Center for Environmentally Sustainable Transportation in Cold Climates

# Use of Cellular Concrete for Air Convection Embankment to Protect Permafrost Foundations in Cold Regions: Feasibility Study

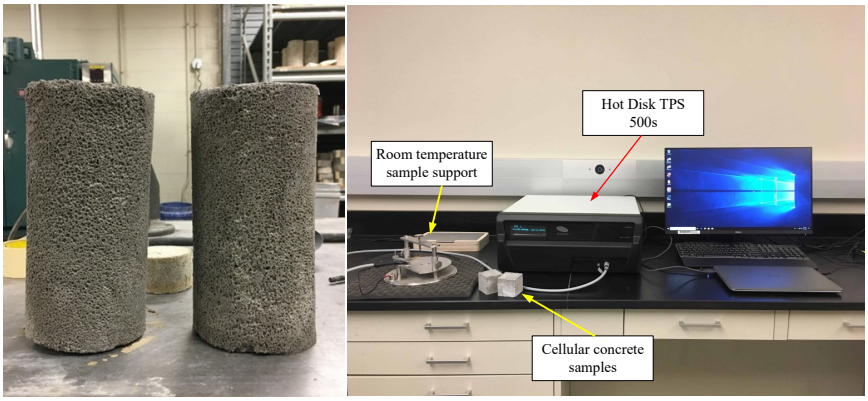


**Prepared by:**

Jenny Liu, Ph.D., P.E. and Hanli Wu
Missouri University of Science and Technology

**August 2019**

**Prepared for:**

Center for Environmentally Sustainable Transportation in Cold Climates
University of Alaska Fairbanks
P.O. Box 755900
Fairbanks, AK 99775

U.S. Department of Transportation
1200 New Jersey Avenue, SE
Washington, DC 20590

**INE/CESTiCC 19.22**

# REPORT DOCUMENTATION PAGE

Form approved OMB No.



| 1. AGENCY USE ONLY (LEAVE BLANK) | 2. REPORT DATE | 3. REPORT TYPE AND DATES COVERED |
|---|---|---|
| | 08/2019 | Final Report: 04/2017 – 08/2019 |

4. TITLE AND SUBTITLE
Use of Cellular Concrete for Air Convection Embankment to Protect Permafrost Foundations in Cold Regions: Feasibility Study

5. FUNDING NUMBERS
CESTiCC 1618

6. AUTHOR(S)
Jenny Liu and Hanli Wu

7. PERFORMING ORGANIZATION NAME(S) AND ADDRESS(ES)
Department of Civil, Architectural, and Environmental Engineering
Missouri University of Science and Technology
Rolla, MO 65409-0030

8. PERFORMING ORGANIZATION REPORT NUMBER
INE/CESTiCC 19.22

9. SPONSORING/MONITORING AGENCY NAME(S) AND ADDRESS(ES)
Center for Environmentally Sustainable Transportation in Cold Climates
University of Alaska Fairbanks
P.O. Box 755900
Fairbanks, AK 99775-5900

10. SPONSORING/MONITORING AGENCY REPORT NUMBER
INE/CESTiCC 19.22

11. SUPPLEMENTARY NOTES

12a. DISTRIBUTION / AVAILABILITY STATEMENT
No restrictions

12b. DISTRIBUTION CODE

13. ABSTRACT (Maximum 200 words)

The air convection embankment (ACE) is a technique used to protect permafrost from thawing in road construction in cold regions. However, the desired materials needed for ACE are not readily available, which prevents its extensive use in Alaska. To overcome the limitation of traditional ACE, and further improve the cooling effect of ACE, this study investigated the feasibility of using cellular concrete as an alternative material for ACE in cold regions. The heat transfer patterns of the cellular concrete ACE, the crushed-rock ACE, and the sand/gravel embankment were studied using the numerical simulation. The results of the present study show that the cooling performance of both cellular concrete ACE and crushed-rock ACE are superior to the traditional sand/gravel embankment. The cellular concrete ACE has better heat insulation property in the summer, and the crushed-rock ACE has stronger natural convection in winter. For the annual cooling efficiency of the two different ACE techniques, the proposed cellular concrete ACE has a better cooling effect on the foundation soil than the crushed-rock ACE. These results indicate that the thermal conductivity and specific heat capacity of construction materials have significant impacts on the performance of the ACE.

14- KEYWORDS: Permafrost, Air Convection Embankment, Cellular Concrete, Crushed Rock, Cooling Effect, Thermal Conductivity, Specific Heat Capacity

15. NUMBER OF PAGES
152

16. PRICE CODE
N/A

| 17. SECURITY CLASSIFICATION OF REPORT | 18. SECURITY CLASSIFICATION OF THIS PAGE | 19. SECURITY CLASSIFICATION OF ABSTRACT | 20. LIMITATION OF ABSTRACT |
|---|---|---|---|
| Unclassified | Unclassified | Unclassified | N/A |

# USE OF CELLULAR CONCRETE FOR AIR CONVECTION EMBANKMENT TO PROTECT PERMAFROST FOUNDATIONS IN COLD REGIONS: FEASIBILITY STUDY

## FINAL REPORT

**Prepared for**

**Center for Environmentally Sustainable Transportation in Cold Climates**

**Authors:**

**Jenny Liu, Ph.D., P.E.**

**Hanli Wu**

**Missouri University of Science and Technology**

**INE/CESTiCC 19.22**

**August 2019**

## DISCLAIMER

This document is disseminated under the sponsorship of the U. S. Department of Transportation in the interest of information exchange. The U.S. Government assumes no liability for the use of the information contained in this document. The U.S. Government does not endorse products or manufacturers. Trademarks or manufacturers' names appear in this report only because they are considered essential to the objective of the document.

# METRIC (SI*) CONVERSION FACTORS

## APPROXIMATE CONVERSIONS TO SI UNITS

| Symbol | When You Know | Multiply By | To Find | Symbol |
|---|---|---|---|---|
| | | LENGTH | | |
| in | inches | 25.4 | | mm |
| ft | feet | 0.3048 | | m |
| yd | yards | 0.914 | | m |
| mi | Miles (statute) | 1.61 | | km |
| | | AREA | | |
| $in^2$ | square inches | 645.2 | millimeters squared | $cm^2$ |
| $ft^2$ | square feet | 0.0929 | meters squared | $m^2$ |
| $yd^2$ | square yards | 0.836 | meters squared | $m^2$ |
| $mi^2$ | square miles | 2.59 | kilometers squared | $km^2$ |
| ac | acres | 0.4046 | hectares | ha |
| | | MASS (weight) | | |
| oz | Ounces (avdp) | 28.35 | grams | g |
| lb | Pounds (avdp) | 0.454 | kilograms | kg |
| T | Short tons (2000 lb) | 0.907 | megagrams | mg |
| | | VOLUME | | |
| fl oz | fluid ounces (US) | 29.57 | milliliters | mL |
| gal | Gallons (liq) | 3.785 | liters | liters |
| $ft^3$ | cubic feet | 0.0283 | meters cubed | $m^3$ |
| $yd^3$ | cubic yards | 0.765 | meters cubed | $m^3$ |

Note: Volumes greater than 1000 L shall be shown in $m^3$

| | | | | |
|---|---|---|---|---|
| | | TEMPERATURE (exact) | | |
| ºF | Fahrenheit temperature | 5/9 (ºF-32) | Celsius temperature | ºC |
| | | ILLUMINATION | | |
| fc | Foot-candles | 10.76 | lux | lx |
| fl | foot-lamberts | 3.426 | candela/$m^2$ | $cd/cm^2$ |
| | | FORCE and PRESSURE or STRESS | | |
| lbf | pound-force | 4.45 | newtons | N |
| psi | pound-force per square inch | 6.89 | kilopascals | kPa |

These factors conform to the requirement of FHWA Order 5190.1A *SI is the symbol for the International System of Measurements

## APPROXIMATE CONVERSIONS FROM SI UNITS

| Symbol | When You Know | Multiply By | To Find | Symbol |
|---|---|---|---|---|
| | | LENGTH | | |
| mm | millimeters | 0.039 | inches | in |
| m | meters | 3.28 | feet | ft |
| m | meters | 1.09 | yards | yd |
| km | kilometers | 0.621 | Miles (statute) | mi |
| | | AREA | | |
| $mm^2$ | millimeters squared | 0.0016 | square inches | $in^2$ |
| $m^2$ | meters squared | 10.764 | square feet | $ft^2$ |
| $km^2$ | kilometers squared | 0.39 | square miles | $mi^2$ |
| ha | hectares (10,000 $m^2$) | 2.471 | acres | ac |
| | | MASS (weight) | | |
| g | grams | 0.0353 | Ounces (avdp) | oz |
| kg | kilograms | 2.205 | Pounds (avdp) | lb |
| mg | megagrams (1000 kg) | 1.103 | short tons | T |
| | | VOLUME | | |
| mL | milliliters | 0.034 | fluid ounces (US) | fl oz |
| liters | liters | 0.264 | Gallons (liq) | gal |
| $m^3$ | meters cubed | 35.315 | cubic feet | $ft^3$ |
| $m^3$ | meters cubed | 1.308 | cubic yards | $yd^3$ |
| | | TEMPERATURE (exact) | | |
| ºC | Celsius temperature | 9/5 ºC+32 | Fahrenheit temperature | ºF |
| | | ILLUMINATION | | |
| lx | lux | 0.0929 | foot-candles | fc |
| $cd/cm^2$ | candela/$m^2$ | 0.2919 | foot-lamberts | fl |
| | | FORCE and PRESSURE or STRESS | | |
| N | newtons | 0.225 | pound-force | lbf |
| kPa | kilopascals | 0.145 | pound-force per square inch | psi |

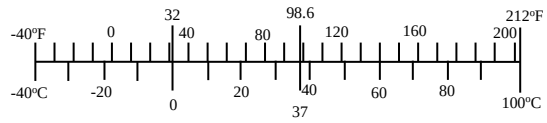

## ACKNOWLEDGMENTS

The authors wish to express their appreciation to the ADOT&PF personnel for their support throughout this study, as well as the Center for Environmentally Sustainable Transportation in Cold Climates (CESTiCC). The authors would also like to thank Aerix Industries' assistance and support during the laboratory tests for providing foaming agent and loaning the laboratory foaming generator to use.

## TABLE OF CONTENTS

## LIST OF FIGURES

## LIST OF TABLES

## EXECUTIVE SUMMARY

For engineering practice in permafrost regions, keeping the temperature of the native surface below the freezing point is the critical factor that determines the stability of the structures. The crushed-rock air convection embankment (ACE) is an excellent way to protect the active permafrost layer from thawing in the road construction of the interior of Alaska due to its excellent cooling effect in winter and good thermal resistance performance in summer. However, the desired materials needed for ACE are not readily available, which prevents its extensive use in Alaska. To overcome the limitation (shortage of crushed rocks) of traditional ACE, and further improve the cooling effect of ACE, a new strategy of using cellular concrete as an alternative material for ACE is proposed in this study.

Density, porosity, thermal conductivity of cellular concrete can be designed that makes it a promising alternative material to replace crushed rocks as a building material in embankment construction. In addition, cellular concrete is flexible in casting; it can be created to any shapes and any gradations needed to improve the cooling effect of the embankment. Moreover, the utilization of more industrial byproduct and less Portland cement in cellular concrete makes it a great economical and sustainable construction material.

This study investigated the properties of cellular concrete to evaluate the potential of cellular concrete as an alternative material for ACE construction. The influence of foam content and the proportion of sand on the compressive behavior of cellular concrete were investigated in

a preliminary lab test. Based on the initial results and conclusion of the test, five sets of cellular concrete specimens with 10%, 20%, 30%, 40%, and 50% foam content were prepared in the lab to further investigate the influence of foam content on the properties of cellular concrete. The flow table test was done using the consistency definitions described in ASTM C1107. Based on the flowability measurement by ASTM C1437, the flow table test was conducted in the lab to evaluate the ease of placing, consolidating, and finishing freshly placed concrete without segregation. Both fresh density and oven-dry density of cellular concrete specimens were measured and analyzed. The permeability test was conducted in the lab using Isco pump and core holder, and a high water pressure environment was created in the core holder. For the evaluation of compressive strength, 2in×2in cube specimens, as described in ASTM C109, were prepared according to ASTM C1107. The 200 Kip Tinius-Olsen Universal Testing Machine was used to test the compressive strength of the cubic specimens at several ages: 7, 14, 28, 60, and 120 days. The test results provide useful information for the application of this cellular concrete material in embankment construction. Thermal properties, especially thermal conductivity and specific capacity are the key factors in the ACE performance. The Hot Disk TPS 500S was selected to investigate the thermal properties of cellular concrete specimens. A fractional factorial design (Taguchi Methods) based on an “orthogonal array” was used to evaluate the effects of various key factors, such as fly ash, slag, and water-cementitious ratio, on the thermal properties and compressive strength of cellular concrete. The statistic software MINITAB was used to evaluate the impact of multiple variables (foam, water, cement, fly ash, and slag) on a set of responses

such as thermal conductivity and compressive strength. Moreover, an optimal mix design was obtained considering compressive strength and relatively low thermal conductivity.

The lab test results indicated that the compressive strength of cellular concrete is a function of its porosity (or density) and compressive strength decreases significantly at high porosities. The cellular concrete with foam content of 30% to 40% was recommended as an alternative material for ACE construction. Cellular concrete in this range can guarantee sufficient strength and superior thermal insulation properties. The influence of four different independent variables (foam volume, water-cementitious ratio, fly ash, and slag) on the properties of cellular concrete was investigated, and nine sets of specimens with different mix designs were used for testing the properties of cellular concrete. The results showed that for 3, 7, 14, 21, and 28 days the compressive strength could be obtained in the range of 1.8-11.8, 2.4-15.0, 3.3-17.0, 4.2-18.7, and 5.4-21.2 MPa, respectively. Also, the thermal conductivity of nine sets of cellular concrete specimens ranged from 0.3460 W/m·℃ to 0.5455 W/m·℃. The MINITAB predicted that the thermal conductivity of cellular concrete could reach 0.25 W/m·℃ under the premise of ensuring sufficient compressive strength.

In this study, the heat transfer pattern of the cellular concrete ACE, the crushed-rock ACE, and the sand/gravel embankment were studied by using the numerical method. The results of the present study show that the cooling performance of both cellular concrete ACE and crushed-rock ACE is superior to the traditional sand/gravel embankment. The cellular concrete ACE has better heat insulation property in the summer, and the crushed-rock ACE has stronger

natural convection in winter. For the annual cooling efficiency of the two different ACE strategies, the proposed cellular concrete ACE has a better cooling effect on the foundation soil than the crushed-rock one. The study indicated that the thermal conductivity and specific heat capacity of the construction materials have a significant impact on the performance of the ACE.

# CHAPTER 1.0 INTRODUCTION

## 1.1 Problem Statement

The air convection embankment (ACE) concept has been studied for many years. Previous numerical and field studies have confirmed that ACE can be successfully used to provide passive cooling for roadway embankments in permafrost zones around the world, including China, Russia, Canada, and interior Alaska. However, in many areas of interior Alaska, the coarse gravel or crushed rocks needed for ACE construction are not readily available. Burdened by the need to ship suitable rock to remote locations, costs for constructing an ACE are often prohibitively high, which prevents its widespread use in Alaska. An existing cementitious material may provide the solution.

The use of cellular concrete has expanded considerably in the last 10 to 15 years, use as precast panels, floor slabs, roof sections, backfills, and other non-structural functions. Cellular concrete uses a special foaming agent that entrains large amounts of finely divided air bubbles into the mixture. It has excellent insulating characteristics, high strength, and is easy to use. It is a promising cost-effective alternative to crushed rocks for broader implementation of the ACE design in Alaska. No previous research has been done on using cellular concrete to construct an ACE. Therefore, this research will investigate the feasibility of using cellular concrete as an alternative to crushed rocks to take full advantage of the ACE design. Cellular concrete is also a

lightweight fill material, which is an extremely desirable characteristic for many foundation locations that would benefit from the ACE design.

### 1.2 Background

Much of the interior of Alaska is underlain by thaw-unstable permafrost or frozen ground in which temperatures hover near thawing and thus are more susceptible to thermal degradation (Ferrians, 1994; Goering and Kumar, 1996; Regehr et al., 2013; Ma et al., 2017). Construction of transportation infrastructure in these regions often results in a disturbance of the pre-existing thermal balance and subsequent permafrost thawing, this is particularly true in the side-slope regions of road embankments where winter snow-removal provides effective insulation while dry, sparsely vegetated conditions lead to a high surface temperature during the summer (Goering and Kumar, 1996; Saboundjian and Goering, 2003; Zhang et al., 2006; Regehr et al., 2013). The increased temperatures and thawing permafrost often result in shoulder rotations and longitudinal cracks in pavements.

Previous studies have shown that the air convection embankment (ACE) is an excellent technique to cool the roadbed and stabilize the roadway embankment (Goering and Kumar, 1996; Lai et al., 2006; Ma et al., 2006; Zhang et al., 2006; Mu et al., 2012; Regehr et al., 2013; Dong et al., 2014). The ACE technique has been studied since the 1990s (Goering and Kumar, 1996). It involves building road embankments using a highly porous material, such as poorly graded gravel or crushed rock without fines. This high permeability allows for the natural convection of the air to occur within the embankment during the winter months, the natural

convection results in unstable air density gradients, which subsequently cool the embankment. During summer months, the embankment density gradients are stable, and circulation does not occur (Goering and Kumar, 1996; Zhang et al., 2006; Regehr et al., 2013). Thus, the embankment acts as a one-way heat transfer structure, effectively removing heat from the underlying foundation and eliminating thaw settlement. Goering and Kumar (1996) reported numerical simulation results that demonstrated the passive cooling capability of air convection within roadway embankments.

In 1995, the Alaska Department of Transportation and Public Facilities (AKDOT&PF) started a project (Goering, 1997) entitled "Air Convection Embankment Experimental Feature Design," which was intended to design and install an ACE roadway embankment in a road project via the Experimental Features in Construction Program. The design and construction of the experimental feature took place during 1995-97, with completion of the ACE test section in July 1997. In 1996, the original project was extended into a second phase to allow for three years of monitoring. This monitoring period began in November of 1996 and was originally scheduled for completion at the end of September 1999. A no-cost extension approved in 1999 extended the monitoring period through December 2000. Goering (1997) detailed the design and construction process. The first five years of monitoring (November 1996 – December 2000) were discussed in three publications (Goering, 1998; Goering, 2001, 2003). Data collected from the Parks/Chena Ridge ACE test embankment indicated that convective cooling was taking place within the test embankment during winter months, and temperatures beneath the ACE test section were

generally cooler than those recorded beneath the control section. Goering (2003) performed a numerical study with a particular focus on the effect of convective cooling in railway embankments and application to permafrost areas. A two-dimensional unsteady finite-element model was used to examine the heat transfer characteristics of these embankments. The results showed significant differences in circulation patterns and a cooling effect throughout the yearly cycle. Xu and Goering (2008) presented thermal performance data for ventilated shoulders during the first year of operation in the same project. The data presented for the ventilated shoulders demonstrates that they produce a maximum cooling effect at the base and over the lower portion of the side slope boundary. Mean annual temperatures within the lower portion of the rock layer were approximately 4.5 °C cooler than the mean ambient air temperature during the test period. Temperature data indicated a significant cooling trend in the subgrade foundation soil beneath the ventilated shoulder during the test period.

Similar success was reported by researchers in other parts of the world (Mu et al., 2011; Zhang et al., 2006; Lai et al., 2006; Regehr et al., 2013; Pei et al., 2014; Dong et al., 2014; Qian et al., 2012; Mu et al., 2012). Rooney (1997) describes the use of this technique in Russia. In the last decades, this technique has been used extensively in the recently completed Qinghai–Tibet Railway project (Sun et al., 2005; Ma et al., 2006). Based on the success in both numerical simulations and field observations in Alaska, McHattie and Goering (2009) summarized a simplified one-dimensional "Air Convection Embankment (ACE) Design Guide." Other numerical and field studies have confirmed that an ACE can be successfully used to provide

passive cooling for roadway embankments in permafrost zones in places such as China, Russia, and Canada. However, easy access to coarse gravel or crushed rocks, needed for ACE construction, has limited the use of ACEs in other areas (Saboundjian, 2008; Ferrell, 2009). A potentially cost-effective alternative material with high performance is needed to replace crushed rocks in ACE construction.

Cellular concrete could address this problem in two ways. Cellular concrete uses a special foaming agent that entrains large amounts of finely divided air bubbles in the mixture. Due to these unit weights and air content, cellular concrete can potentially be an insulating material. Besides, sufficient material strength of the cellular concrete to meet the needs of a pavement structure is usually achievable. Cellular concrete has a relatively high compressive strength (0.5-17 MPa) in comparison to its relatively low density (400-1920 kg/m$^3$), which is associated with good thermal conductivity (0.1-0.7 W/(m·K)). As the foam content increases, the unit weight decreases, as does the strength of the concrete. On the other hand, the thermal properties improve (i.e., thermal conductivity decreases) as the foam content increases (Lamond and Pielert, 2006; Amran et al., 2015; Samson et al., 2016).

Another benefit of using cellular concrete is that it is both easy to use and cost-effective. Manufacturing cellular concrete uses primarily conventional methods, except that it requires the use of a foam generator and creates foam by combining water and a foaming agent (Ramamurthy et al., 2009; Samson et al., 2016). The placement method is often by direct shoot or by a pumping and distribution hose. The workability of cellular concrete can vary widely depending

upon the application. Setting characteristics may also provide another means to change the placement method, particularly for pavement applications (Rasheed and Prakash, 2015; Amran et al., 2015). With these types of material characteristics, the use of cellular concrete as an alternative material for the ACE construction appears entirely plausible. However, no previous research has been done regarding using cellular concrete to construct an ACE. Research in this area could transform infrastructure construction in the Circumpolar North.

### 1.3 Objectives

The objective of the proposed research is to investigate the possibility of using cellular concrete as an alternative to crushed rocks to extend the use of the ACE design in interior Alaska. The research focused on the following four aspects: (1) mixture proportions to yield adequate combinations of density, strength, and thermal conductivity, (2) material combinations to provide the lowest cost at the longest performance, (3) numerically investigate the feasibility of using cellular concrete as an alternative to crushed rocks to extend the use of the ACE design in interior Alaska, (4) provide a rough cost estimation of cellular concrete ACE, crushed-rock ACE, and conventional sand/gravel embankment.

### 1.4 Research Methodology

The following major tasks were completed to achieve the objectives of this study:

- Task 1: Literature Survey
- Task 2: Material Ingredients Selection and Optimization of Mix Design
- Task 3: Numerical Simulation

- Task 4: Economic Analysis
- Task 5: Final Report and Recommendations

***Task 1: Literature Survey***

This task involved a comprehensive literature search of published materials and on-going research projects regarding ACE technology and the use of cellular concrete in different applications. This survey investigated the feasibility of using cellular concrete as an alternative material for ACE construction.

***Task 2: Material Ingredients Selection and Optimization of Mix Design***

This task involved trial tests of material combinations of cement, fly ash, silt, and a foaming agent with different amounts of foam. The effects of those design factors on the setting time (ASTM C191), flowability, and compressive strength (ASTM 39) of pastes were investigated to determine the optimum paste design. Then the workability (ASTM C1437), thermal conductivity, and concrete density and compressive strength (ASTM 39) were evaluated to finalize the optimum mix design of cellular concrete.

***Task 3: Numerical Simulation***

A series of numerical simulations were used to quickly investigate the effects of cellular concrete on ACE performance in interior Alaska. The virtual highway and railway embankments were built using designs similar to those in Goering and Kumar (1996) and Goering (2003). The material properties for the foundation soils and the climatic conditions were the same as those used in the Goering and Kumar (1996) for highway embankment and Goering (2003) for railway

embankment. First, the physical models and governing equations of air convection in a porous medium were discussed. Then a series of numerical simulations were used to investigate the performance of cellular concrete, crushed-rock ACE, and a commonly used sand/gravel embankment. Case 1 corresponds to a cellular concrete ACE, and Case 2 corresponds to a crushed-rock ACE, whereas Case 3 corresponds to a compacted sand/gravel embankment. The results for the three cases are compared and discussed. The simulation results were compared with those in previous analyses for conventional granular road embankment and ACE with a well-drained crushed open rock to evaluate the performance of the cellular concrete.

***Task 4: Economic Analysis***

An economic analysis was performed to compare the costs of constructing an ACE embankment using the crushed rocks and cellular concrete, and the traditional silty sand/gravel embankment in interior Alaska.

***Task 5: Draft of Final Report and Recommendations***

A final report was drafted upon the completion of previous tasks, and recommendations for using the cellular concrete to construct an ACE were provided.

## 1.5 Outline of the Report

The report includes six chapters. Chapters 1 and 2 provide an introduction and a literature review. Chapter 3 presents a detailed description of the laboratory test of cellular concrete. In the initial screening test, five sets of mixtures were designed to investigate the influence of foam content on the physical properties of cellular concrete. In the optimization test, nine sets of

mixtures were designed using the Taguchi method. Chapter 4 presents the details of three numerical simulations of embankments, and the cooling effects of three models were compared and discussed. Chapter 5 presents a brief economic analysis to compare the costs of constructing an ACE embankment using the crushed rocks and cellular concrete in interior Alaska. Finally, Chapter 6 provides the main conclusions and recommendations taken from the study.

# CHAPTER 2.0 LITERATURE REVIEW

A literature review was performed, to collect information on critical subjects that pertain to this study such as roadway embankment construction techniques in permafrost regions, roadway embankment cooling systems and cooling effects, and, the development, and applications of cellular concrete. Special attention was put on the air convection embankment (ACE) and cellular concrete. The cooling effect of ACE was discussed in detail, supported by a lot of numerical simulation and engineering practices in North America, China, and Russian. The physical, mechanical, and functional properties of cellular concrete were also introduced. The performance and application of cellular concrete were illustrated and discussed in detail. Due to cellular concrete's excellent insulation characteristics and relatively good structural performance, cellular concrete shows good potential as a cost-effective alternative to crush rocks for broader implementation of ACEs.

## 2.1 Background

### *2.1.1 Challenges of Permafrost Foundation in Cold Regions*

There are about 35,760,000 $km^2$ of permafrost worldwide, approximately 24% of the land area in the world (Lai et al., 2006). Permafrost can cause many engineering and geotechnical problems such as thaw settlement, slope instability, drainage issues, which are significant challenges for engineering projects.

Despite many engineering techniques developed in recent years, it is still challenging to construct and maintain infrastructure in permafrost regions. These geotechnical and engineering problems not only impact the construction and design but also can cause problems in the long run as well, due to changing environments and seasonal fluctuations (Regehr et al., 2013; Mu et al., 2012). The temperature of the buildings is relatively high, and the heat could potentially thaw the frozen ground below it, causing permafrost degradation, this could then destabilize the foundation of a road structure (Ma et al., 2006). The majority of permafrost in the world is distributed in the interior of Alaska, Siberia, Northern Canada, Greenland, and the Qinghai-Tibetan Plateau.

In recent years, many techniques have been developed to solve the problems of engineering in permafrost regions such as cooling the roadbed, controlling roadbed thawing and raising embankment alignment. Regehr et al. (2013) summarized the techniques to control roadbed thawing, insulate the roadbed, and reduce roadbed fill weights. Compared with roadbed applications in permafrost regions, the cooling roadbed techniques, especially ACEs, are most likely to reduce the temperature of the embankment effectively, prevent thawing of ice in permafrost layers, and promote long-term roadbed stability (Goering and Kumar, 1996; Goering, 2003). However, in many areas, the coarse gravel or crushed rocks needed for ACE construction are not readily available. Burdened by the need to ship suitable rocks to permafrost regions, costs for ACE construction are usually prohibitively high; a potentially cost-effective alternative material with high performance is needed to replace crushed rocks in ACE construction.

### *2.1.2 Engineering Practices in Russia, North America, and China*

With the development of economic and transportation systems in recent years, the need for highway, railway and other infrastructure in the permafrost region keeps rising. Reliable transportation infrastructures play a vital role in improving the quality of life for residents in cold regions, transporting natural resources, industrial products, and daily goods (Regehr et al., 2013).

The development of railroads and transportation systems in permafrost regions has a history of more than 100 years. A vast amount of practices on embankment construction in permafrost regions were studied by many engineers and researchers around the world. Russian engineers pioneered permafrost construction with the practices of the Trans-Siberian Railway in 1895. After a few years, North America obtained many experiences in the construction of the Alaska Railway in 1904 and the following construction of the Hudson Bay Railway in 1910. In recent decades, Chinese engineers have improved and advanced the techniques by researching and applying new techniques in the construction of the Qinghai-Tibet Railway in permafrost regions (Regehr et al. 2013).

## 2.2 Techniques for Roadbed Practices in Permafrost Regions

A review of techniques for improving roadbed stability in permafrost regions was provided based on a comprehensive investigation. These techniques are mainly divided into three categories: 1) Improving Quality/uniformity of Pavement Subsurface Material; 2) Raising Embankment Alignment; and 3) Cooling the Roadbed and Reduce Temperature Variations. Other techniques for roadbed practices in permafrost regions include insulating the roadbed,

reducing roadbed fill weight, and improving pavement subsurface drainage. One of the most effective techniques is cooling the foundation and reducing temperature variations with the ACE concept, which will be illustrated and discussed in detail in section 2.3.

### *2.2.1 Improve Quality/uniformity of Pavement Subsurface Material*

One of the geotechnical techniques to prevent frost damage is to stabilize the soil, which is usually to remove the frost susceptible soils or vegetative layers down to frost depth and replace the soil with non-frost susceptible material. Because of the expense of excavation and the availability of the non-frost susceptible material, this solution is not widely used in construction (Ye et al., 2007; Regehr et al., 2013). Another method is to control the permafrost thaw rate after embankment construction. Regehr et al. (2013) pointed out that wide embankments have a significant influence on soil disturbance and thus enlarge the thawed zone. The insulation effect of snow cover can be minimized by removing snow frequently. However, this is not practical in a remote area.

### *2.2.2 Raise Embankment Alignment*

Besides replacing with non-frost susceptible soils, the thaw settlement can also be controlled through raising the embankment alignment. In shallow groundwater situations, raising the existing alignment can provide sufficient clearance above groundwater, and the water accessibility can be reduced. In other words, water cannot be transported to the freeze front through a capillary rise if the pavement structure is isolated from the influence of groundwater.

This treatment method can be expensive, depending on the availability and quantity of material required.

### *2.2.3 Cool the Roadbed and Reduce Temperature Variations*

The thaw settlement problem can be mitigated through reducing the temperature in the embankment, which helps prevent the ice lens from forming and avoiding the thaw-weakening of the permafrost layers (Goering and Kumar, 1996; Goering, 1998; Goering, 2003). There are many different types of roadbed cooling systems in the application of stabilizing the permafrost layers such as shading boards, insulation methods, ACEs, ventilation ducts, and thermosyphons.

#### *Shading Board*

Shading boards have an excellent cooling effect by reducing solar radiation. Field tests, along the Qinghai-Tibet Highway, of shading boards indicated that the shading board techniques could reduce the annual average surface temperature of the side slope of the embankment by about 3.2℃, compared with the embankment slope without shading board (Yu et al., 2008). Field test results showed that the annual average slope surface temperature under the shading board was about 1.5℃ lower than the nearby natural ground surface. However, the shading board could be destroyed easily by strong wind if placed too high. The installation and maintenance costs should be considered for the long term (Yu et al., 2008).

#### *Ventilation Ducts*

Ventilation ducts are hollow tubes installed in the embankment, which allow cold air to pass through and transfer heat from the tubes (Regehr et al., 2013). A field test conducted by Niu

et al. (2006) on the Qinghai-Tibet Plateau explored the cooling effect of the duct-ventilated railway embankment. The results showed that, for roadbed with duct at a low position, the heat absorption only lasts a short period and then releases heat, which indicates that low-positioned ducts offer more effective cooling for the permafrost than high-positioned ducts.

### *Thermosyphons*

Thermosyphons are two-phase convection tubes. Thermosyphons with condensers are buried below the driving surface without using air-cooled heat exchangers. Xu and Goering (2008) investigated the thermal performance of Hairpin thermosyphons and ventilated shoulders. The results showed significant cooling effect in the subgrade foundation soil beneath the ventilated shoulder. Heat flux and temperature data collected from the Hairpin thermosyphons displayed its effectiveness at removing heat from the subgrade soils beneath the center of the embankment. The temperature measurements presented in this study showed that the passive cooling system was operating effectively.

### *Air Convection Embankment (ACE)*

Another technique is to use the ACE, which involves building road embankments using a highly porous material, such as poorly graded gravel or crushed rock without fines to facilitate natural convection of the pore air. The detail of the mechanism, cooling effect, and thermal characteristics of ACE will be illustrated and discussed in the following section.

## 2.3 Air Convection Embankment (ACE)

A series of studies reported that thaw settlement of permafrost could mostly result in instability and failure of the embankment. Therefore, techniques for preventing damage to embankment due to thaw settlement are of prime importance (Zhang et al., 2006). ACE, also known as crushed rock embankment, has widely been used in Qinghai–Tibetan railway roadbed constructions to protect permafrost from thaw settlement in recent decades, due to its excellent cooling effect.

The ACE has been studied since the 1990s (Goering and Kumar, 1996). Several earlier investigations on ACE give a detailed discussion on its mechanism, cooling effects, and applications.

### *2.3.1 Mechanism of Air Convection Embankment*

It has been proven that ACEs constructed with crushed rock layer in permafrost regions have a distinct cooling effect for preventing thaw-settlement and stabilizing the permafrost layers of roadways in areas of warm permafrost (Goering, 1998; Goering, 2003; Sun et al., 2005; Liu et al., 2017).

ACEs are constructed by utilizing crushed rocks or poorly graded open aggregates, resulting in very high air permeability. In winter, the ambient temperature is lower than the underlying permafrost. Air density gradients formed within the embankment during cold winter result in pore air convection. This convection speeds up the heat out of the embankment during cold periods. During the summer, convection does not occur due to the stable air density gradient

(Goering, 1998). It is observed that heat from the bottom of the crushed rock mass can be efficiently removed in winter, but little has been removed during the warm season (Lai et al., 2006). In cold seasons, ACE performs excellent cooling effect, and in warm-season, it turns to provide an excellent thermal insulation resistance to protect the heat transfer from the ambient environment to the permafrost layer (Goering, 1998).

Regehr et al. (2013) summarized several typical ACE techniques such as full ACE, base layer ACE, shoulder ACE, U-shape ACE, and toe berm ACE (Figure 2.1). In addition, the cooling mechanism and effect of ACE were shortly illustrated and discussed in his study.

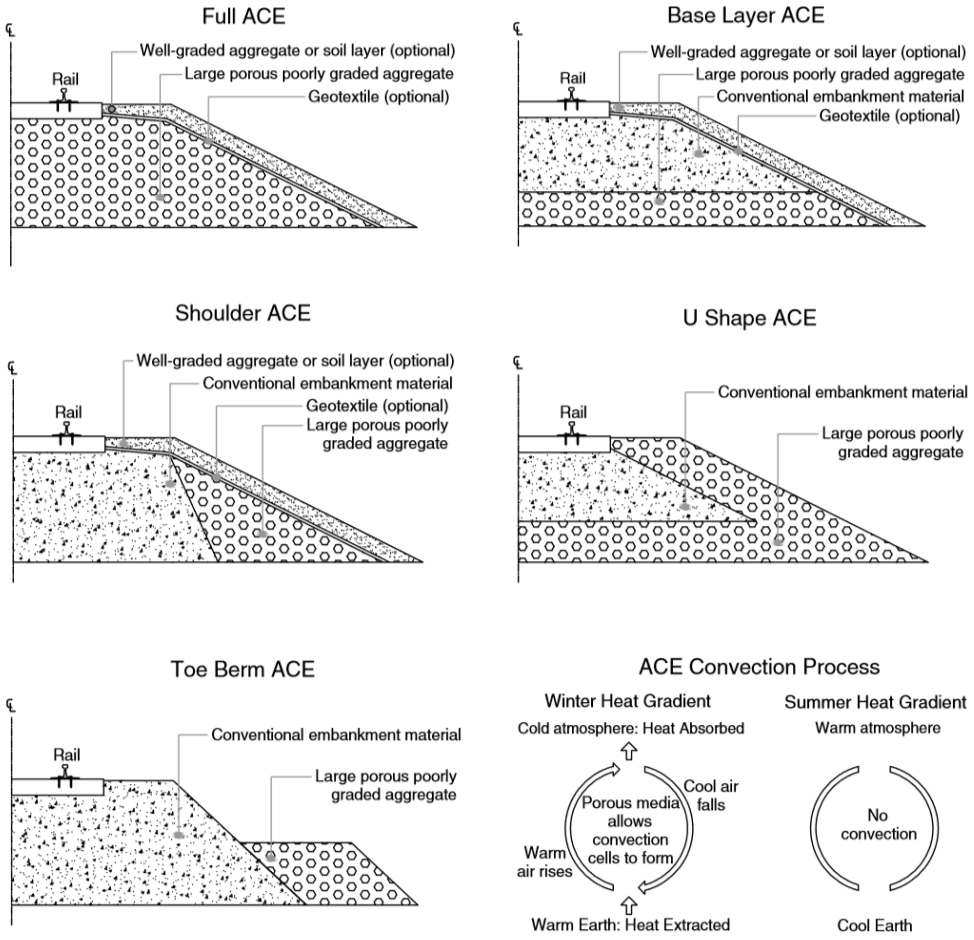


**Figure 2.1** Conceptual diagrams of various ACE configurations (adapted from Regehr et al., 2013).

### *2.3.2 Cooling Effects and Boundary Conditions*

#### *Cooling effects*

Many previous studies have investigated the cooling effect of ACEs. Vast amounts of experiments and numerical analyses have been conducted to explore the mechanism of the cooling effect of ACEs. Goering and Kumar (1996) introduced a numerical method to quickly investigate the effect of wintertime convection in the open-graded embankment, and a field

investigation of the open-graded roadway indicated that the simulation method showed its great potential in quickly investigating the effect of ACE. In addition, a long-term field-based study at Brown's Hill Quarry near Fairbanks, Alaska, showed that ACE has a strong influence on decreasing the roadbed temperature in winter and a strong insulation effect in summer (Goering, 1998).

In recent years, many ACE practices and researches were conducted in the Qinghai-Tibet Railway. Based on eight years of long-term monitoring along the Qinghai-Tibet Railway, Mu et al. (2012) reported that the cooling effect of ACE was distinct. However, the underlying permafrost along the railway experienced the different thermal processes in the relatively warm and cold permafrost region. Lai et al. (2006) conducted a series of experiments for the crushed rock layer with open and closed boundary conditions. It was observed that heat from the bottom of the crushed rock mass was efficiently removed in winter, but little was removed during the warm season. Annual observation showed that the cooling effect of ACE was distinct; it is an active cooling technique for reducing permafrost temperature and preventing permafrost degradation.

***Porosity and gradation***

The existence of large porosity of the crushed rock embankment is the main reason for the cooling effect (Liu et al., 2017). Previous studies reported that the first-rate importance for the cooling effect is the porosity and gradation of ACE. However, due to strong wind, the wind-blown sand and rock debris reduce the porosity of the embankment, which over time results in

weakening the cooling effect of ACE (Liu et al., 2017). Rooney (1997) reported the application of air convention embankment on the BAM railway system in Russia. Based on several field-based tests, Rooney (1997) concluded that large size rock fill is better for decreasing the embankment temperature, but the gravel-size rocks seemed more economical to use. In addition, the author pointed out that specific design techniques and the influence of microclimate must be taken serious consideration. Mu et al. (2012) also emphasized that the natural environment is a significant contributing factor for the cooling effect of ACE that we cannot ignore.

Sun et al. (2005) investigated the cooling effect of ACE on Qinghai-Tibet Plateau. The crushed rocks with a diameter of 5-8cm (small crushed rock SCR) and 40-50cm (big crushed rock BCR) was selected for experimental test separately (Figure 2.2).

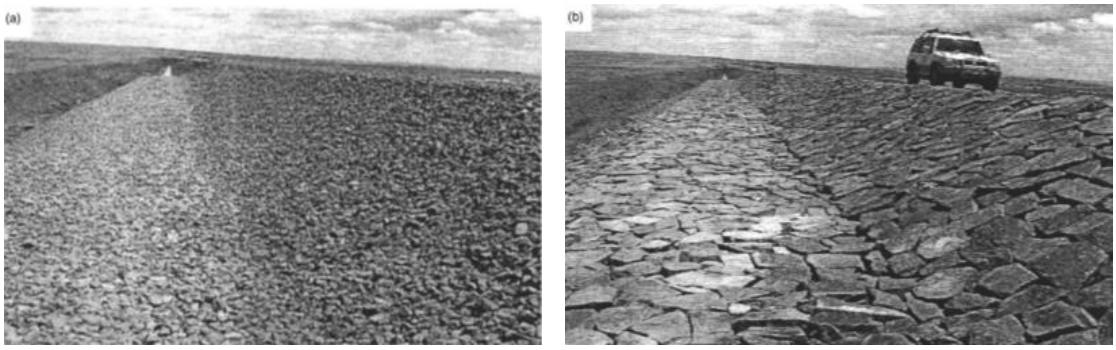


**Figure 2.2** Small crushed-rock ACE and big crushed-rock ACE (adapted from Sun et al., 2005).

The results showed that the SCR layer had better heat insulation in the summer and the BCR had stronger convection effectiveness in winter. Consider the annual cooling efficiency of the two crushed rock layers; the BCR layer had a better cooling effect on the foundation soil than the SCR layer (Sun et al., 2005).

***Boundary conditions***

The crushed-rock embankment can be mainly divided into two categories, based on the boundary conditions (impermeable and permeable) of the crush-rock layer. One is closed-boundary ACEs; the other is open-boundary ACEs (Zhang et al., 2006).

The boundary condition of ACE can largely influence the heat transfer pattern of the embankment in permafrost regions (Zhang et al., 2006). A series of experiments were carried out by Lai et al. (2006) to explore the heat-transfer mechanism and cooling effect of the crushed-rock layers with closed or open boundaries and periodically changed boundary temperatures. Further studies conducted by Zhang et al. (2006) reported that when the height of the embankment is low, the boundary conditions cause no distinct difference to the cooling effect, however, when the height of the embankment is high, and the boundary conditions largely influence the temperature distribution of crushed-rock embankment. Moreover, the cooling effect under the open boundary condition is far better than the closed boundary condition. However, the asymmetric temperature distribution problem of the high embankment, caused by external wind and open boundary conditions, should be taken into serious consideration during road design period (Zhang et al., 2006).

### *2.3.3 Thermal Characteristics*

ACE has recently been used for roadbed construction in permafrost regions due to its semiconductor characteristics, the ACEs have a cooling effect on the permafrost that can eliminate the degradation of permafrost layers and make it much more stable. Thermal

conductivity is of vital importance for ACE thus it has recently been investigated by many researchers (Goering, 2003; Li et al., 2009; Zhi et al., 2008; Wu et al., 2010; Mu et al., 2010; Pei et al., 2014; Liu et al., 2017).

Li et al. (2009) investigated the thermal characteristics of ACE, daily and annually, with crushed rock side slope by using a numerical method. Liu et al. (2017) focused on the change of porosity and its impact on the thermal regime of ACE in the Qinghai-Tibet Railway. Moreover, it was pointed out that optimized porosities of the crushed rock layer could make the underlying permafrost of Qinghai-Tibet Railway keep stable in the coming 50 years. Pei et al. (2014) conducted thermal stability analysis by considering three types of embankment: the crushed-rock interlayer embankment, the crushed-rock base embankment, and the crushed-rock interlayer-revetment embankment. Sun et al. (2005) investigated the heat transfer characteristics of ACE considering the crushed rock layer with two gradations and the results indicated that crushed-rock layers using big rocks had a better cooling effect than small crushed rock layers.

**2.4 Cellular Concrete**

Cellular concrete also known as foam concrete, is a lightweight concrete consisting of a system of homogeneous cell structures made by the injection (or blending) of prepared foam or by the generation of gas into a cement-based slurry (Lamond and Pielert, 2006; Ramamurthy et al., 2009; Amran et al., 2015). Cellular concrete is recognized for its excellent thermal and acoustic insulation, high strength-density ratio, lightweight and low cement content (Amran et al., 2015; Rasheed and Prakash, 2015). In practice, cellular concrete has been widely used as no-

and semi-structural materials in recent years. A variety of excellent functional properties makes it suitable for a considerable number of functional applications (Ramamurthy et al., 2009; Amran et al., 2015).

### *2.4.1 Proportioning and Preparation of Cellular Concrete*

#### *Supplementary Cementitious Materials*

Fly ash or natural pozzolans are most common for use as supplementary cementitious materials (SCM) in Portland cement. There are many benefits to utilizing the SCM in the mix design. For instance, it usually has a reasonable cost saving by using mineral admixtures or industry byproducts in mix design (Kashani et al., 2017). Moreover, the pozzolanic properties of SCM would have a positive impact on flowability, compressive strength, permeability, and reducing the heat of hydration (Lamond and Pielert, 2006).

In recent years, many researchers and engineers conducted a series of experiments to investigate the influence of SCM on the properties of cellular concrete. Krivenko and Kovalchuk (2014) studied the impact of alkali-activated fly ash on the heat resistance ability of cellular concrete. Liu et al. (2016) utilized oil palm shell, a kind of industrial waste, as lightweight coarse aggregate, to develop an environmentally friendly foamed geopolymer concrete. Jones et al. (2017) developed a kind of backfill material based on an ultra-low-density cellular concrete by utilizing a considerable proportion of fly ash to replace Portland cement, which significantly reduced the embodied carbon dioxide of these mixes.

### *Foam Agents*

Foam agents can significantly influence the concrete density through a rate of air bubbles created in the paste mixtures (Amran et al., 2015). In general, there are two typical types of foam agents used for preparing cellular concrete, synthetic foaming agents and protein foaming agents, but the mechanism of foaming generation differs from each other (Kuzielová et al., 2016).

The dosage of the foaming agent is a significant factor for the properties of cellular concrete. Risdanareni et al. (2017) investigated the influence of a dose of a foaming agent on the properties of geopolymer foam concrete. The foamed concrete utilized fly ash and metakaolin as a raw mineral source, with the dosage of the foaming agent of 0%, 0.3%, 0.6% and 0.9% by weight separately. In addition, Amran et al. (2015) pointed out that the volume of foam agent has a significant effect on the properties of cellular concrete. Moreover, excessive foam volume results in a drop in the flow of fresh concrete.

Kuzielová et al. (2016) reported that microwave and ultrasonic treatment could significantly improve the performance of a foaming agent on some critical properties of cellular concrete. With the treatment applying to the foaming procedure, smaller pore size and correspondingly higher compressive strength values can be obtained. In addition, the stability of the foam was enhanced, and the less foaming agent needed in the newly developed foaming method. Liu et al. (2011) investigated the effectiveness of dodecanamide foaming agent as an alternative foaming agent in preparing foam concrete, which showed high potentials in low-density foam concrete application. Lin et al. (2013) utilized a novel foaming agent to improve

the stability and uniformity of foam resulted in the higher performance of the newly developed foam concrete.

### *2.4.2 Properties of Cellular Concrete*

#### *Physical Properties*

Physical properties such as porosity, permeability, density, and drying shrinkage are considered as important factors to evaluate the applicability of cellular concrete. Porosity, sorption, and density are the unique physical properties of cellular concrete, which are illustrated and discussed in this section.

*Porosity*

Porosity is one of the most significant properties of cellular concrete. Many other properties of cellular concrete such as strength, durability, as well as thermal insulation, are influenced by porosity (Amran et al., 2015; Lamond and Pielert, 2006). Kearsley and Wainwright (2001) pointed out that there is a strong relationship between porosity and dry density of cellular concrete, and the porosity is mostly independent of ash type, ash content, and the insulation of the foam.

Mineral admixtures could influence the porosity of cellular concrete. A series of studies reported that mineral admixtures could be used for reducing the porosity of cellular concrete (Amran et al., 2015). For instance, the porosity reduction effect of lime powder is better than that of fly ash because of its fine particles that could enhance the compact composition of the microstructure of cellular concrete (Barbhuiya et al., 2009).

The volume of foam agent could also affect the porosity. A considerable number of studies reported that the volume of foam agents largely influenced the porosity of cellular concrete because the foam structure was highly attributed to the shape, size, air-voids distribution and volume of microspores (Ramamurthy et al., 2009; Amran et al., 2015). Moreover, excessive dosage of foam agent can expand the size of bubbles and increase the porosity of cellular concrete (Jones and Mccarthy, 2005; Amran et al., 2015).

*Sorption*

Sorption characteristics such as absorption and sorptivity are of vital importance as they affect the durability and other properties of cellular concrete (Nambiar and Ramamurthy, 2007). Absorption and sorptivity affect the durability of cellular concrete, and it was mainly determined by density, foam agent, type of mineral admixtures as well as permeability (Nambiar and Ramamurthy, 2007; Amran et al., 2015).

The water absorption influenced mainly by the total volume of pores. Specimen processing, mix composition and curing condition were the major contributing factors for sorptivity properties (Ramamurthy et al., 2009). Several studies made on aerated and foamed concrete indicated that the micro-pores and its characteristics along with mix composition had significant influences on the sorption property (Amran et al., 2015). For a given mix type of cellular concrete, sorptivity and water absorption were mainly controlled by capillary action and porosity (Nambiar and Ramamurthy, 2007).

*Density*

Cellular concrete is a low-density and homogeneous building material. Based on the previous study, the density of cellular concrete ranges from 320 to 1920 kg/m$^3$ (20-120 lb/ft$^3$) (Lamond and Pielert, 2006). For cellular concrete, density is a critical indicator of a variety of unique properties. A relationship between density and properties of cellular concrete was introduced in many previous works of literature (Jones et al., 2006; Gerasimovich et al., 2014; Long and Wang, 2015; Sayadi, 2016b).

Cellular concrete with density not exceeding 800 kg/m$^3$ (50lb/ft$^3$) was often recognized as insulating concrete or low-density concrete. The compressive strength of this group usually ranges approximately from 0.7 to 7 MPa (100-100psi). This group of cellular concrete could be used in nonstructural applications, such as firewalls, roof decks, insulation applications, and backfill materials, due to its high performance of fire resistance, water resistance or thermal and sound insulation (Lamond and Pielert, 2006; Amran et al., 2015).

For cellular concrete, the densities ranging from 800 to 1920 kg/m$^3$ (50-120lb/ft$^3$) are usually considered as a semi-structural range, sometimes, a small proportion of sand or fine aggregate has been used to improve the structural performance of cellular concrete. The compressive strength of this group ranges approximately from 3.4 to 17 MPa (500-2500psi). Cellular concrete with a density of this range is usually used for semi-structural applications such as insulation walls, floors, roofs, and nonstructural fill (Lamond and Pielert, 2006; Amran et al., 2015).

Cellular concrete with sand or fine aggregate was often considered as cellular sand concrete. The densities usually range from 800 to 1920 kg/$m^3$ (50-120lb/$ft^3$). For this group of cellular concrete, 25 MPa (3600psi) or more could be achieved for compressive strength (Lamond and Pielert, 2006; Jones and Mccarthy, 2005).

***Mechanical Properties***

Mechanical properties are recognized as one of the most significant factors in the application of cellular concrete (Amran et al., 2015). Many recent studies have investigated the relationship between mechanical properties of cellular concrete and physical properties such as density, porosity, and sorption (Lamond and Pielert, 2006; Long and Wang, 2015; Sayadi, 2016b). Other contributing factors, which are of vital importance to mechanical properties, have also been studied and summarized in previous studies, for instance, water-cement ratio, characteristics of ingredients used, foaming methods and curing procedures (Choi et al., 2007; Ramamurthy et al., 2009; Amran et al., 2015).

*Compressive Strength*

The compressive strength of cellular concrete can be influenced by many factors such as density, air content, water-cement ratio, curing condition, special admixtures and so forth (Lamond and Pielert, 2006; Ramamurthy et al., 2009; Amran et al., 2015). Cast density has a significant influence on the compressive strength of cellular concrete (Sayadi, 2016b). Much previous literature illustrated and discussed the relationship between compressive strength and density of cellular concrete (Long and Wang, 2015; Ramamurthy et al., 2009; Amran et al.,

2015; Yue et al., 2013). Experimentally, it was concluded that cast density had a direct functional relationship with compressive strength where compressive strength decreases exponentially with a reduction in cast density of cellular concrete as shown in Figure 2.3 (Ramamurthy et al., 2009; Amran et al., 2015).

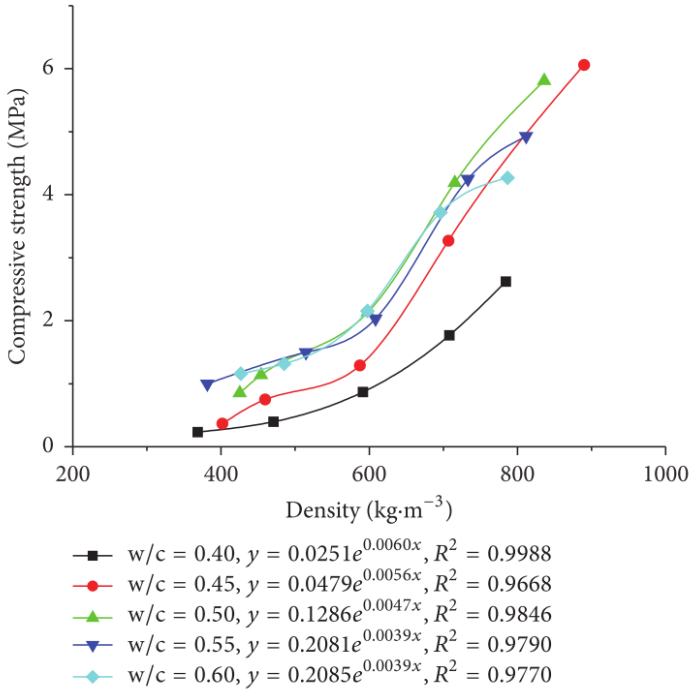


**Figure 2.3** The fitting relationships between the strength and dry density of foam concrete (adapted from Liu et al., 2016a).

Foam agent was another major controlling factor in the compressive strength of cellular concrete. A high volume of air content or a high volume of air-voids resulted in a lower density of cellular concrete (Amran et al., 2015; Risdanareni et al., 2017). Also, the type of foam agent and the foaming process had a significant influence on the uniformity of air-voids in the cellular concrete, which directly affected the compressive strength of cellular concrete (Amran et al., 2015; Kuzielová et al., 2016).

Another contributing factor to the compressive strength of foam concrete is the water-cement ratio. Liu et al. (2016a) reported that with the increase in the water-cement ratio, the compressive strength showed an inverted V-shaped variation law as Figure 2.4.

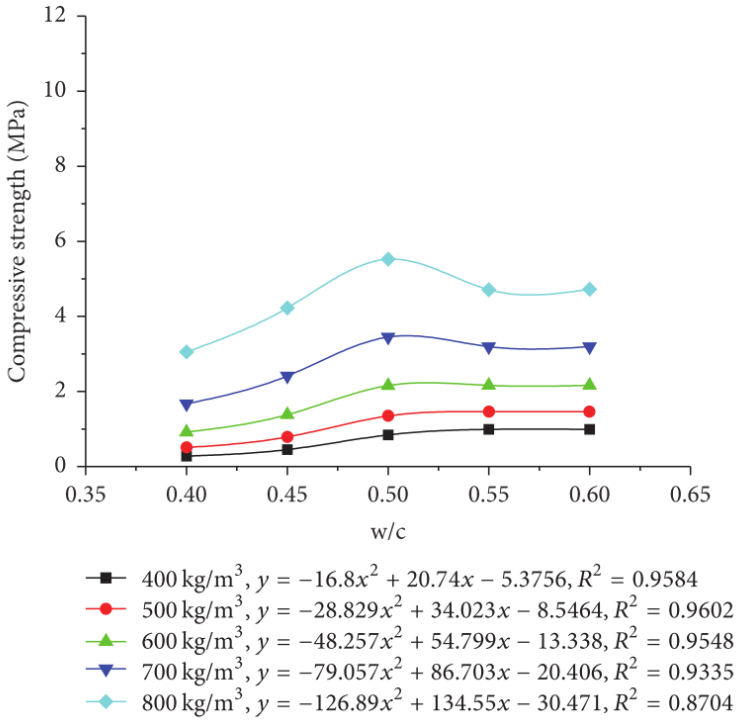


**Figure 2.4** Effect of w/c ratio on the strength of foam concrete (adapted from Liu et al., 2016a).

An excessive amount of coarse sand also had a bad influence on the compressive strength of cellular concrete; the reason was that an excessive amount of coarse sand would adversely affect the pore size or microstructure of cellular concrete, which leads to decreasing compressive strength (Amran et al., 2015). Besides, the compressive strength of cellular concrete was influenced by many other factors such as supplementary cementitious materials, curing method, steel or fiber reinforcement, and so forth.

*Flexural and Tensile Strength*

The flexural and tensile strength had a similar relationship to the compressive strength as with cellular concrete. The flexural strength of cellular concrete was typically 25-35% of the compressive strength, and the ratio of tensile strength to compressive strength was in the range of 10-15% (Lamond and Pielert, 2006; Ramamurthy et al., 2009). However, Amran et al. (2015) reported a different range of 20-40% for the ratio of tensile strength to compressive strength, which was much higher than ordinary concrete that possessed a ratio of 8-11%. The flexural and tensile strength of cellular concrete was lower than ordinary aggregate concrete and lightweight concrete with the same density (Ramamurthy et al., 2009).

The increase of flexural and tensile strength was mainly attributed to the improved density of cellular concrete (Sayadi et al., 2016b). Moreover, fiber reinforcement was a cost-efficient method to improve the flexural and tensile strength of cellular concrete in some special constructions (Jones and Mccarthy, 2005; Cai et al., 2011). A study conducted by Chen et al. (2012) showed that utilizing polypropylene (PP) fiber could increase about 31.7% of the splitting tensile strength compared to non-PP fiber foamed concrete.

*Modulus of Elasticity*

The modulus of elasticity is one of the significant mechanical properties of cellular concrete. The strain and creep behavior of cellular concrete, which are of vital significance in structural design, is determined by the modulus of elasticity (Zhang and Wang, 2016). The modulus of elasticity of cellular concrete is lower than ordinary concrete with the same density due to its porosity (Lamond and Pielert, 2006; Ramamurthy et al., 2009; Amran et al., 2015).

Previous studies also reported that the modulus of elasticity is influenced by the aggregate type and content (Jones and Mccarthy, 2005). Understand the fundamental rules of elastic modulus is of vital importance to developing cellular concrete for structural and semi-structural applications (Zhang and Wang, 2016).

The modulus of elasticity has a functional relationship with its density and compressive strength (Lamond and Pielert, 2006). In previous research, several models have been developed to correlate the modulus of elasticity with compressive strength, and density for cellular concretes (Narayanan et al., 2000). Two general forms of the models (Zhang and Wang, 2016) are shown below:

$$E_c = m \cdot f_c^{\,n}$$
$$E_c = m \cdot \rho \cdot f_c^{\,0.5} \qquad (2.1)$$

In which, *m* and *n* are fitting constants, ρ is density (usually oven-dry density, kg/m$^3$), $f_c$ is compressive strength, MPa.

Based on the equations, it can be safely concluded that the modulus of elasticity decreases with an increase in the porosity or air content of cellular concrete. In addition, the empirical equations indicated that cellular concrete with higher density results in higher compressive strength as well as a much higher modulus of elasticity. Another cost-efficient method to increase E-value in some particular applications is utilizing fiber reinforcement. The use of polypropylene fibers has been reported to increase the E-value of cellular concrete from 2 to 4 times (Jones and Mccarthy, 2005).

### *2.4.3 Functional Properties and the Application of Cellular Concrete*

Cellular concrete was widely used in many civil and structural engineering fields due to its distinctive functional properties. Thermal conductivity, freeze-thaw resistance, fire resistance, and structural applications were introduced to provide the readers with the state of art review of the applications of cellular concrete. Also, the trend to improve the structural performance of cellular concrete, and the recent development of cellular were illustrated and discussed in this section.

Functional properties have a significant influence on the application of cellular concrete. In recent years, cellular concrete shows great popularity in construction applications owing to its unique functional properties such as the high performance of thermal insulation, sound insulation, fire resistance, and sustainability (Rasheed and Prakash, 2015). Other applications of cellular concrete include: (1) road constructions; (2) cold region constructions; (3) oil spill treatment and carbon capture; (4) anti-seismic structures; (5) waterproof; (6) backfill materials; (7) chemical storage tank and so forth (Decký et al., 2016; Kadela et al., 2017; Tian et al., 2009; Tikalsky et al., 2004; Akulov et al., 2017; Hu, 2013; Xia, 2014). Furthermore, due to the recent improvement of the structural performance of cellular concrete, it becomes an excellent alternative material in structural applications (Rasheed and Prakash, 2015).

#### *Thermal Conductivity*

In general, cellular concrete has excellent thermal insulation properties due to its porosity and microstructural characteristic. Cellular concrete is a kind of lightweight concrete material

that has the thermal conductivity of up to 0.66W/m·K at the density of 1600kg/$m^3$, which is, much less than ordinary concrete with the thermal conductivity of 1.6 W/m·K at a density of 2200kg/$m^3$.

The thermal conductivity of cellular concrete is significantly influenced by moisture content (thermal conductivity of water is 25 times bigger than air) (Sayadi et al., 2016a). Some studies reported that the level of thermal insulation in cellular concrete depends on density, mineral admixtures, aggregate types, cement content and temperature of the concrete (Amran et al., 2015; Sayadi et al., 2016a).

In recent years, researchers launched many innovative studies on the thermal conductivity of cellular concrete. Liu et al. (2014) investigated the thermal conductivity of lightweight aggregate foamed geopolymer concrete. An experiment conducted by Sayadi et al. (2016a) indicated that an increase in the volume of expanded polystyrene (EPS) resulted in lower thermal conductivity. Miled and Limam (2016) first derived various analytical forms for the effective thermal conductivity of foam concretes based on homogenization schemes.

***Freeze-thaw Resistance***

The growing use of cellular concrete as construction materials and geotechnical fills put forward the question of suitable durability and better performance of cellular concrete (Tikalsky et al., 2004). Of vital importance is freeze-thaw resistance of cellular concrete in cold regions. Cellular concrete has excellent freeze-thaw resistance due to its high air content and its relatively high cement content. The microstructure or cell-like structure of cellular concrete and possible

porosity make it a high performance freeze-thaw resistance material (Lamond and Pielert, 2006). Since the air-voids are much larger than those in normal-weight concrete, the saturation and the volume of water in cellular concrete can be much higher than normal-weight concrete with the same moisture condition, the air-voids appear to act as a buffer to prevent rapid penetration, which enhances the freeze-thaw resistance of cellular concrete (Tikalsky et al., 2004; Ramamurthy et al., 2009; Amran et al., 2015). In the meantime, Tikalsky et al. (2004) provided a new method to assess the freeze-thaw resistance of cellular concrete. He also developed a modified freeze-thaw test procedure in his research.

***Fire Resistance***

Recently, cellular concrete has been widely used in building conditions with special fire resistance needs. The capacity of cellular concrete to resist fire depends on its mixture proportions, constituents, and compositions. In general, as the density decreased, the cellular concrete would increase the fire resistance, because its high air content and porosity make it an excellent material for thermal insulation (Lamond and Pielert, 2006).

Since the thermal conductivity and diffusivity are low, cellular concrete results in better fire resistance. Cellular concrete with low densities results in better fire resistance than regular concrete, and further research indicated that for cellular concrete with higher densities, this trend is inverted (Sayadi et al., 2016a). Moreover, several recent studies focused on the fire resistance of cellular concrete and its structural applications by using numerical methods and laboratory tests. For instance, Biondini and Nero (2011) created a numerical model to simulate the cellular

concrete beam under fire for nonlinear analysis. Bihina et al. (2013) studied the behavior of composite steel-concrete cellular beams under fire by using the finite element method. Wang (2013) conducted a laboratory test to determine the performance of thermal insulation and fire resistance of light ceramsite foam concrete block wall.

***Structural Application***

Critical literature reviews show that researchers from different countries have conducted many experiments to explore the structural behaviors of cellular concrete (Rasheed and Prakash, 2015), but the research on lightweight cellular concrete for structural application is still limited. The structural behavior of cellular concrete can be significantly influenced by its density and porosity (Lamond and Pielert, 2006; Amran et al., 2015). To achieve the high structural performance of cellular concrete, Jones and Mccarthy (2005) investigated the influence of relatively high plastic density ranges from 1400-1600kg/$m^3$ to structural behaviors of cellular concrete by utilizing two types of fly ash, fine fly ash, and coarse fly ash, in the mix design. Finally, the target strength 25N/$mm^2$ was achieved in the cellular concrete without any reinforcement, which showed the great potential of cellular concrete in a structural application.

The compressive and tensile strength of cellular concrete can be significantly improved by utilizing steel reinforcement (Ramamurthy et al., 2009). However, Jones and Mccarthy (2005) pointed out that carbonation-induced corrosion should be taken into serious consideration when cellular concrete with steel reinforcement was used in an exposed environment. Further research showed that hybrid-synthetic fiber, as an alternative option, has high performance reinforcement.

The compressive stress of cellular concrete with the 0.44% hybrid-synthetic fiber reinforcement improved twice compared to the ones without any reinforcement (Rasheed and Prakash, 2015). Another experiment conducted by Krämer et al. (2017) concluded that nanotubes as reinforcement are an effective method to improve further the mechanical performance of foam concretes. Moreover, the cohesion of the concrete can be improved largely by utilizing Polypropylene fiber, and a suitable quantity of the fiber can raise the strength efficiently (Cai et al., 2011).

Krämer et al. (2015) introduced a new method to enhance the performance of foam concrete by utilizing reinforced three-phase-foams, which provide strengthening through pozzolanic reaction. The results showed that the mechanical properties of foam concrete with utilizing three-phase-foams could be significantly improved. Three-Phase cellular concrete was illustrated in Figure 2.5.

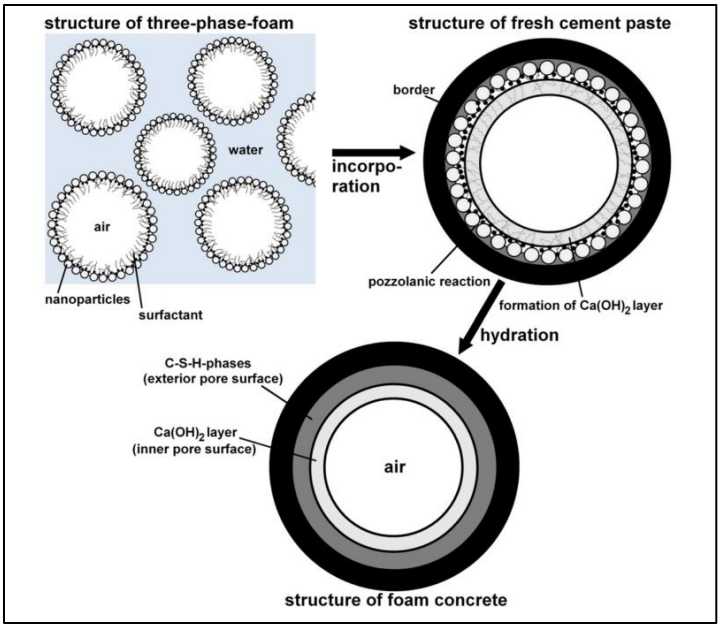


**Figure 2.5** Theory of the formation of the pore structure and hydration products of the produced foam concretes (adapted from Krämer et al., 2015).

Kadela et al. (2017) conducted a series of experiments focused on the application of cellular concrete as alternative structural materials in road pavement. The results show that the compressive and flexural strengths increased with an increase in the density of cellular concrete approximated with polynomial functions.

***Recent Development and Other Applications***

Cai et al. (2011) investigated the performance of foamed concrete influenced by utilizing magnetite mill tailings (felsite powder) and Solvay distiller waste in the mix design. The data showed that Solvay distiller waste improved the performance of foamed concrete in many aspects such as higher strength, better cohesion, less shrinkage, especially at an early age. Kashani et al. (2017) introduced a new technique for the application of recycled tire crumbs in lightweight cellular concrete. Although, the compressive strength decreased with the increasing

of tire crumbs content. The additional experiment found that the lightweight cellular concrete with tire crumb has significant advantages of excellent thermal and sound insulation, low water absorption that has a high potential in the application of auditoriums, plant rooms, offices, and hospital partitions that with a particular need for insulation properties of building materials. Akulov et al. (2017) investigated the relationship between oil contamination removal ability and the density of foam concrete. Different types of petroleum products have been used to take the tests, and five different densities of foam concrete have been adopted, 300 kg/$m^3$, 400 kg/$m^3$, 500 kg/$m^3$, 600 kg/$m^3$, 700 kg/$m^3$, 800 kg/$m^3$, to explore the oil absorption of foamed concrete. The results show that foam concrete with a density of 600kg/$m^3$ is considered the optimal choice for the oil spill elimination. A new type of cellular concrete was created by Wang et al. (2012) to improve the deformation ability and enhance its waterproof function and ductility performance for the application of cellular concrete in large-span soft rock tunnel. Decký et al. (2016) conducted an in-situ test to determine the equivalent modulus of the subgrade layer with the layer of foamed concrete. Laboratory tests and series of 3-D FEM numerical models have been conducted to find out the optimal design.

**2.5 Cellular Concrete: an Alternative Material for ACE**

Cellular concrete as a promising building material has been widely used in many areas due to its excellent performance in thermal insulation, fire resistance, water absorption, and so forth (Lamond and Pielert, 2006). In addition, the utilization of more industrial byproduct and less Portland cement in cellular concrete makes it a great economical and sustainable

construction material. Nowadays, many researchers launched comprehensive studies on cellular concrete, but the exploration of the structural properties and geotechnical fills applications of cellular concrete is still limited (Rasheed and Prakash, 2015).

Previous studies have confirmed that ACE has excellent performance in providing passive cooling for road embankment in permafrost regions (Xu and Goering, 2008). However, in many permafrost areas, the coarse gravel or crushed rocks needed for ACE construction are not readily available.

Cellular concrete as an alternative material for ACE in permafrost regions showed great potential to get higher performance and reduce the high cost of embankment construction in the permafrost region. Cellular concrete is flexible in casting; it can be manufactured in any shapes and any gradations needed to improve the cooling effect of the embankment, which would conduct a positive impact on stimulating creativity for embankment construction design at the same time.

# CHAPTER 3.0 LABORATORY TEST OF CELLULAR CONCRETE

Cellular concretes are lightweight concretes with a Portland cement finely aggregate base containing many small air cells uniformly distributed throughout the concrete. The foam volume or the porosity has a significant effect on the properties of cellular concrete. In this study, the screening test of cellular concrete was investigated with different foam content of 10%, 20%, 30%, 40%, and 50%. The initial screening test investigated the range of foam content and recommended a reasonable range for the optimal design. For optimization of mixtures, a fractional factorial design (Taguchi Methods) based on an "orthogonal array" was used to evaluate the effects of various key factors, which are fly ash, slag, and water-cementitious ratio, on the thermal properties and compressive strength of cellular concrete. The lab test design and associated experimental testing are described. The analysis results of the Taguchi design by MINITAB are presented. The optimum combination is subsequently chosen — this study aimed at developing lightweight cellular concrete considering ACE construction on permafrost foundations in Alaska.

## 3.1 Materials

Holcim Type I cement was used for all concrete mixtures. The class C fly ash and coal slag were utilized to improve the performance of cellular concrete (Figure 3.1). Besides, the Aerlite™ foaming agent, which is produced by Aerix Industries, was used in the research with a designed dilution ratio of 1:55. Foam stabilizer made of oleic acid and triethanolamine was

manipulated to stabilize the foam (Figure 3.2). The surface of the cellular concrete foam stabilizer can effectively reduce the arrangement of liquid in the double electron layer on the surface of the liquid film to surround the air, and form bubbles.


**Figure 3.1** Holcim Type I cement, coal slag, and class C fly ash.

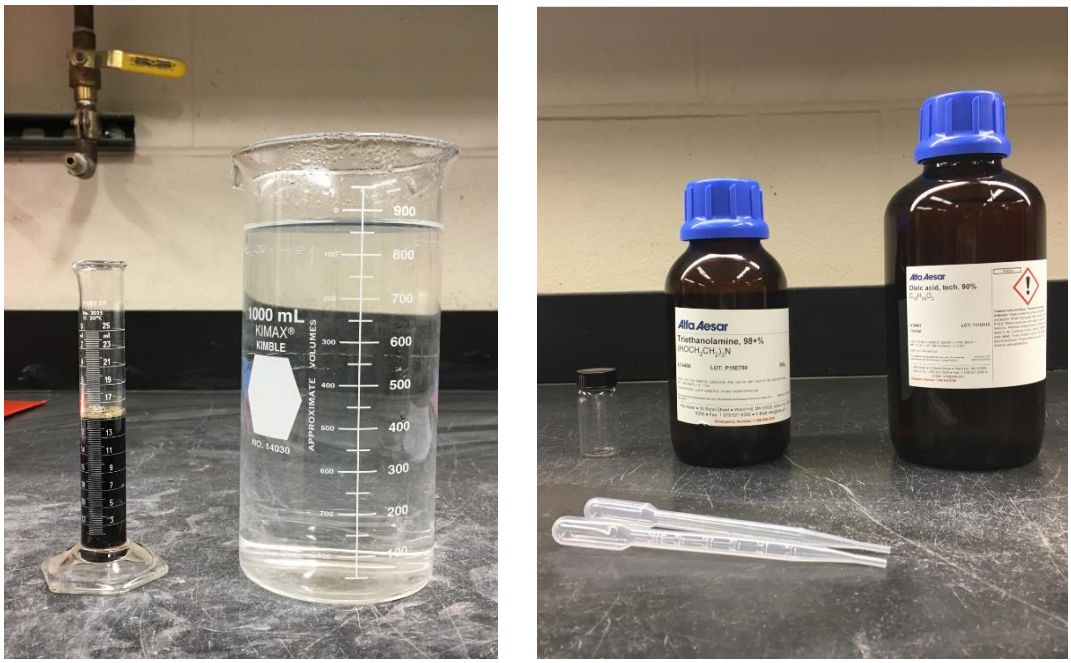


**Figure 3.2** Aerlite™ protein-based foam agent (left) and foam stabilizer (Oleic acid and Triethanolamine) (right).

The Aerlite™ foam liquid concentrate is a hybrid formula that takes the highest performing strength attributes of the protein products and combines them with the fluidity and flexibility found in the straight synthetic products. This kind of protein-based foaming agents, most commonly used in geotechnical applications, produces a lightweight cellular concrete when combined with a cement slurry. Figure 3.3 shows the generated foam and cellular concrete specimens. As shown in Figure 3.4, the specimen preparation procedures are mainly mortar preparing, mix mortar with foam, molding, and curing. The details of specimen preparation are demonstrated below.

**Figure 3.3** The generated foam (left) and cellular concrete specimens (right).

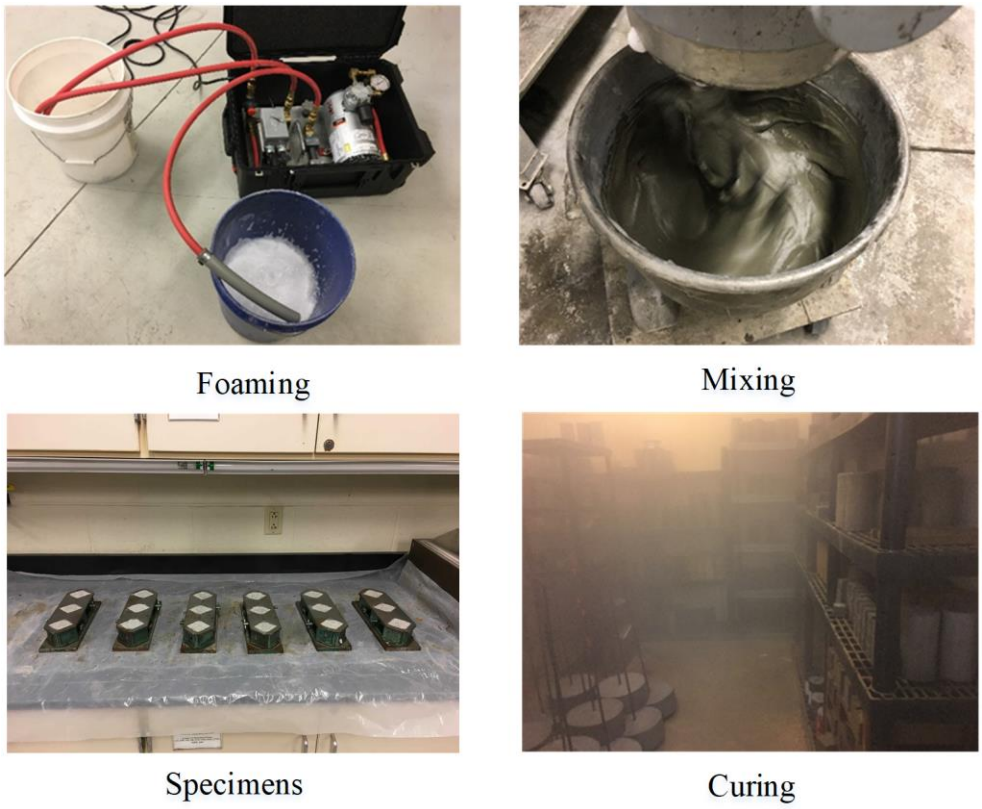


**Figure 3.4** Specimen preparation procedures.

***Cement Paste Preparing***

Use the portable laboratory foam generator to make sufficient foam. Add the masonry cement in the appropriate amounts to the mixing container, then add water on top of the dry ingredients. And then mix the foam with the paste.

***Mix Mortar with Foam***

With a trowel, break up any lumps of undispersed cement. Mix with an operating speed of 4 to 5 rad/s [40 to 50 r/min] for 5 min. While still mixing, add foam to the mortar. After that,

mix the foam mortar with an operating speed of 4 to 5 rad/s [40 to 50 r/min] over 2 min (ASTM C192, ASTM C495).

***Molding***

Several standard test specimens were chosen for investigating the various parameters. The molds applied in the lab test are cube molds, 2in×2in. In molding the specimens, place the concrete in two approximately equal layers. Tap the outside of the mold lightly 10 to 15 times with an open hand after placing each layer to close voids and release entrapped air. Overfill the mold when placing the second layer. As soon as possible after casting, strike off the top surface of each specimen and cover the specimen with a plastic bag to prevent evaporation, without marring the surface (ASTM C192).

***Curing***

For the first 24h after molding, maintain the specimens at a temperature of 21°C. After 24±2h, store the specimens in the curing room at a temperature of 21±6 °C [70±10 °F] and relative humidity of 50±30 % (ASTM C192).

**3.2 Initial Screening Test**

The cellular concrete to be developed should achieve two primary objectives: gain the relatively low thermal conductivity of cellular concrete in order to improve the thermal performance of ACE, and obtain adequate compressive strength in the cellular concrete to meet the strength requirement for ACE construction. The initial screening investigated the influence of foam contents on the physical properties of the cellular concrete.

### *3.2.1 Mix Design*

As was depicted in section 3.1, specimen preparation procedures are mainly foam generating, cement pasts preparing, mixing cement paste with foam, molding, and curing. Moreover, the mixing details in the lab tests are summarized in Tables 3.1 and 3.2. Several standard cube specimens were chosen for investigating the various parameters (Figure 3.5). Cubes specimens 2in×2in in size were used for testing the compressive strength at day 7, 14, 28, 60, 120. In addition, the thermal properties tests were conducted using the cubes (2in×2in) specimens after 28 days. The cylinder specimens (1.0in×2.5in, diameter×height) were utilized for permeability test.

**Figure 3.5** Cubic cellular concrete specimens (ASTM C192).

The mix design in this lab test focused on the influence of foam volume on the properties of cellular concrete. The cellular concrete mix is a combination of cement, water, foam, and foam stabilizer. This study strives to find the perfect proportions of these ingredients to optimize concrete mixes and gain workability, compressive strength, thermal conductivity, and other

desirable properties. As was shown in Table 3.1, the water-cement ratio is 0.45 and foam volume of 10%, 20%, 30%, 40%, and 50% were chosen in the mix design.

**Table 3.1** Cellular concrete mix design considers different foam content.

| No. | Variable | Unit | C10 | C20 | C30 | C40 | C50 | Note |
|---|---|---|---|---|---|---|---|---|
| 1 | Foam | % | 10 | 20 | 30 | 40 | 50 | by volume of cellular concrete |
| 2 | w/c | --- | 0.45 | 0.45 | 0.45 | 0.45 | 0.45 | Water-cement ratio (by weight) |
| 3 | Portland cement | % | 100 | 100 | 100 | 100 | 100 | by weight of cementitious materials |

**Table 3.2** The batch weights of cellular concrete with different foam content.

| Specimen ID | Mixture Component | Batch Weights | | | | |
|---|---|---|---|---|---|---|
| | | Full batch | Placing batch | Matric Unit | Placing batch | Lab Unit |
| C10 | Cement | 1172.25 | 4.689 | kg | 4689 | g |
| | Net water | 523.56 | 2.094 | kg | 2094 | g |
| | Foam | 0.1 | 0.0004 | $m^3$ | 400 | ml |
| C20 | Cement | 1042.31 | 4.169 | kg | 4169 | g |
| | Net water | 461.14 | 1.845 | kg | 1845 | g |
| | Foam | 0.2 | 0.0008 | $m^3$ | 800 | ml |
| C30 | Cement | 911.81 | 3.647 | kg | 3647 | g |
| | Net water | 398.47 | 1.594 | kg | 1594 | g |
| | Foam | 0.3 | 0.0012 | $m^3$ | 1200 | ml |
| C40 | Cement | 781.31 | 3.125 | kg | 3125 | g |
| | Net water | 335.79 | 1.343 | kg | 1343 | g |
| | Foam | 0.4 | 0.0016 | $m^3$ | 1600 | ml |
| C50 | Cement | 651.37 | 2.605 | kg | 2605 | g |
| | Net water | 273.37 | 1.093 | kg | 1093 | g |
| | Foam | 0.5 | 0.0020 | $m^3$ | 2000 | ml |

### *3.2.2 Physical Properties Tests*

#### *Flow Table Test*

Workability refers to the ease of placing, consolidating, and finishing freshly placed concrete without segregation. The initial workability test was done using the consistency definitions described in ASTM C1107. The consistency is classified into three categories (plastic, flowable, and fluid) according to ASTM C1107. Based on the flowability measurement by ASTM C1437, the flow table test was conducted in the lab (Figure 3.6).

**Figure 3.6** Flow table test and accessories to run the test (ASTM C1437).

The hand-driven flow table has a 10inches diameter cast bronze table/platen. It includes the standard cast bronze flow mold (2 3/4″ top dia.×2″ High×4″ bottom dia.). The hand-driven flow table determines the consistency of cellular concrete pastes. The flow of the grout was measured on the standard flow table after three drops in 2 seconds due to the high flowability of cellular concrete pastes. It took 7 and 15 mins to measure after mixing.

***Density Measurement***

*Fresh Density*

After the first 24h, the specimens were demolded, and an electronic scale was used to measure the fresh density of the cellular concrete. To minimize the accidental error, a set of 10 specimens was measured at a time to calculate the fresh density of specimens (Figure 3.7).


**Figure 3.7** Density measurement by the electronic scale.

*Oven-Dry Density*

The oven-dry density of cellular concrete can be determined as below. Mold 5 companion specimens for oven-dry density measurement at the same time. Cure the companion specimens, except dry the companion specimens at the age of 28 days in an oven at 110±5℃ and weigh at 24-h intervals until the loss in weight does not exceed 1% in a 24-h period. Determine the mass and dimensions of the oven-dry specimens and calculate the density from the average data obtained (ASTM C495).

***Permeability Test***

Permeability test is a measurement of the ability of cellular concrete to allow fluids to pass through it. The permeability of a porous medium is related to the porosity, but also the shapes of the voids in the porous medium and their level of connectedness. In this study, the permeability test was conducted in the lab by Isco pump and core holder (Figure 3.8) under created high water pressure environment in the core holder. The maximum water pressure was set as 1000psi. With the accompanying Figure 3.9, the cylinder specimens (1.0in×2.5in, Diameter×height) were used in the permeability test.

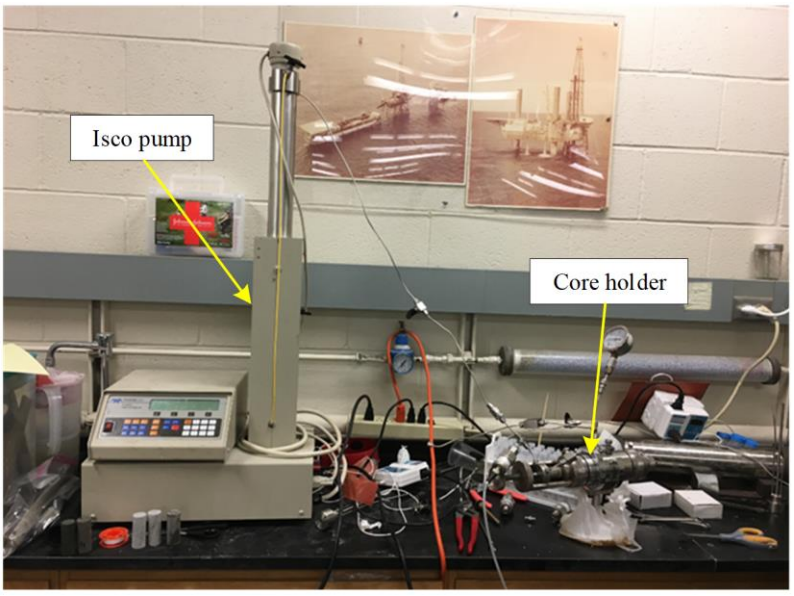


**Figure 3.8** Permeability test using Isco pump and core holder.


**Figure 3.9** Specimens for the permeability test.

***Compressive Strength Test***

For the evaluation of compressive strength, 2in×2in cube specimens were prepared according to ASTM C109 and C1107. The 200 Kip Tinius-Olsen Universal Testing Machine (Figure 3.10) was operated to test the compressive strength of the cubic specimens at several ages: day 7, 14, 28, 60, and 120 (ASTM C39, C495, C109).


**Figure 3.10** Tinius-Olsen Universal Testing Machine for the compressive strength test.

The cubic specimens were kept in the molds for 24h, and then they were demolded and sent to the curing room until the age of testing. Figure 3.11 indicates the compressive strength test and the specimen failure under peak load.

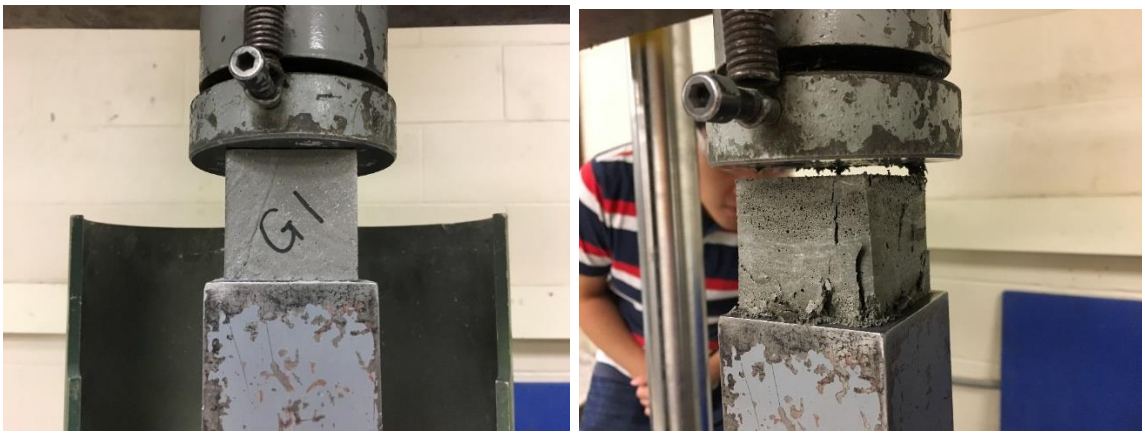


**Figure 3.11** Compressive strength cube specimens (left) and cube specimen after test via ASTM C109 (right).

***Thermal Properties Test***

Thermal properties, especially thermal conductivity and specific capacity are key factors in the ACE performance. An experimental study was conducted to investigate the thermal

conductivity, thermal diffusivity, and specific heat capacity of cellular concrete with foam volume of 10%, 20%, 30%, 40%, and 50%. The Hot Disk TPS 500S (Figure 3.12) was selected to investigate the thermal properties of cellular concrete specimens. The room temperature sample holder used in the test consists of a sample and sensor holder made of stainless steel (Figure 3.12), and a Kapton insulated sensor 5501 was utilized for thermal properties measurement.

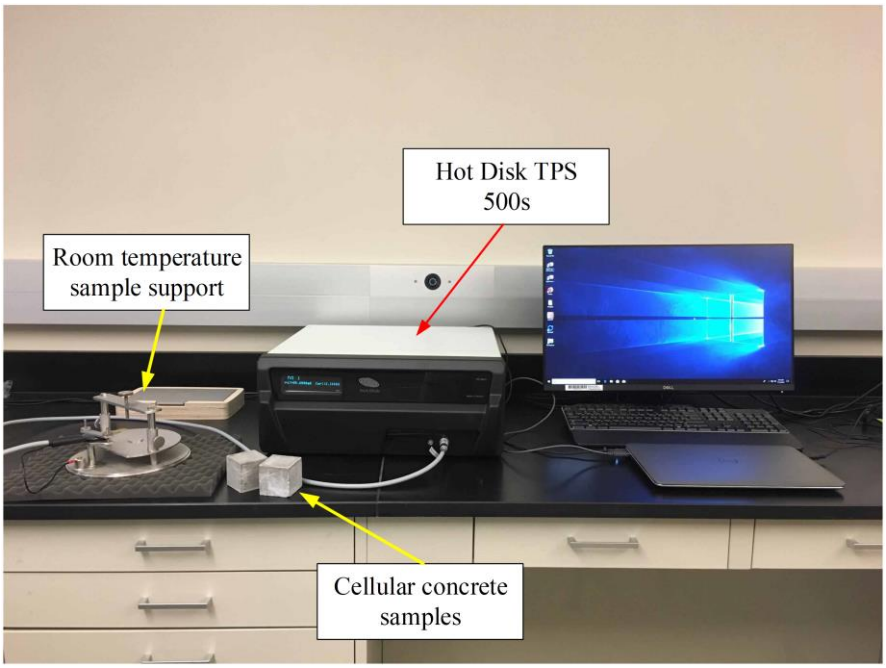


**Figure 3.12** Hot Disk TPS 500s for thermal properties test.

### *3.2.3 Results and Analysis*

#### *Workability*

As cellular concrete cannot be subjected to compaction or vibration, the cellular concrete should have sufficient flowability and self-compatibility. The workability of cellular concrete is

affected by the water-cement ratio in the base mix and amount of foam in the mix. The results of the flow table test were shown in Table 3.3.

Both of Table 3.3 and Figure 3.13 illustrate that the flowability reduced with an increase in the volume of foam in the mix. The reason is that by increasing the foam content, the density of cellular concrete paste will reduce. Higher air content resulted in greater cohesion as well. Besides, the stiffness of mix will increase due to the adhesion between bubbles and solid particles in the cellular concrete pastes.

**Table 3.3** Results of flow table test (ASTM C1437).

| Grout | Number of Drops | Flow at 7 min, Percent | Flow at 15 min, Percent |
|---|---|---|---|
| C10 | 3 | 102 | 65 |
| C20 | 3 | 96 | 62 |
| C30 | 3 | 91 | 51 |
| C40 | 3 | 83 | 53 |
| C50 | 3 | 74 | 48 |

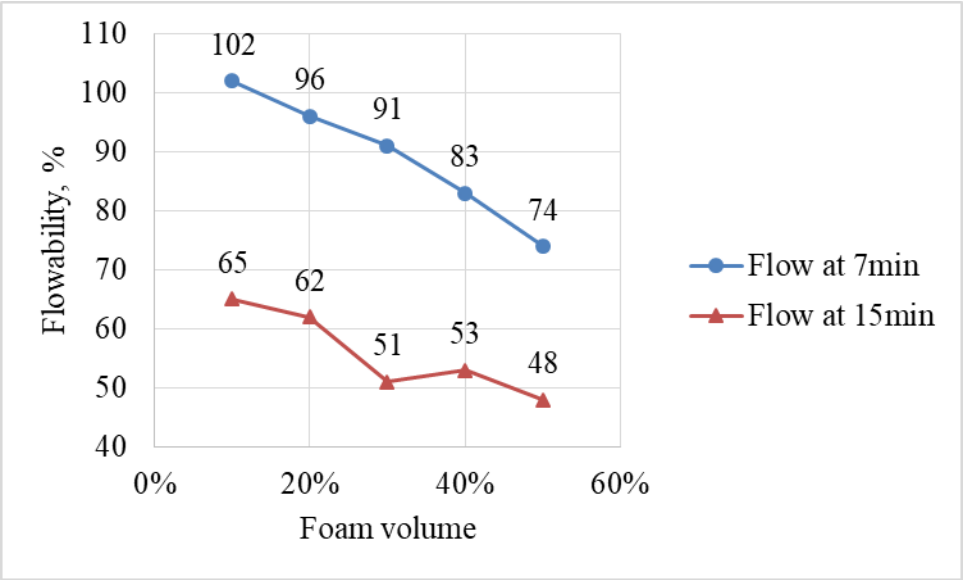


**Figure 3.13** Flowability versus foam volume.

***Density***

Density can be either fresh or oven-dry state. At certain times, the fresh density may not be accurate, because the moisture content in the cellular concrete may vary from flexible air void content and surroundings. In this test, the fresh density and oven-dry density are shown in Table 3.4 and Table 3.5, respectively.

**Table 3.4** Fresh density of the specimens.

| Specimen ID | Specimen Number | Mass (kg) | Volume ($m^3$) | Density ($kg/m^3$) | Density ($lbs/ft^3$) |
|---|---|---|---|---|---|
| C10 | 10 | 2.2278 | $1.31 \times 10^{-3}$ | 1699 | 106.1 |
| C20 | 10 | 1.9508 | $1.31 \times 10^{-3}$ | 1488 | 92.9 |
| C30 | 10 | 1.7321 | $1.31 \times 10^{-3}$ | 1321 | 82.5 |
| C40 | 10 | 1.4972 | $1.31 \times 10^{-3}$ | 1142 | 71.3 |
| C50 | 10 | 1.1496 | $1.31 \times 10^{-3}$ | 877 | 54.7 |

**Table 3.5** Oven-dry density of the specimens.

| Specimen ID | Specimen Number | Mass (kg) | Volume ($m^3$) | Density ($kg/m^3$) | Density ($lbs/ft^3$) |
|---|---|---|---|---|---|
| C10 | 10 | 1.9500 | $1.31 \times 10^{-3}$ | 1487 | 92.9 |
| C20 | 10 | 1.7502 | $1.31 \times 10^{-3}$ | 1335 | 83.3 |
| C30 | 10 | 1.5746 | $1.31 \times 10^{-3}$ | 1201 | 75.0 |
| C40 | 10 | 1.4198 | $1.31 \times 10^{-3}$ | 1083 | 67.6 |
| C50 | 10 | 1.0446 | $1.31 \times 10^{-3}$ | 797 | 49.7 |

Figure 3.14 shows the influence of foam content on the fresh density and oven-dry density of cellular concrete. Accordingly, the density decreased linearly with an increase in the volume of foam in the mix. When the foam content increased from 10% to 50%, the fresh density of the cellular concrete decreased from 1699$kg/m^3$ to 877$kg/m^3$ and the oven-dry density

of the cellular concrete decreased from 1487kg/m$^3$ to 797kg/m$^3$. As the foam content increased, the water content of the foam concrete decreased.

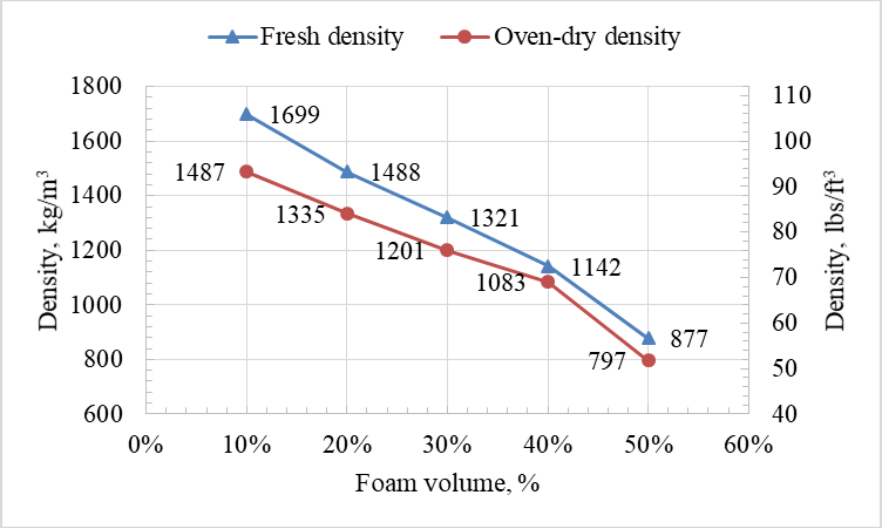


**Figure 3.14** Density versus foam volume.

***Permeability***

Five sets of cylinder specimens (1.0in×2.5in, Diameter×height) were utilized in the permeability test. As is shown in Table 3.6, the permeability of the five sets of specimens, C10, C20, C30, C40, and C50 are 0.0 m$^2$, which means the cellular concrete in the test are waterproof concrete that will not allow water to pass through it and the air voids are not connected.

**Table 3.6** Permeability of the specimens.

| Specimen ID | Water pressure (psi) | Permeability (m$^2$) |
|---|---|---|
| C10 | 1000 | 0.0 |
| C20 | 1000 | 0.0 |
| C30 | 900 | 0.0 |
| C40 | 700 | 0.0 |
| C50 | 500 | 0.0 |

The non-permeability feature of cellular concrete made it an excellent choice for the application in cold regions. Due to the non-permeability feature of cellular concrete, the freeze

and thaw resistance ability of cellular concrete could be much higher than ability of permeable ones. Therefore, foam concrete as a building material has excellent durability in cold regions.

***Compressive Strength***

The compressive strength is considered as one of the most important factors to measure applicability of foamed concrete at the hardened state. Tables 3.7-3.11 indicate the compressive strength of cellular concrete with foam content of 10%, 20%, 30%, 40%, and 50% at the age of 7, 14, 28, 60, and 120 days, respectively. 2in×2in cube specimens as was described in ASTM C109 were prepared for the evaluation of compressive strength of the cellular concrete with different foam content.

**Table 3.7** 7-days compressive strength test results.

| Specimen ID | Age | No. | Compressive Strength | | Average Compressive Strength | |
|---|---|---|---|---|---|---|
| | (day) | | (psi) | (MPa) | (psi) | (MPa) |
| C10 | 7 | 1 | 4972 | 34.3 | 4884 | 33.7 |
| | | 2 | 4760 | 32.8 | | |
| | | 3 | 4919 | 33.9 | | |
| C20 | 7 | 1 | 2653 | 18.3 | 2647 | 18.3 |
| | | 2 | 2626 | 18.1 | | |
| | | 3 | 2662 | 18.4 | | |
| C30 | 7 | 1 | 1674 | 11.5 | 1660 | 11.4 |
| | | 2 | 1618 | 11.2 | | |
| | | 3 | 1688 | 11.6 | | |
| C40 | 7 | 1 | 547 | 3.8 | 579 | 4.0 |
| | | 2 | 549 | 3.8 | | |
| | | 3 | 640 | 4.4 | | |
| C50 | 7 | 1 | 371 | 2.6 | 365 | 2.5 |
| | | 2 | 363 | 2.5 | | |
| | | 3 | 360 | 2.5 | | |

**Table 3.8** 14-days compressive strength test results.

| Specimen ID | Age | No. | Compressive Strength | | Average Compressive Strength | |
|---|---|---|---|---|---|---|
| | (day) | | (psi) | (MPa) | (psi) | (MPa) |
| C10 | 14 | 1 | 5560 | 38.3 | 5393 | 37.2 |
| | | 2 | 5463 | 37.7 | | |
| | | 3 | 5156 | 35.5 | | |
| C20 | 14 | 1 | 2876 | 19.8 | 2871 | 19.8 |
| | | 2 | 2905 | 20.0 | | |
| | | 3 | 2833 | 19.5 | | |
| C30 | 14 | 1 | 1936 | 13.3 | 2000 | 13.8 |
| | | 2 | 2133 | 14.7 | | |
| | | 3 | 1931 | 13.3 | | |
| C40 | 14 | 1 | 847 | 5.8 | 764 | 5.3 |
| | | 2 | 775 | 5.3 | | |
| | | 3 | 669 | 4.6 | | |
| C50 | 14 | 1 | 511 | 3.5 | 535 | 3.7 |
| | | 2 | 533 | 3.7 | | |
| | | 3 | 562 | 3.9 | | |

**Table 3.9** 28-days compressive strength test results.

| Specimen ID | Age | No. | Compressive Strength | | Average Compressive Strength | |
|---|---|---|---|---|---|---|
| | (day) | | (psi) | (MPa) | (psi) | (MPa) |
| C10 | 28 | 1 | 6137 | 42.3 | 6198 | 42.7 |
| | | 2 | 6113 | 42.1 | | |
| | | 3 | 6345 | 43.7 | | |
| C20 | 28 | 1 | 3023 | 20.8 | 3089 | 21.3 |
| | | 2 | 2845 | 19.6 | | |
| | | 3 | 3399 | 23.4 | | |
| C30 | 28 | 1 | 2534 | 17.5 | 2481 | 17.1 |
| | | 2 | 2502 | 17.3 | | |
| | | 3 | 2408 | 16.6 | | |
| C40 | 28 | 1 | 828 | 5.7 | 910 | 6.3 |
| | | 2 | 972 | 6.7 | | |
| | | 3 | 930 | 6.4 | | |
| C50 | 28 | 1 | 564 | 3.9 | 578 | 4.0 |
| | | 2 | 582 | 4.0 | | |
| | | 3 | 589 | 4.1 | | |

**Table 3.10** 60-days compressive strength test results.

| Specimen ID | Age | No. | Compressive Strength | | Average Compressive Strength | |
|---|---|---|---|---|---|---|
| | (day) | | (psi) | (MPa) | (psi) | (MPa) |
| C10 | 60 | 1 | 6677 | 46.0 | 6626 | 45.7 |
| | | 2 | 6469 | 44.6 | | |
| | | 3 | 6733 | 46.4 | | |
| C20 | 60 | 1 | 3713 | 25.6 | 3726 | 25.7 |
| | | 2 | 3568 | 24.6 | | |
| | | 3 | 3896 | 26.9 | | |
| C30 | 60 | 1 | 2626 | 18.1 | 2767 | 19.1 |
| | | 2 | 2877 | 19.8 | | |
| | | 3 | 2798 | 19.3 | | |
| C40 | 60 | 1 | 1276 | 8.8 | 1352 | 9.3 |
| | | 2 | 1353 | 9.3 | | |
| | | 3 | 1426 | 9.8 | | |
| C50 | 60 | 1 | 686 | 4.7 | 666 | 4.6 |
| | | 2 | 721 | 5.0 | | |
| | | 3 | 591 | 4.1 | | |

**Table 3.11** 120-days compressive strength test results.

| Specimen ID | Age | No. | Compressive Strength | | Average Compressive Strength | |
|---|---|---|---|---|---|---|
| | (day) | | (psi) | (MPa) | (psi) | (MPa) |
| C10 | 120 | 1 | 6810 | 47.0 | 6832 | 47.1 |
| | | 2 | 6807 | 46.9 | | |
| | | 3 | 6880 | 47.4 | | |
| C20 | 120 | 1 | 4627 | 31.9 | 4651 | 32.1 |
| | | 2 | 4717 | 32.5 | | |
| | | 3 | 4608 | 31.8 | | |
| C30 | 120 | 1 | 2918 | 20.1 | 2970 | 20.5 |
| | | 2 | 2988 | 20.6 | | |
| | | 3 | 3004 | 20.7 | | |
| C40 | 120 | 1 | 1751 | 12.1 | 1755 | 12.1 |
| | | 2 | 1753 | 12.1 | | |
| | | 3 | 1762 | 12.1 | | |
| C50 | 120 | 1 | 744 | 5.1 | 756 | 5.2 |
| | | 2 | 779 | 5.4 | | |
| | | 3 | 744 | 5.1 | | |

*Effect of Age*

Figure 3.15 demonstrated the development of compressive strength with age for cellular concrete. The compressive strength of cellular concrete with different foam content in the mixes displayed a continuous increase with age. The rate of compressive strength development was greater initially and decreased as age increased. Comparison of the strength at day 28 and day 120 indicated that at the latter age, all mixes showed appreciable improvement in compressive strength. The 28-days compressive strength of cellular concrete with foam content of 10% to 50% ranges from 578 psi (4.0MPa) to 6198 psi (42.7MPa). As can be seen from Table 3.9 the compressive strength of specimen with foam content of 20%, 30%, and 40% at the age of 28-days is 3089psi (21.3MPa), 2481psi (17.1MPa), and 910psi (6.3MPa), respectively. In addition, the 28-days compressive strength of cellular concrete with the foam content ranges from 20% to 40% can meet the requirement for the ACE construction practice in cold regions.

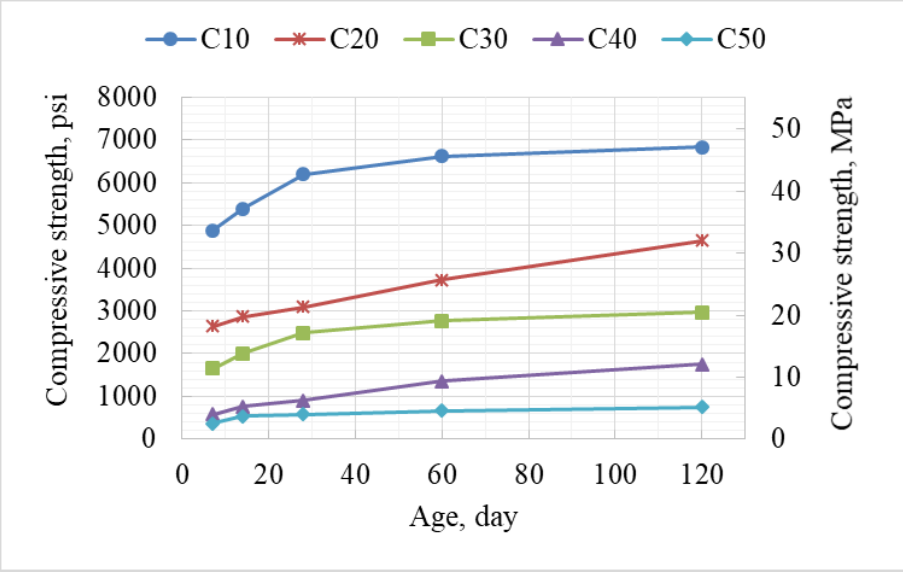


**Figure 3.15** Compressive strength versus time for cellular concrete.

*Effect of Foam Volume*

The compressive strength of cellular concretes with different foam volumes are presented in Figure 3.16 and 3.17. The strength of cellular concrete appears to increase exponentially with a decrease in foam volume. However, for cellular concretes with different densities, the increasing range is different (Figure 3.17). When the foam volume was 10%, the compressive strength increased by approximately 40% from 7-days to 120-days. When the foam volume was 50%, the compressive strength increased by approximately 100% from 7-days to 120-days. The foam content has a significant influence on the compressive strength of cellular concrete.

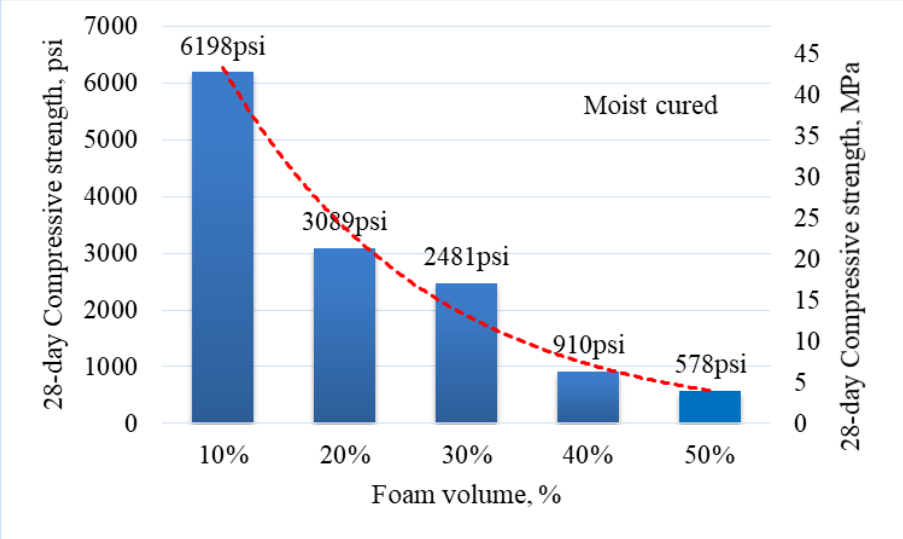


**Figure 3.16** Compressive strength versus foam volume (28 days).

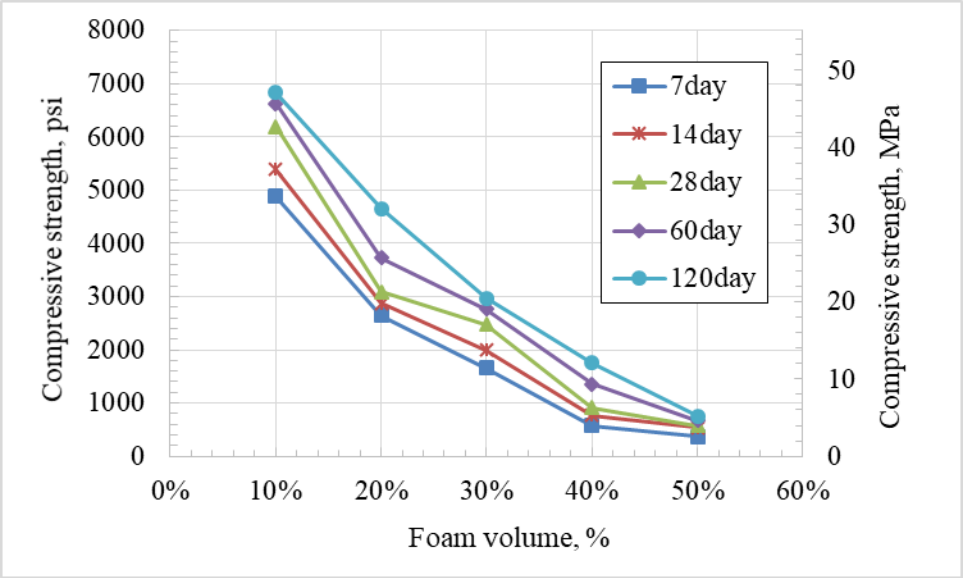


**Figure 3.17** Compressive strength versus foam volume.

*Effect of Density*

The compressive strength of cellular concrete with different oven-dry densities is presented in Figure 3.18. The strength of cellular concrete appeared to increase with a rising in concrete density. With the ascent of density, the compressive strength of cellular concrete increase slowly and then become fast. Previous studies indicated that within specific density ranges, this relationship could be linear, but for the entire possible range of cellular concrete density, it is a curvilinear relationship (Chen, 2012).

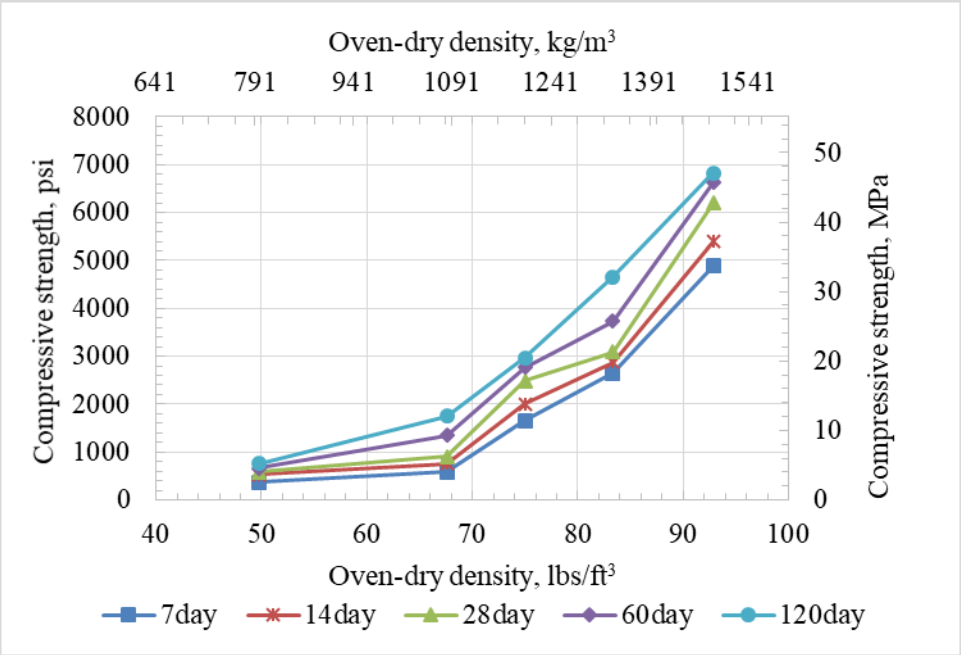


**Figure 3.18** Compressive strength versus density for cellular concrete.

***Thermal Properties***

Cellular concrete has excellent thermal insulating properties due to its cellular microstructure. The thermal properties, especially, thermal conductivity and specific heat capacity of building materials, have significant influence on the cooling effect of air convection embankment. By using the Hot Disk TPS 500s, the transient thermal conductivity, thermal diffusivity, and specific heat capacity of cellular concrete with different foam contents were investigated. The testing results were presented in Table 3.12 to Table 3.16.

**Table 3.12** Thermal properties of cellular concrete (Specimen: C10).

| Specimen ID | Number | Temperature (℃) | Thermal Conductivity (W/m·℃) | Thermal Diffusivity ($mm^2/s$) | Specific Heat Capacity ($MJ/m^3·℃$) |
|---|---|---|---|---|---|
| C10 | 1 | 21.0 | 0.9591 | 0.4774 | 2.009 |
| | 2 | 21.0 | 0.9337 | 0.4451 | 2.097 |
| | 3 | 21.0 | 0.9364 | 0.4496 | 2.083 |
| | 4 | 21.0 | 0.9335 | 0.4429 | 2.108 |
| | 5 | 21.0 | 0.9351 | 0.4545 | 2.058 |
| | Average | 21.0 | 0.9396 | 0.4539 | 2.071 |
| | St.dev | 0.0 | 0.0098 | 0.0124 | 0.035 |

**Table 3.13** Thermal properties of cellular concrete (Specimen: C20).

| Specimen ID | Number | Temperature (℃) | Thermal Conductivity (W/m·℃) | Thermal Diffusivity ($mm^2/s$) | Specific Heat Capacity ($MJ/m^3·℃$) |
|---|---|---|---|---|---|
| C20 | 1 | 21.0 | 0.8297 | 0.5583 | 1.486 |
| | 2 | 21.0 | 0.8312 | 0.5581 | 1.489 |
| | 3 | 21.0 | 0.8332 | 0.5649 | 1.475 |
| | 4 | 21.0 | 0.8310 | 0.5522 | 1.505 |
| | 5 | 21.0 | 0.8305 | 0.5503 | 1.509 |
| | Average | 21.0 | 0.8311 | 0.5568 | 1.493 |
| | St.dev | 0.0 | 0.0012 | 0.0052 | 0.013 |

**Table 3.14** Thermal properties of cellular concrete (Specimen: C30).

| Specimen ID | Number | Temperature (℃) | Thermal Conductivity (W/m·℃) | Thermal Diffusivity ($mm^2/s$) | Specific Heat Capacity ($MJ/m^3·℃$) |
|---|---|---|---|---|---|
| C30 | 1 | 21.0 | 0.6849 | 0.5948 | 1.151 |
| | 2 | 21.0 | 0.6850 | 0.5987 | 1.144 |
| | 3 | 21.0 | 0.6837 | 0.5971 | 1.145 |
| | 4 | 21.0 | 0.6859 | 0.6041 | 1.135 |
| | 5 | 21.0 | 0.6864 | 0.6033 | 1.138 |
| | Average | 21.0 | 0.6852 | 0.5996 | 1.143 |
| | St.dev | 0.0 | 0.0009 | 0.0036 | 0.006 |

**Table 3.15** Thermal properties of cellular concrete (Specimen: C40).

| Specimen ID | Number | Temperature (℃) | Thermal Conductivity (W/m·℃) | Thermal Diffusivity ($mm^2/s$) | Specific Heat Capacity ($MJ/m^3 \cdot ℃$) |
|---|---|---|---|---|---|
| C40 | 1 | 21.0 | 0.4305 | 0.6269 | 0.6867 |
| | 2 | 21.0 | 0.4304 | 0.6268 | 0.6866 |
| | 3 | 21.0 | 0.4298 | 0.6255 | 0.6871 |
| | 4 | 21.0 | 0.4314 | 0.6664 | 0.6474 |
| | 5 | 21.0 | 0.4281 | 0.6110 | 0.7006 |
| | Average | 21.0 | 0.4300 | 0.6313 | 0.6817 |
| | St.dev | 0.0 | 0.0011 | 0.0185 | 0.0179 |

**Table 3.16** Thermal properties of cellular concrete (Specimen: C50).

| Specimen ID | Number | Temperature (℃) | Thermal Conductivity (W/m·℃) | Thermal Diffusivity ($mm^2/s$) | Specific Heat Capacity ($MJ/m^3 \cdot ℃$) |
|---|---|---|---|---|---|
| C50 | 1 | 21.0 | 0.3722 | 0.6932 | 0.5498 |
| | 2 | 21.0 | 0.3680 | 0.6898 | 0.5506 |
| | 3 | 21.0 | 0.3684 | 0.6921 | 0.5469 |
| | 4 | 21.0 | 0.3691 | 0.6966 | 0.5512 |
| | 5 | 21.0 | 0.3701 | 0.6939 | 0.5496 |
| | Average | 21.0 | 0.3696 | 0.6931 | 0.5496 |
| | St.dev | 0.0 | 0.0015 | 0.0025 | 0.0017 |

The thermal conductivity and specific heat capacity of cellular concrete with different foam volumes are presented in Figure 3.19 and Figure 3.20, respectively. As can be seen, the thermal conductivity and specific heat capacity of cellular concrete appeared to decrease linearly with an increase in foam content. The thermal conductivity of cellular concrete specimens with foam content of 10% to 50% at the age of 28-days ranges from 0.9396 W/m·℃ to 0.3696 W/m·℃. The thermal conductivity of cellular concrete with foam volume of 50% is two-fifths of that of cellular concrete with foam volume of 10%. Simultaneously, the specific heat capacity of cellular concrete specimens with foam volume of 10% to 50% ranges from 2.071 $MJ/m^3$ to

0.5496 MJ/m$^3$. With the foam content of cellular concrete increased from 10% to 50%, the specific heat capacity decreased by 0.73 times.

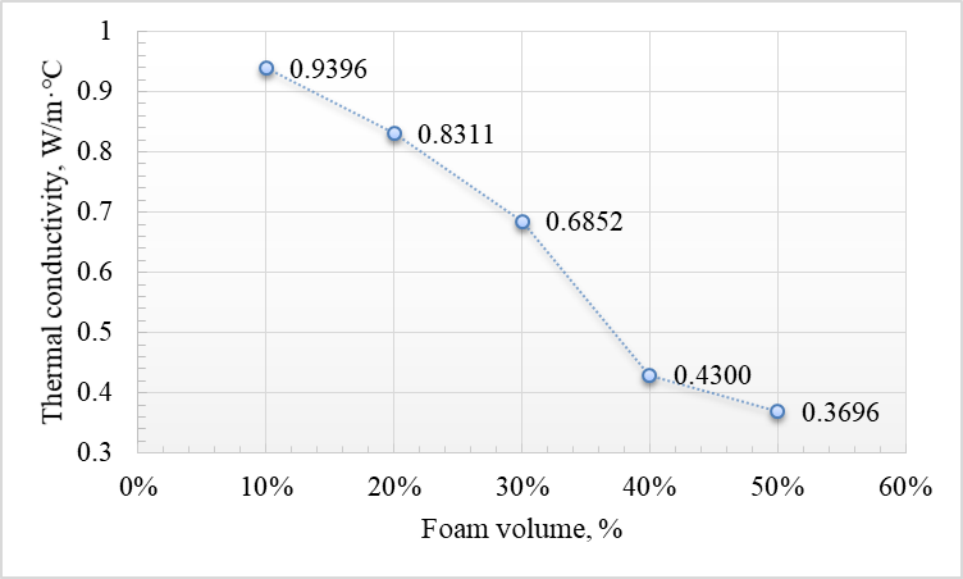


**Figure 3.19** Thermal conductivity versus foam volume.

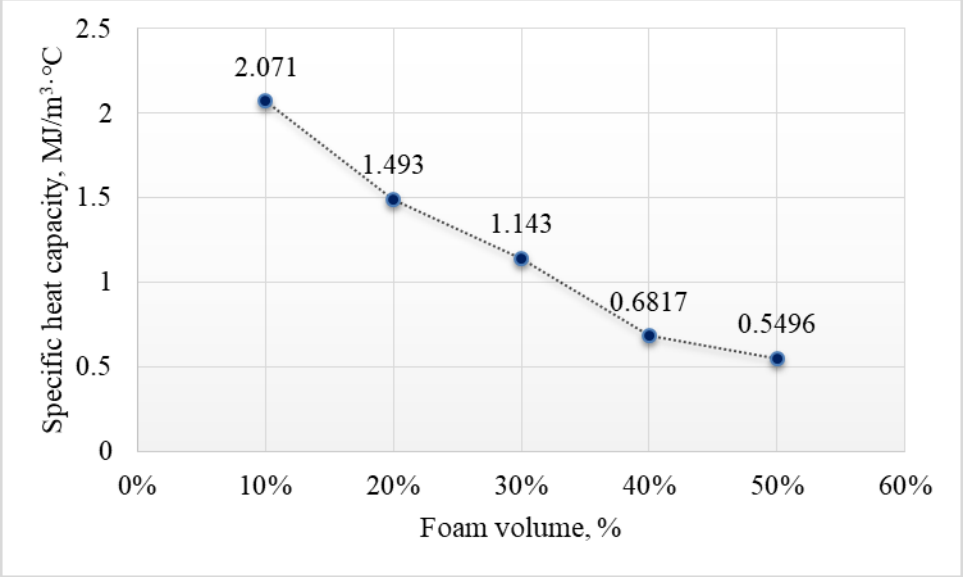


**Figure 3.20** Specific heat capacity versus foam volume.

Figure 3.21 indicates the thermal diffusivity of cellular concrete with different foam volumes. The thermal diffusivity of cellular concrete appeared to increase with a linear increase in foam volumes. When the foam content increased from 10% to 50%, the thermal diffusivity increase 1.5 times from the cellular concrete contained 10% foam volume.

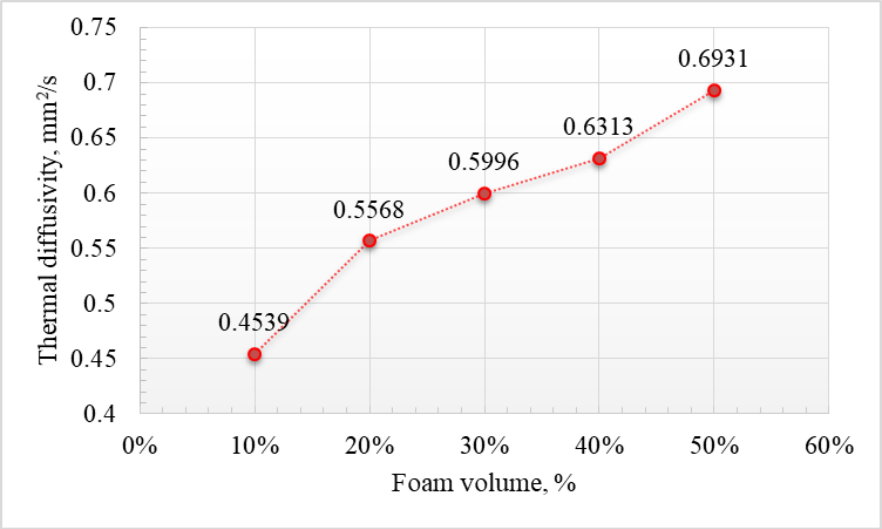


**Figure 3.21** Thermal diffusivity versus foam volume.

### *3.2.4 Conclusions and Recommendations*

As discussed above, cellular concrete as embankment materials possesses good thermal insulation property and lower sorptivity properties while producing adequate compressive strength for embankment construction. The cellular concrete with foam content of 30% to 40% is recommended as an alternative material for ACE construction. Cellular concrete in this range can guarantee sufficient strength and superior thermal insulation properties. Also, the cellular concrete with using cementitious materials of this range of foam content will be further discussed in the following chapter.

## 3.3 Optimization Test

### *3.3.1 Taguchi Methods*

The technique of laying out the conditions of experiments involving multiple factors was first proposed by Sir R.A.Fisher, which is popularly known as the factorial design of experiments. Since most experiments usually involve a significant number of factors, which means a large number of experiments. Dr. Genichi Taguchi, who is regarded as the foremost proponent of robust parameter design, constructed a particular set of general design guidelines for factorial experiments to reduce the number of experiments to a practical level, which is the famous Taguchi method. The Taguchi method is an engineering method for product or process design that focuses on minimizing variation and/or sensitivity to noise. The Taguchi design also known as an orthogonal array in a fractional factorial matrix that ensures a balanced comparison of levels of any factor.

### *3.3.2 Taguchi Design and Mix Proportion*

In the Taguchi design analysis, each factor can be evaluated independently without all other factors. Each column in the orthogonal array represents a specific factor with two or more levels. Each row represents a run. The influence of four different independent variables, foam volume, water-cementitious ratio, fly ash, and slag, on the properties of cellular concrete was investigated in the test. Each variable having three set level values, the standard L9 Taguchi design was chosen for an experiment. Table 3.17 and Table 3.18 display the L9 Taguchi design (orthogonal array), and the L9 ($3^4$) orthogonal array is meant for understanding the effect of 4

independent factors each having 3-factor level values. $3^4$ means four factors with two levels each. If the full factorial design were used, it would have $3^4$=81 runs. The L9 ($3^4$) array only requires eight runs — a fraction of the full factorial design. This array is orthogonal and factor levels are weighted equally across the entire design. With the following Table 3.18, the table columns represent the control factors, the table rows represent the runs (combination of factor levels), and each table cell represents the factor level for that run.

**Table 3.17** Parameters and their variation levels.

| | Variable | unit | Level 1 | Level 2 | Level 3 | Note |
|---|---|---|---|---|---|---|
| 1 | Foam | % | 30 | 35 | 40 | by volume of cellular concrete |
| 2 | w/c | --- | 0.4 | 0.45 | 0.5 | Water-cement ratio (by weight) |
| 3 | Fly ash | % | 15 | 25 | 35 | by weight of cementitious materials |
| 4 | Slag | % | 20 | 30 | 40 | by weight of cementitious materials |

**Table 3.18** Standard L9 orthogonal array.

| Exp.no | Independent variables | | | | Specimens ID |
|---|---|---|---|---|---|
| | Var. 1 | Var. 2 | Var. 3 | Var. 4 | |
| 1 | Level 1 | Level 1 | Level 1 | Level 1 | CC-1 |
| 2 | Level 1 | Level 2 | Level 2 | Level 2 | CC-2 |
| 3 | Level 1 | Level 3 | Level 3 | Level 3 | CC-3 |
| 4 | Level 2 | Level 1 | Level 2 | Level 3 | CC-4 |
| 5 | Level 2 | Level 2 | Level 3 | Level 1 | CC-5 |
| 6 | Level 2 | Level 3 | Level 1 | Level 2 | CC-6 |
| 7 | Level 3 | Level 1 | Level 3 | Level 2 | CC-7 |
| 8 | Level 3 | Level 2 | Level 1 | Level 3 | CC-8 |
| 9 | Level 3 | Level 3 | Level 2 | Level 1 | CC-9 |

Based on the L9 (34) orthogonal array mentioned above, the mix proportion was designed as follows. Table 3.19 shows the mix proportion of the cellular concrete with parameters and each level adopted from Table 3.17 and Table 3.18.

**Table 3.19** Mix proportion with parameter and each level.

| Code | Foam (%, volume) | w/c (ratio) | Fly ash (%, weight) | Slag (%, weight) |
|---|---|---|---|---|
| CC-1 | 30 | 0.40 | 15 | 20 |
| CC-2 | 30 | 0.45 | 25 | 30 |
| CC-3 | 30 | 0.50 | 35 | 40 |
| CC-4 | 35 | 0.40 | 25 | 40 |
| CC-5 | 35 | 0.45 | 35 | 20 |
| CC-6 | 35 | 0.50 | 15 | 30 |
| CC-7 | 40 | 0.40 | 35 | 30 |
| CC-8 | 40 | 0.45 | 15 | 40 |
| CC-9 | 40 | 0.50 | 25 | 20 |

Table 3.20 presents the mix proportions of binders. The mixes were prepared at about 5.5 min with a drill and a paddle. The cement was first mixed with 1/2 of water followed by pre-mixing the rest of water and cementitious materials (fly ash, and slag) . After the appropriate volume of the foam was generated, it was immediately added to the base mix and mixed all together until there was no foam on the surface of the paste. All the foam was uniformly distributed and incorporated into the mix.

**Table 3.20** Mix design of cellular concrete.

| Code | Foam (liter/$m^3$) | Net water (kg/$m^3$) | Cement (kg/$m^3$) | Fly ash (kg/$m^3$) | Slag (kg/$m^3$) |
|---|---|---|---|---|---|
| CC-1 | 300 | 373.40 | 626.02 | 144.47 | 192.62 |
| CC-2 | 300 | 391.19 | 403.04 | 223.91 | 268.69 |
| CC-3 | 300 | 406.69 | 209.27 | 292.98 | 334.83 |
| CC-4 | 350 | 339.52 | 309.18 | 220.84 | 353.35 |
| CC-5 | 350 | 362.11 | 375.93 | 292.39 | 167.08 |
| CC-6 | 350 | 377.39 | 430.33 | 117.36 | 234.73 |
| CC-7 | 400 | 312.12 | 286.93 | 286.93 | 245.94 |
| CC-8 | 400 | 328.26 | 344.06 | 114.69 | 305.83 |
| CC-9 | 400 | 346.97 | 399.05 | 181.39 | 145.11 |

### *3.3.3 Physical Properties Tests*

#### *Flow Table Test*

As was described in the initial screening test, the workability test was done using the consistency definitions described in ASTM C1107. Based on the flowability measurement by ASTM C1437, the flow of the grout was measured on the standard flow table after three drops in 2s. This measurement was taken 7 and 15 min after mixing (Figure 3.6).

#### *Setting Time Test*

When working with cellular concrete in any form, time record is required for all processes like transporting, placing, compacting, and finishing. During this process, cellular concrete pastes must be in the plastic stage so that every process can be done easily. The setting time of the mixtures was measured according to ASTM C191. A paste that is proportioned and mixed to normal consistency is molded and placed in a moist cabinet and allowed to start setting (Figure 3.22).

Periodic penetration tests are performed on this paste by allowing a 1-mm Vicat needle to settle into this paste. The Vicat initial time of setting is the time elapsed between the initial contact of cement and water and the time when the penetration is measured or the time when calculation is 25 mm. The Vicat final time of setting is the time elapsed between initial contact of cement and water and the time when the needle does not leave a complete circular impression in the paste surface (ASTM C191).

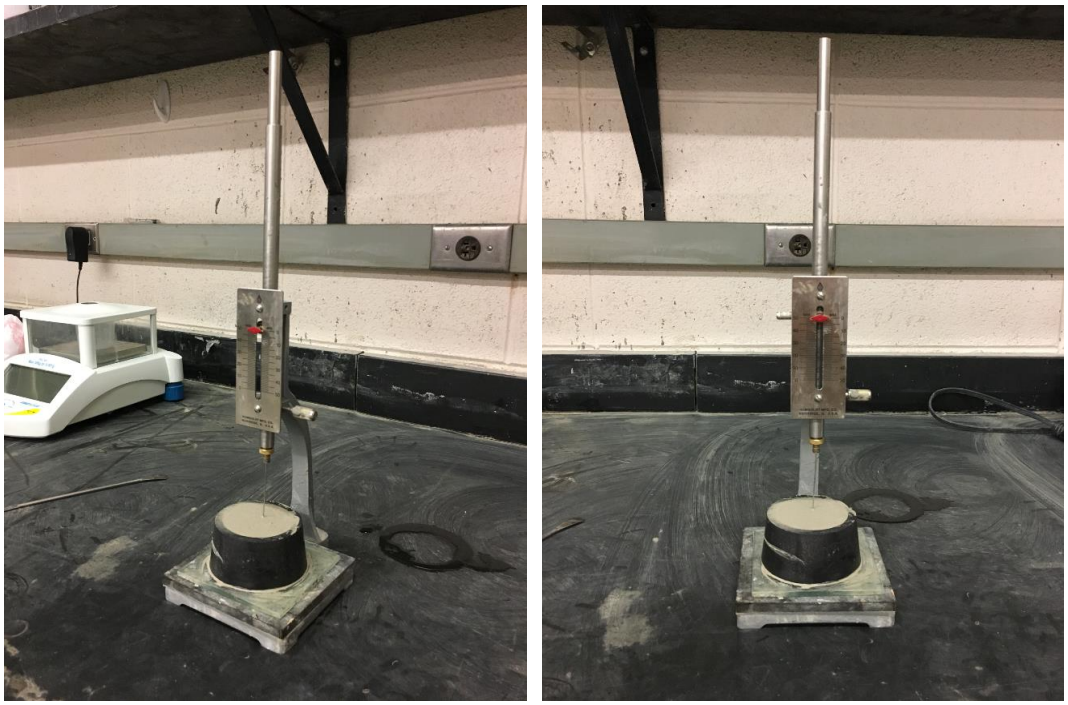

**Figure 3.22** Setting time test by Vicat apparatus (ASTM C191).

***Density Measurement***

After the first 24h, the specimens were demolded and an electronic scale was used to measure the fresh density of the cellular concrete. After 21 days, the specimens were moved into an oven at 110±5℃ and weighed at 24-h intervals until the loss in weight does not exceed 1%

in a 24-h period. To minimize the accidental error, a set of 10 specimens was measured at a time to calculate the fresh density of specimens. So the fresh density and oven-dry density can be obtained in this way.

***Compressive Strength Test***

The goal of a compressive strength test is to determine the behavior of cellular concrete specimen while it experiences a compressive load by measuring stress. For the evaluation of compressive strength, 2in×2in cube specimens as was described in ASTM C109 were prepared according to ASTM C1107. The 200 Kip Tinius-Olsen Universal Testing Machine was applied to test the compressive strength of the cubic specimens at several ages: 3, 7, 14, 21, and 28 days (Figure 3.10).

***Thermal Properties Test***

In this study, the Transient Plane Source (TPS) method is utilized for studying the thermal transport properties. The TPS method is based on the use of a transiently heated plane sensor (Kapton insulated sensor 5501) and in its most common adaptation referred to as the Hot Disk Thermal Constants Analyzer (Figure 3.12). While performing a measurement, the Kapton sensor is fitted between two pieces of cellular concrete specimens and each one with a plane surface face to the sensor. The solution of the thermal conductivity equation is based on the assumption that the Hot Disk sensor is located in an infinite medium, which means that the transient recording must be interrupted as soon as possible to avoid the outside influence.

### *3.3.4 Results and Analysis*

#### *Workability*

Table 3.21 shows the results of the flow table test of various mixes of cellular concrete. The main effect plotted by each factor for the flow table test of cellular concrete is demonstrated in Figure 3.23 and Figure 3.24. The degree of contributing factors was calculated using analysis of variance (ANOVA) in Minitab. Table 3.21 presents the overall view of the effects of constituent of cellular concrete on flowability. It is observed that the workability was strongly influenced by the water cementitious ratio.

**Table 3.21** Results of flow table test (ASTM C1437).

| Specimen ID | Number of Drops | Flow at 7 min, Percent | Flow at 15 min, Percent |
|---|---|---|---|
| CC1 | 3 | 73 | 60 |
| CC2 | 3 | 88 | 75 |
| CC3 | 3 | 100 | 85 |
| CC4 | 3 | 63 | 50 |
| CC5 | 3 | 75 | 70 |
| CC6 | 3 | 105 | 95 |
| CC7 | 3 | 75 | 70 |
| CC8 | 3 | 88 | 75 |
| CC9 | 3 | 100 | 93 |

Figure 3.23 and Figure 3.24 displays the influence of foam volume, water-cementitious ratio, fly ash, and slag on the flowability of cellular concrete. It is observed that water-cementitious ratio have an essential influence on the flowability of cellular concrete, by increasing the water-cementitious ratio, and the flowability of cellular concrete pastes increased very fast.

The flow measurement decreased with the increase of fly ash percentage due to the high specific surface area of fly ash, thus increasing the water demand. This was mainly because of the absorptive character of fly ash particles. Cellular concrete containing fly ash requires more water for a given consistency. However, for cellular concrete with high water-cementitious ratio, the addition of fly ash could improve the stability of the cellular concrete.

All foam volume, as shown in Figure 3.23 and Figure 3.24, fulfilled the workability requirement. The above level of 35% indicated the ascent of the workability for the mechanism of the adhesion between the bubbles and solid particles in the mixture. However, at the level below 35%, by increasing the foam content, the workability will decrease.

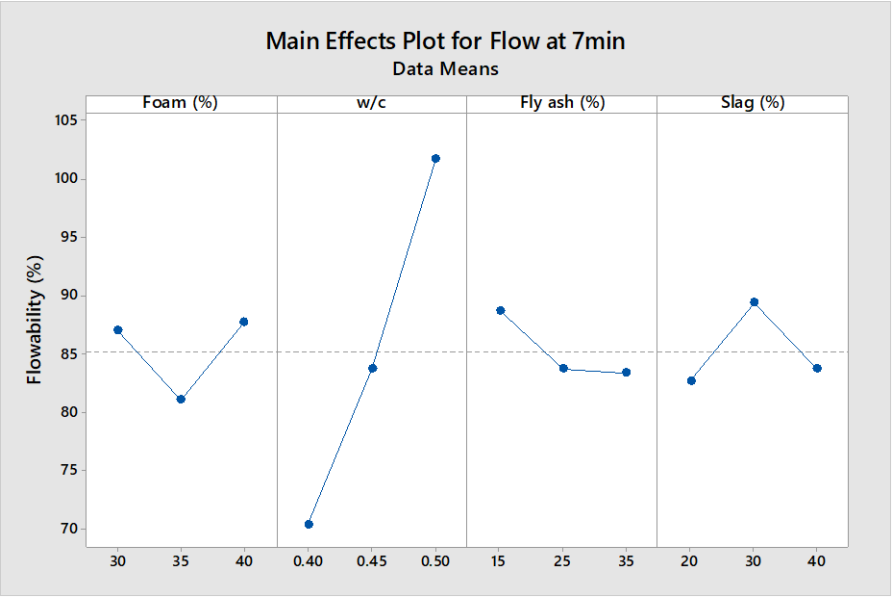


**Figure 3.23** Main effects plot for flow table test (flow at 7 min).

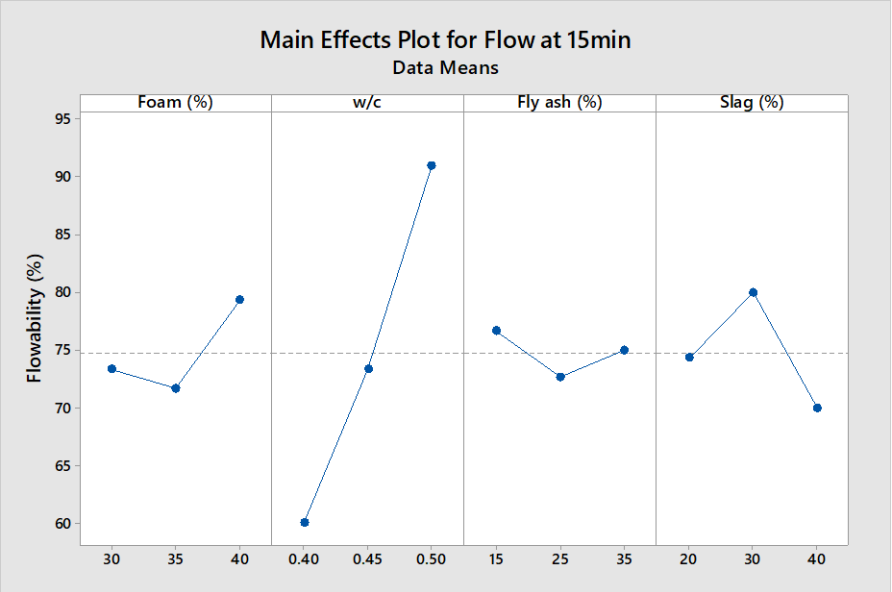


**Figure 3.24** Main effects plot for flow table test (flow at 15 min).

***Setting Time***

Initial setting time defined as the time elapsed between the moment that the water is added to the cement, to the time that the paste starts losing its plasticity. The final setting time defined as the time elapsed between the water added moment and the time when paste has completely lost its plasticity. In the meantime, the paste has attained sufficient firmness to resist certain definite pressure.

Normally a minimum of 30 min has maintained for mixing and handing operations. The initial setting time should not be less than 30 minutes. The target final setting time should not exceed 24 hours. As can be observed from Table 3.22, all the results of initial setting time test meet the minimum requirement and most of the final setting time meet the maximum requirement, except specimen CC9.

**Table 3.22** Results of setting time test.

| Specimen ID | Initial setting (min) | Final setting (min) |
|---|---|---|
| CC1 | 315 | 690 |
| CC2 | 330 | 660 |
| CC3 | 495 | 720 |
| CC4 | 300 | 675 |
| CC5 | 345 | 735 |
| CC6 | 525 | 825 |
| CC7 | 345 | 615 |
| CC8 | 360 | 690 |
| CC9 | 540 | 945 |

***Density***

In this test, the fresh density and oven-dry density are shown in Table 3.23 and Table 3.24, respectively. The fresh density ranges from 1031 kg/m$^3$ (64.3 lbs/ft$^3$) to 1428 kg/m$^3$ (89.2 lbs/ft$^3$). Moreover, the oven-dry density ranges from 975 kg/m$^3$ (60.9 lbs/ft$^3$) to 1308 kg/m$^3$ (81.7 lbs/ft$^3$).

**Table 3.23** Fresh density of the specimens.

| Specimen ID | Specimen Number | Mass (kg) | Volume (m$^3$) | Density (kg/m$^3$) | Density (lbs/ft$^3$) |
|---|---|---|---|---|---|
| CC1 | 10 | 1.8724 | $1.31 \times 10^{-3}$ | 1428 | 89.2 |
| CC2 | 10 | 1.7074 | $1.31 \times 10^{-3}$ | 1302 | 81.3 |
| CC3 | 10 | 1.6314 | $1.31 \times 10^{-3}$ | 1244 | 77.7 |
| CC4 | 10 | 1.6822 | $1.31 \times 10^{-3}$ | 1283 | 80.1 |
| CC5 | 10 | 1.6256 | $1.31 \times 10^{-3}$ | 1240 | 77.4 |
| CC6 | 10 | 1.5232 | $1.31 \times 10^{-3}$ | 1162 | 72.5 |
| CC7 | 10 | 1.4720 | $1.31 \times 10^{-3}$ | 1123 | 70.1 |
| CC8 | 10 | 1.5036 | $1.31 \times 10^{-3}$ | 1147 | 71.6 |
| CC9 | 10 | 1.3512 | $1.31 \times 10^{-3}$ | 1031 | 64.3 |

**Table 3.24** Oven-dry density of the specimens.

| Specimen ID | Specimen Number | Mass (kg) | Volume ($m^3$) | Density ($kg/m^3$) | Density ($lbs/ft^3$) |
|---|---|---|---|---|---|
| CC1 | 10 | 1.7147 | $1.31 \times 10^{-3}$ | 1308 | 81.7 |
| CC2 | 10 | 1.5298 | $1.31 \times 10^{-3}$ | 1167 | 72.8 |
| CC3 | 10 | 1.4525 | $1.31 \times 10^{-3}$ | 1108 | 69.2 |
| CC4 | 10 | 1.5364 | $1.31 \times 10^{-3}$ | 1172 | 73.2 |
| CC5 | 10 | 1.4958 | $1.31 \times 10^{-3}$ | 1141 | 71.2 |
| CC6 | 10 | 1.4079 | $1.31 \times 10^{-3}$ | 1074 | 67.0 |
| CC7 | 10 | 1.3935 | $1.31 \times 10^{-3}$ | 1063 | 66.4 |
| CC8 | 10 | 1.4119 | $1.31 \times 10^{-3}$ | 1077 | 67.2 |
| CC9 | 10 | 1.2782 | $1.31 \times 10^{-3}$ | 975 | 60.9 |

***Compressive Strength***

In order to get a better understanding of the influence of 4 different independent variables (foam volume, water-cementitious ratio, fly ash, and slag) on the compressive strength of cellular concrete, the standard L9 Taguchi design was chosen for an experiment. Table 3.25-3.29 depicts the compressive strength of cellular concrete at the age of 3, 7, 14, 21, and 28 days, respectively. 2in×2in cube specimens, as was described in ASTM C109, were prepared for the evaluation of compressive strength of the cellular concrete with different foam content. The results show that in 3, 7, 14, 21, and 28 days the compressive strength could be obtained in the range of 1.8-11.8, 2.4-15.0, 3.3-17.0, 4.2-18.7, and 5.4-21.2 MPa, respectively. Meanwhile, the highest and lowest compressive strength were obtained from CC1 and CC7, respectively.

**Table 3.25** 3-days compressive strength test results.

| Specimen ID | Age | No. | Compressive Strength | | Average Compressive Strength | |
|---|---|---|---|---|---|---|
| | (day) | | (psi) | (MPa) | (psi) | (MPa) |
| CC1 | 3 | 1 | 1620 | 11.2 | 1705 | 11.8 |
| | | 2 | 1649 | 11.4 | | |
| | | 3 | 1846 | 12.7 | | |
| CC2 | 3 | 1 | 1482 | 10.2 | 1413 | 9.7 |
| | | 2 | 1355 | 9.3 | | |
| | | 3 | 1403 | 9.7 | | |
| CC3 | 3 | 1 | 735 | 5.1 | 766 | 5.3 |
| | | 2 | 783 | 5.4 | | |
| | | 3 | 781 | 5.4 | | |
| CC4 | 3 | 1 | 1060 | 7.3 | 1047 | 7.2 |
| | | 2 | 1063 | 7.3 | | |
| | | 3 | 1017 | 7.0 | | |
| CC5 | 3 | 1 | 910 | 6.3 | 1019 | 7.0 |
| | | 2 | 1134 | 7.8 | | |
| | | 3 | 1014 | 7.0 | | |
| CC6 | 3 | 1 | 795 | 5.5 | 835 | 5.8 |
| | | 2 | 843 | 5.8 | | |
| | | 3 | 867 | 6.0 | | |
| CC7 | 3 | 1 | 341 | 2.4 | 255 | 1.8 |
| | | 2 | 195 | 1.3 | | |
| | | 3 | 228 | 1.6 | | |
| CC8 | 3 | 1 | 719 | 5.0 | 740 | 5.1 |
| | | 2 | 741 | 5.1 | | |
| | | 3 | 761 | 5.2 | | |
| CC9 | 3 | 1 | 830 | 5.7 | 836 | 5.8 |
| | | 2 | 844 | 5.8 | | |
| | | 3 | 833 | 5.7 | | |

**Table 3.26** 7-days compressive strength test results.

| Specimen ID | Age | No. | Compressive Strength | | Average Compressive Strength | |
|---|---|---|---|---|---|---|
| | (day) | | (psi) | (MPa) | (psi) | (MPa) |
| CC1 | 7 | 1 | 2053 | 14.2 | 2179 | 15.0 |
| | | 2 | 2215 | 15.3 | | |
| | | 3 | 2269 | 15.6 | | |
| CC2 | 7 | 1 | 1722 | 11.9 | 1628 | 11.2 |
| | | 2 | 1590 | 11.0 | | |
| | | 3 | 1572 | 10.8 | | |
| CC3 | 7 | 1 | 1096 | 7.6 | 1051 | 7.2 |
| | | 2 | 1124 | 7.7 | | |
| | | 3 | 934 | 6.4 | | |
| CC4 | 7 | 1 | 1286 | 8.9 | 1271 | 8.8 |
| | | 2 | 1296 | 8.9 | | |
| | | 3 | 1231 | 8.5 | | |
| CC5 | 7 | 1 | 1326 | 9.1 | 1270 | 8.8 |
| | | 2 | 1248 | 8.6 | | |
| | | 3 | 1237 | 8.5 | | |
| CC6 | 7 | 1 | 1470 | 10.1 | 1468 | 10.1 |
| | | 2 | 1527 | 10.5 | | |
| | | 3 | 1407 | 9.7 | | |
| CC7 | 7 | 1 | 387 | 2.7 | 347 | 2.4 |
| | | 2 | 299 | 2.1 | | |
| | | 3 | 354 | 2.4 | | |
| CC8 | 7 | 1 | 1086 | 7.5 | 1069 | 7.4 |
| | | 2 | 983 | 6.8 | | |
| | | 3 | 1138 | 7.8 | | |
| CC9 | 7 | 1 | 1138 | 7.8 | 1117 | 7.7 |
| | | 2 | 1073 | 7.4 | | |
| | | 3 | 1140 | 7.9 | | |

**Table 3.27** 14-days compressive strength test results.

| Specimen ID | Age | No. | Compressive Strength | | Average Compressive Strength | |
|---|---|---|---|---|---|---|
| | (day) | | (psi) | (MPa) | (psi) | (MPa) |
| CC1 | 14 | 1 | 2375 | 16.4 | 2462 | 17.0 |
| | | 2 | 2497 | 17.2 | | |
| | | 3 | 2514 | 17.3 | | |
| CC2 | 14 | 1 | 2200 | 15.2 | 2132 | 14.7 |
| | | 2 | 2058 | 14.2 | | |
| | | 3 | 2137 | 14.7 | | |
| CC3 | 14 | 1 | 1302 | 9.0 | 1330 | 9.2 |
| | | 2 | 1376 | 9.5 | | |
| | | 3 | 1311 | 9.0 | | |
| CC4 | 14 | 1 | 2078 | 14.3 | 2063 | 14.2 |
| | | 2 | 2057 | 14.2 | | |
| | | 3 | 2055 | 14.2 | | |
| CC5 | 14 | 1 | 1414 | 9.7 | 1438 | 9.9 |
| | | 2 | 1509 | 10.4 | | |
| | | 3 | 1390 | 9.6 | | |
| CC6 | 14 | 1 | 1481 | 10.2 | 1488 | 10.3 |
| | | 2 | 1499 | 10.3 | | |
| | | 3 | 1484 | 10.2 | | |
| CC7 | 14 | 1 | 509 | 3.5 | 480 | 3.3 |
| | | 2 | 460 | 3.2 | | |
| | | 3 | 470 | 3.2 | | |
| CC8 | 14 | 1 | 1222 | 8.4 | 1231 | 8.5 |
| | | 2 | 1227 | 8.5 | | |
| | | 3 | 1243 | 8.6 | | |
| CC9 | 14 | 1 | 1155 | 8.0 | 1221 | 8.4 |
| | | 2 | 1257 | 8.7 | | |
| | | 3 | 1252 | 8.6 | | |

**Table 3.28** 21-days compressive strength test results.

| Specimen ID | Age | No. | Compressive Strength | | Average Compressive Strength | |
|---|---|---|---|---|---|---|
| | (day) | | (psi) | (MPa) | (psi) | (MPa) |
| CC1 | 21 | 1 | 2709 | 18.7 | 2712 | 18.7 |
| | | 2 | 2730 | 18.8 | | |
| | | 3 | 2696 | 18.6 | | |
| CC2 | 21 | 1 | 2514 | 17.3 | 2391 | 16.5 |
| | | 2 | 2230 | 15.4 | | |
| | | 3 | 2428 | 16.7 | | |
| CC3 | 21 | 1 | 1406 | 9.7 | 1432 | 9.9 |
| | | 2 | 1438 | 9.9 | | |
| | | 3 | 1453 | 10.0 | | |
| CC4 | 21 | 1 | 1864 | 12.9 | 1955 | 13.5 |
| | | 2 | 2034 | 14.0 | | |
| | | 3 | 1967 | 13.6 | | |
| CC5 | 21 | 1 | 1896 | 13.1 | 1817 | 12.5 |
| | | 2 | 1721 | 11.9 | | |
| | | 3 | 1833 | 12.6 | | |
| CC6 | 21 | 1 | 1698 | 11.7 | 1645 | 11.3 |
| | | 2 | 1533 | 10.6 | | |
| | | 3 | 1704 | 11.7 | | |
| CC7 | 21 | 1 | 524 | 3.6 | 608 | 4.2 |
| | | 2 | 669 | 4.6 | | |
| | | 3 | 632 | 4.4 | | |
| CC8 | 21 | 1 | 1353 | 9.3 | 1420 | 9.8 |
| | | 2 | 1582 | 10.9 | | |
| | | 3 | 1324 | 9.1 | | |
| CC9 | 21 | 1 | 1449 | 10.0 | 1351 | 9.3 |
| | | 2 | 1320 | 9.1 | | |
| | | 3 | 1285 | 8.9 | | |

**Table 3.29** 28-days compressive strength test results.

| Specimen ID | Age | No. | Compressive Strength | | Average Compressive Strength | |
|---|---|---|---|---|---|---|
| | (day) | | (psi) | (MPa) | (psi) | (MPa) |
| CC1 | 28 | 1 | 3151 | 21.7 | 3071 | 21.2 |
| | | 2 | 2833 | 19.5 | | |
| | | 3 | 3228 | 22.3 | | |
| CC2 | 28 | 1 | 2674 | 18.4 | 2598 | 17.9 |
| | | 2 | 2562 | 17.7 | | |
| | | 3 | 2557 | 17.6 | | |
| CC3 | 28 | 1 | 1792 | 12.4 | 1965 | 13.5 |
| | | 2 | 2109 | 14.5 | | |
| | | 3 | 1993 | 13.7 | | |
| CC4 | 28 | 1 | 2126 | 14.7 | 2143 | 14.8 |
| | | 2 | 2234 | 15.4 | | |
| | | 3 | 2069 | 14.3 | | |
| CC5 | 28 | 1 | 2044 | 14.1 | 2205 | 15.2 |
| | | 2 | 2339 | 16.1 | | |
| | | 3 | 2231 | 15.4 | | |
| CC6 | 28 | 1 | 1898 | 13.1 | 1847 | 12.7 |
| | | 2 | 1875 | 12.9 | | |
| | | 3 | 1768 | 12.2 | | |
| CC7 | 28 | 1 | 820 | 5.7 | 789 | 5.4 |
| | | 2 | 814 | 5.6 | | |
| | | 3 | 732 | 5.0 | | |
| CC8 | 28 | 1 | 1740 | 12.0 | 1713 | 11.8 |
| | | 2 | 1678 | 11.6 | | |
| | | 3 | 1720 | 11.9 | | |
| CC9 | 28 | 1 | 1570 | 10.8 | 1594 | 11.0 |
| | | 2 | 1590 | 11.0 | | |
| | | 3 | 1623 | 11.2 | | |

Figure 3.25 shows the histogram of the compressive strength of 9 sets of cellular concrete specimens. As can be seen, CC1 obtained the highest compressive strength, and CC7 obtained the lowest compressive strength. The compressive strength of cellular concrete with different foam content in the mixes displayed a continuous increase with age.

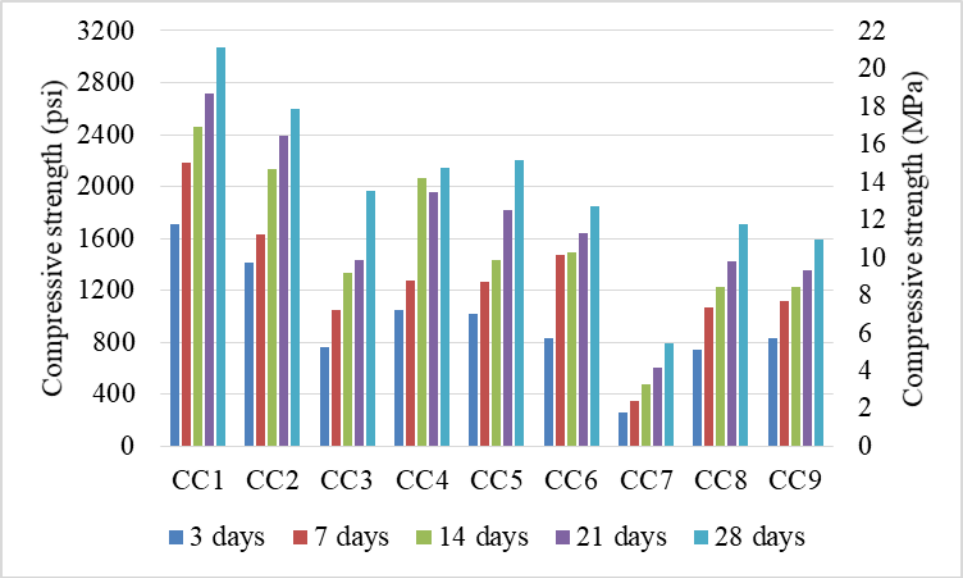


**Figure 3.25** Compressive strength of specimens at 3, 7, 14, 21, 28 days.

The lab test result was analyzed by a statistical software named MINITAB. The MINITAB software can calculate regression coefficients table and variance results table for cellular concrete. In statistics, standardized regression coefficients are also called beta coefficients or beta weights. A regression coefficient describes the size and direction of the relationship between a predictor and the response variable. Coefficients are the numbers by which the values of the term are multiplied in a regression equation. Figure 3.26 presents the summary of main effects plot from 3 to 28 days compressive strength of cellular concrete.

The foam content has a significant influence on the compressive strength of cellular concrete. The bubbles in the cellular concrete significantly contributed to the compressive behavior of cellular concrete. What is more, the volume of foam affected the interconnectivity of bubbles, and the bubble merger in places resulted in large voids. This weakness reduced the compressive strength of cellular concrete specimens. As was observed in Figure 3.26, by

increasing the foam volume from 30% to 40%, the compressive strength of cellular concrete decreases significantly.

The adequate amount of water and high pozzolanic reactivity are the main factors of the acceleration of reaction in the hydration process of concrete. When studying the effect of water-cementitious ratio (w/c) on compressive strength, the maximum compressive strength was found at the w/c of 0.45. The reason is that 0.45 of w/c can provide the optimum amount of water required to facilitate the hydration process using pozzolanic materials with $Ca(OH)_2$ produced by Portland cement. However, when w/c exceeds 0.45, the excess water formed the capillary pores structures in the cellular concrete result in a descent in compressive strength. When w/c is lower than 0.45, the insufficient hydration reaction would also lead to a decrease in compressive strength.

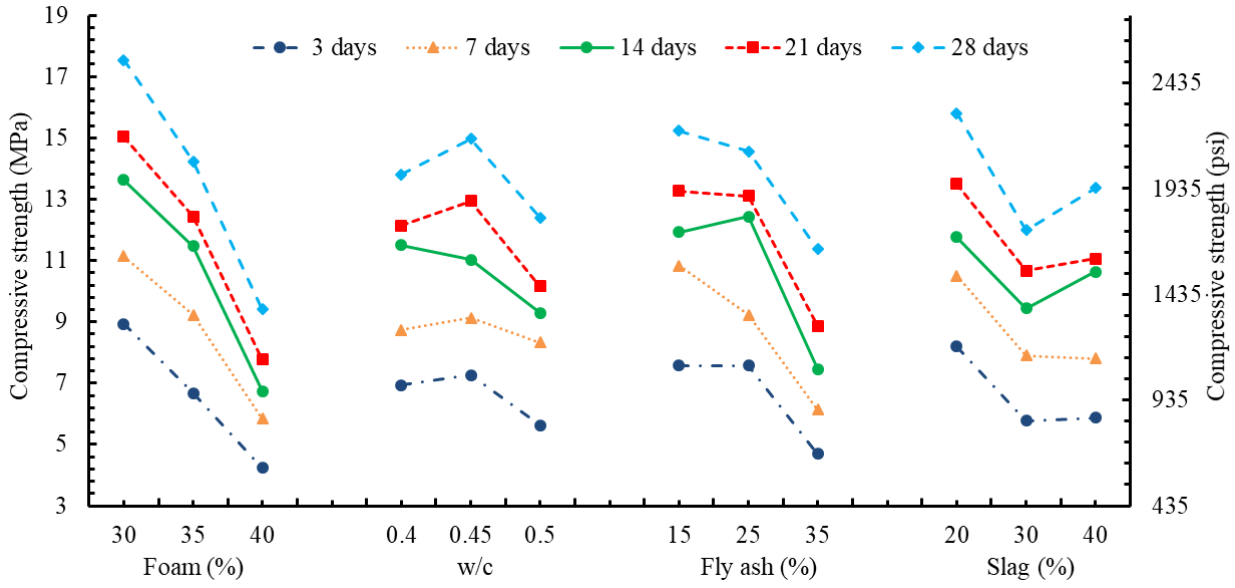


**Figure 3.26** Summary of main effects plot for compressive strength.

As demonstrated in Figure 3.26, fly ash also has an extraordinary influence on the compressive strength of cellular concrete. As the amount of fly ash increased, the compressive strength of concrete decreased rapidly. When studying the effect of slag on compressive strength, the minimum compressive strength was reached at 30% slag. However, when the proportion of slag exceeds 30%, the compressive strength of cellular concrete will increase with an ascent of slag content. When the proportion of slag is lower than 30%, with the increase of the slag content, the compressive strength of cellular concrete will decrease.

***Thermal Properties***

Cellular concrete has excellent thermal insulating properties as a result of its cellular microstructure. Based on the Taguchi methods, the standard L9 Taguchi design was chosen for an experiment to explore the thermal properties of cellular concrete. Briefly, when performing a thermal transport measurement, the TPS sensor is placed between two pieces of cellular concrete to be measured and repeat the measurement to ensure there is no temperature drift present. Each specimen was tested five times and then averaged to get the value. The detail of the thermal properties of cellular concrete is presented in Tables 3.30 to 3.38.

**Table 3.30** Thermal properties of cellular concrete (Specimen: CC1).

| Specimen ID | Number | Temperature (℃) | Thermal Conductivity (W/m·℃) | Thermal Diffusivity ($mm^2/s$) | Specific Heat Capacity ($MJ/m^3·℃$) |
|---|---|---|---|---|---|
| CC1 | 1 | 21.0 | 0.5584 | 0.3492 | 1.599 |
| | 2 | 21.0 | 0.5431 | 0.3355 | 1.619 |
| | 3 | 21.0 | 0.5418 | 0.3339 | 1.623 |
| | 4 | 21.0 | 0.5431 | 0.3291 | 1.650 |
| | 5 | 21.0 | 0.5410 | 0.3249 | 1.665 |
| | Average | 21.0 | 0.5455 | 0.3345 | 1.631 |
| | St.dev | 0.0 | 0.0065 | 0.0082 | 0.024 |

**Table 3.31** Thermal properties of cellular concrete (Specimen: CC2).

| Specimen ID | Number | Temperature (℃) | Thermal Conductivity (W/m·℃) | Thermal Diffusivity ($mm^2/s$) | Specific Heat Capacity ($MJ/m^3·℃$) |
|---|---|---|---|---|---|
| CC2 | 1 | 21.0 | 0.5140 | 0.3312 | 1.552 |
| | 2 | 21.0 | 0.5013 | 0.3169 | 1.582 |
| | 3 | 21.0 | 0.5013 | 0.3179 | 1.577 |
| | 4 | 21.0 | 0.5014 | 0.3207 | 1.563 |
| | 5 | 21.0 | 0.5011 | 0.3179 | 1.576 |
| | Average | 21.0 | 0.5038 | 0.3209 | 1.570 |
| | St.dev | 0.0 | 0.0051 | 0.0053 | 0.011 |

**Table 3.32** Thermal properties of cellular concrete (Specimen: CC3).

| Specimen ID | Number | Temperature (℃) | Thermal Conductivity (W/m·℃) | Thermal Diffusivity ($mm^2/s$) | Specific Heat Capacity ($MJ/m^3·℃$) |
|---|---|---|---|---|---|
| CC3 | 1 | 21.0 | 0.4142 | 0.3023 | 1.370 |
| | 2 | 21.0 | 0.4176 | 0.3119 | 1.339 |
| | 3 | 21.0 | 0.4195 | 0.3156 | 1.329 |
| | 4 | 21.0 | 0.4202 | 0.3155 | 1.332 |
| | 5 | 21.0 | 0.4184 | 0.3114 | 1.344 |
| | Average | 21.0 | 0.4180 | 0.3113 | 1.343 |
| | St.dev | 0.0 | 0.0021 | 0.0049 | 0.015 |

**Table 3.33** Thermal properties of cellular concrete (Specimen: CC4).

| Specimen ID | Number | Temperature (℃) | Thermal Conductivity (W/m·℃) | Thermal Diffusivity ($mm^2/s$) | Specific Heat Capacity ($MJ/m^3·℃$) |
|---|---|---|---|---|---|
| CC4 | 1 | 21.0 | 0.4507 | 0.3012 | 1.497 |
| | 2 | 21.0 | 0.4343 | 0.2832 | 1.533 |
| | 3 | 21.0 | 0.4334 | 0.2828 | 1.533 |
| | 4 | 21.0 | 0.4327 | 0.2802 | 1.544 |
| | 5 | 21.0 | 0.4334 | 0.2824 | 1.535 |
| | Average | 21.0 | 0.4369 | 0.2860 | 1.528 |
| | St.dev | 0.0 | 0.0069 | 0.0077 | 0.016 |

**Table 3.34** Thermal properties of cellular concrete (Specimen: CC5).

| Specimen ID | Number | Temperature (℃) | Thermal Conductivity (W/m·℃) | Thermal Diffusivity ($mm^2/s$) | Specific Heat Capacity ($MJ/m^3·℃$) |
|---|---|---|---|---|---|
| CC5 | 1 | 21.0 | 0.4557 | 0.3088 | 1.476 |
| | 2 | 21.0 | 0.4297 | 0.2754 | 1.560 |
| | 3 | 21.0 | 0.4291 | 0.2786 | 1.540 |
| | 4 | 21.0 | 0.4277 | 0.2745 | 1.558 |
| | 5 | 21.0 | 0.4278 | 0.2781 | 1.538 |
| | Average | 21.0 | 0.4340 | 0.2831 | 1.534 |
| | St.dev | 0.0 | 0.0109 | 0.0130 | 0.031 |

**Table 3.35** Thermal properties of cellular concrete (Specimen: CC6).

| Specimen ID | Number | Temperature (℃) | Thermal Conductivity (W/m·℃) | Thermal Diffusivity ($mm^2/s$) | Specific Heat Capacity ($MJ/m^3·℃$) |
|---|---|---|---|---|---|
| CC6 | 1 | 21.0 | 0.4369 | 0.3576 | 1.222 |
| | 2 | 21.0 | 0.4103 | 0.3140 | 1.307 |
| | 3 | 21.0 | 0.4101 | 0.3152 | 1.301 |
| | 4 | 21.0 | 0.4086 | 0.3139 | 1.302 |
| | 5 | 21.0 | 0.4089 | 0.3148 | 1.299 |
| | Average | 21.0 | 0.4149 | 0.3231 | 1.286 |
| | St.dev | 0.0 | 0.0110 | 0.0172 | 0.032 |

**Table 3.36** Thermal properties of cellular concrete (Specimen: CC7).

| Specimen ID | Number | Temperature (℃) | Thermal Conductivity (W/m·℃) | Thermal Diffusivity ($mm^2/s$) | Specific Heat Capacity ($MJ/m^3·℃$) |
|---|---|---|---|---|---|
| CC7 | 1 | 21.0 | 0.4003 | 0.6430 | 0.6225 |
| | 2 | 21.0 | 0.3922 | 0.6074 | 0.6457 |
| | 3 | 21.0 | 0.3913 | 0.6062 | 0.6456 |
| | 4 | 21.0 | 0.3916 | 0.6195 | 0.6322 |
| | 5 | 21.0 | 0.3917 | 0.6107 | 0.6414 |
| | Average | 21.0 | 0.3934 | 0.6174 | 0.6375 |
| | St.dev | 0.0 | 0.0034 | 0.0136 | 0.0089 |

**Table 3.37** Thermal properties of cellular concrete (Specimen: CC8).

| Specimen ID | Number | Temperature (℃) | Thermal Conductivity (W/m·℃) | Thermal Diffusivity ($mm^2/s$) | Specific Heat Capacity ($MJ/m^3·℃$) |
|---|---|---|---|---|---|
| CC8 | 1 | 21.0 | 0.3737 | 0.3808 | 0.9812 |
| | 2 | 21.0 | 0.3611 | 0.3619 | 0.9980 |
| | 3 | 21.0 | 0.3612 | 0.3594 | 1.0050 |
| | 4 | 21.0 | 0.3619 | 0.3625 | 0.9982 |
| | 5 | 21.0 | 0.3596 | 0.3531 | 1.0180 |
| | Average | 21.0 | 0.3635 | 0.3635 | 1.0001 |
| | St.dev | 0.0 | 0.0051 | 0.0093 | 0.0120 |

**Table 3.38** Thermal properties of cellular concrete (Specimen: CC9).

| Specimen ID | Number | Temperature (℃) | Thermal Conductivity (W/m·℃) | Thermal Diffusivity ($mm^2/s$) | Specific Heat Capacity ($MJ/m^3·℃$) |
|---|---|---|---|---|---|
| CC9 | 1 | 21.0 | 0.3432 | 0.3049 | 1.126 |
| | 2 | 21.0 | 0.3463 | 0.3134 | 1.105 |
| | 3 | 21.0 | 0.3463 | 0.3116 | 1.112 |
| | 4 | 21.0 | 0.3467 | 0.3120 | 1.111 |
| | 5 | 21.0 | 0.3474 | 0.3159 | 1.100 |
| | Average | 21.0 | 0.3460 | 0.3116 | 1.111 |
| | St.dev | 0.0 | 0.0014 | 0.0037 | 0.009 |

As was observed in Figure 3.27, the foam volume has the most significant influence on the thermal conductivity of cellular concrete. The bubbles in the cellular concrete significantly contributed to the thermal insulation behavior of the cellular concrete. By increasing the foam volume from 30% to 40%, the thermal conductivity of cellular concrete decreased very fast. Similarly, increasing the w/c, the proportion of fly ash or the proportion of slag has a positive influence on the thermal insulation property of cellular concrete.

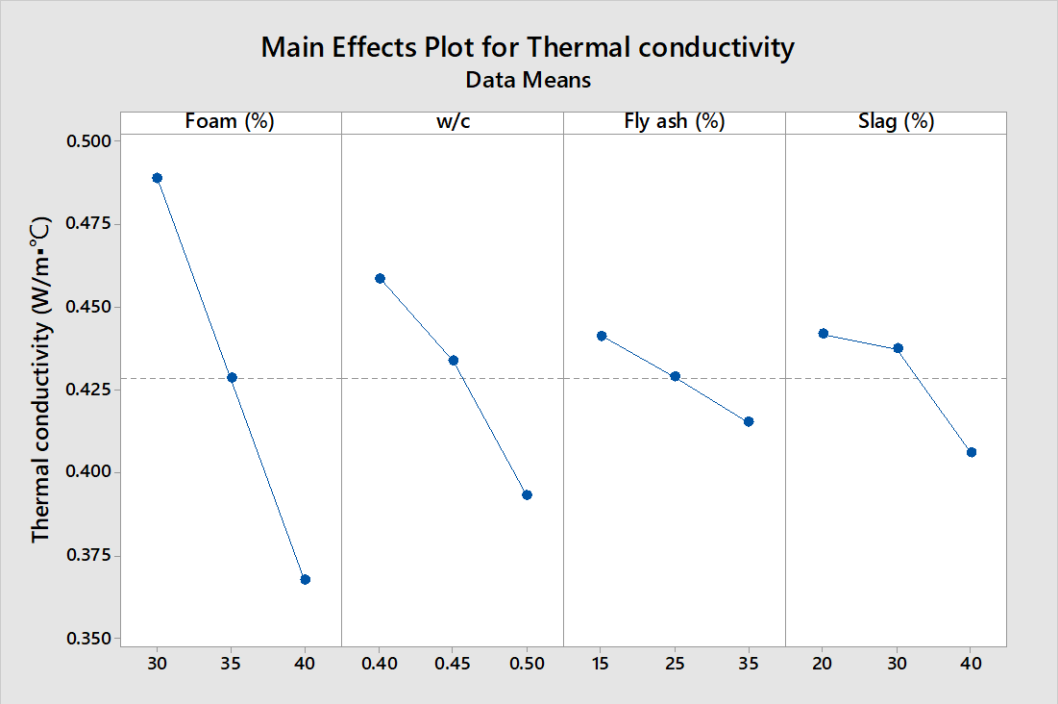


**Figure 3.27** Main effects plot for thermal conductivity.

Figure 3.28 presents the main effects of the independent variables (foam volume, water-cementitious ratio, fly ash, and slag) on the thermal diffusivity. When studying the effect of foam content on thermal diffusivity, the minimum thermal diffusivity was reached at 35% slag. However, when the proportion of foam is lower than 35%, by increasing the foam content, the

thermal diffusivity of cellular concrete will decrease. When the proportion of foam exceeds 35%, the thermal diffusivity of cellular concrete will significantly increase with an increase of foam content. Also, the proportion of fly ash has a similar effect on the thermal diffusivity of cellular concrete. The proportion of slag has the opposite influence on the thermal diffusivity of cellular concrete. The water-cementitious ratio has a negative influence on the thermal diffusivity of cellular concrete. By increasing the w/c, the thermal diffusivity will drop very fast.

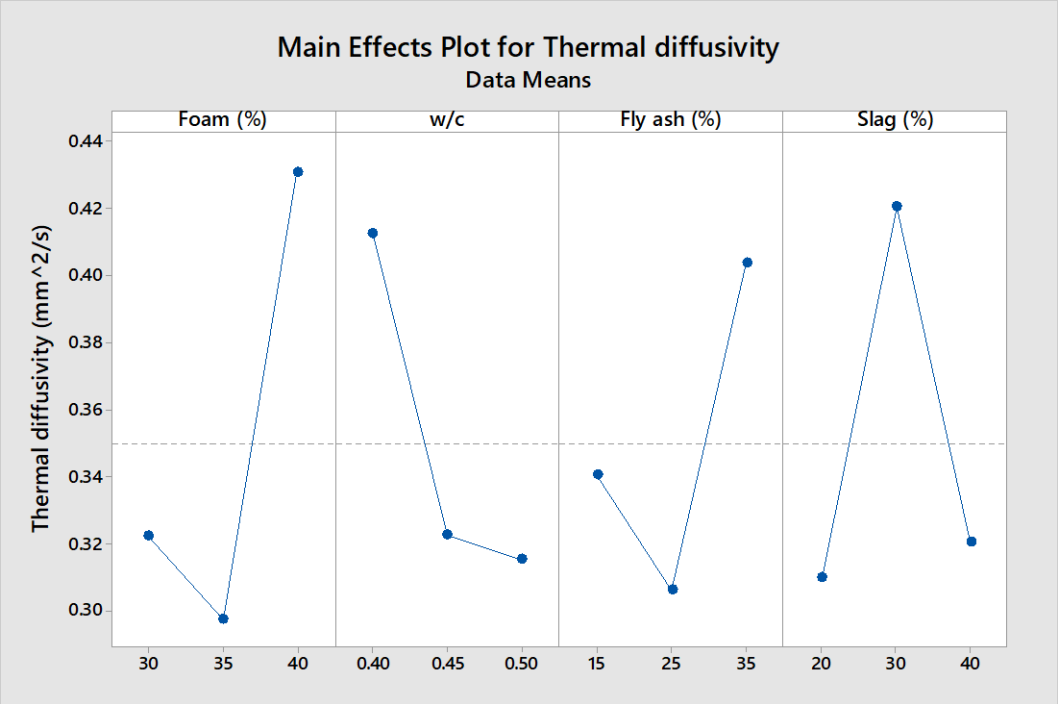


**Figure 3.28** Main effects plot for thermal diffusivity.

With the accompaying Figure 3.29, the foam volume has a remarkable influence on the specific heat capacity of cellular concrete. By increasing the foam volume from 30% to 40%, the specific heat capacity of cellular concrete decrease very fast.

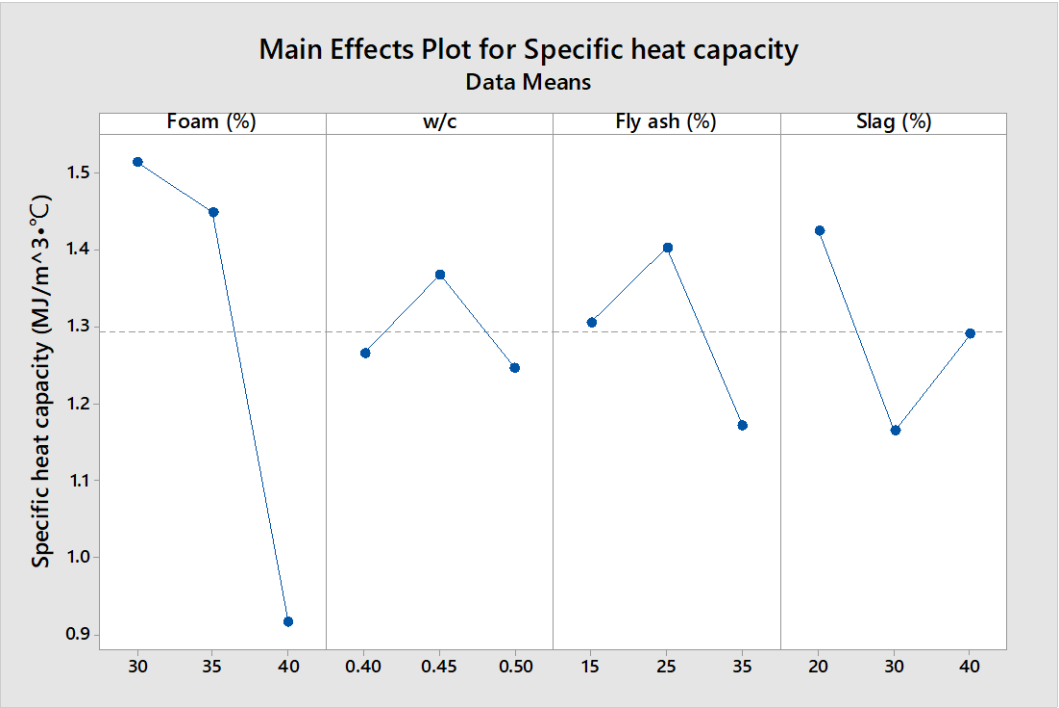


**Figure 3.29** Main effects plot for specific heat capacity.

When studying the effect of water-cementitious ratio on the specific heat capacity of cellular concrete, the maximum specific heat capacity was reached at w/c of 0.45. However, when the w/c is lower than 0.45, by increasing w/c, the specific heat capacity of cellular concrete will increase. When the w/c exceed 0.45, the specific heat capacity of cellular concrete will decrease with an increase of w/c. The proportion of fly ash has a similar effect on the specific heat capacity of cellular concrete. The proportion of slag has a different influence on the specific heat capacity of cellular concrete.

### *3.3.5 Response Optimization*

In MINITAB, response optimization is helpful to identify the combination of variable settings that jointly optimize a set of responses. The response optimization function is also useful

when evaluating the impact of multiple variables (foam, water, cement, fly ash, and slag) on a set of responses (28 days compressive strength, and thermal conductivity of cellular concrete). Table 3.39 presents the preset parameters including target value, lower value, and upper value of the responses (the predicted 28-day compressive strength and the thermal conductivity of cellular concrete).

**Table 3.39** Optimal design parameters.

| | Goal | Lower | Target | Upper | Weight | Importance |
|---|---|---|---|---|---|---|
| 28-days compressive strength | Target | 7.0 MPa | 8.0 MPa | 10.0 MPa | 1 | 0.1 |
| Thermal conductivity | Target | 0.1 W/m·℃ | 0.2 W/m·℃ | 0.3 W/m·℃ | 1 | 0.9 |

Table 3.40 shows the predicted mix design of cellular concrete, and Table 3.41 presents the predicted compressive strength and thermal conductivity of cellular concrete. The predictions indicated that the thermal conductivity of cellular concrete could reach 0.25 W/m·℃ under the premise of ensuring sufficient strength (Figure 3.30).

**Table 3.40** Global solution.

| Component | Volume | Mix proportion |
|---|---|---|
| Foam | 0.4000000 | 400 liter/$m^3$ |
| Water | 0.4165950 | 416.6 kg/$m^3$ |
| Cement | 0.0940850 | 296.4 kg/$m^3$ |
| Fly ash | 0.0371200 | 114.7 kg/$m^3$ |
| Slag | 0.0522000 | 145.1 kg/$m^3$ |
| Total | 1 | --- |

**Table 3.41** Predicted response.

| Properties | Predicted response |
|---|---|
| 28-days compressive strength | 8.19452 MPa |
| Thermal conductivity | 0.24947 W/m·℃ |

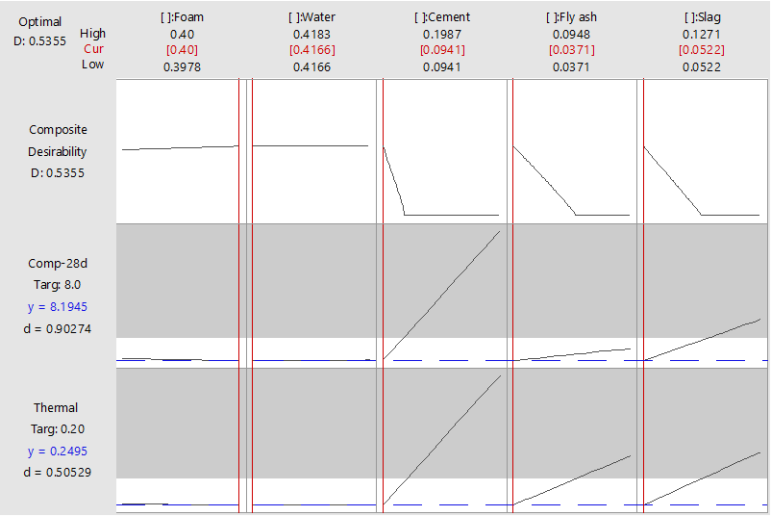


**Figure 3.30** Optimization plot.

# CHAPTER 4.0 NUMERICAL SIMULATION

In this chapter, the authors discuss the physical models and governing equations of air convection in a porous medium. A series of numerical simulations were used to investigate the performance of cellular concrete, crushed-rock ACE, and commonly used sand/gravel embankment. Case 1 corresponds to a compacted sand/gravel embankment, and Case 2 corresponds to a crushed-rock ACE, whereas Case 3 corresponds to a cellular concrete ACE. The results for the three cases are compared and discussed.

**Nomenclature**

| | | | |
|---|---|---|---|
| $\overrightarrow{B_f}$ | Body force term of the momentum equation | | *Greek symbols* |
| $C_2$ | Inertial resistance factor…….(1/m$^2$) | $\alpha$ | Permeability of porous media…….....m$^2$ |
| $c_p$ | Specific heat capacity……..….. J/(kg·℃) | β | Thermal expansion coefficient…..…(1/℃) |
| $E$ | Energy term | $\gamma$ | Porosity |
| $g$ | Gravity acceleration……..m/s$^2$ | $\lambda$ | Thermal conductivity ……...……W/(m·℃) |
| $h$ | Sensible enthalpy | $\mu$ | Dynamic viscosity of air……..…kg/m· s |
| $J$ | Diffusion flux | $\bar{\bar{\tau}}$ | Stress tensor |
| $L$ | Latent heat……..…J/kg | $\rho$ | Density……....kg/m$^3$ |
| $p$ | Pressure…….Pa | $\rho_f$ | The density of fluid……..…...kg/m$^3$ |
| $S_m$ | Source term for mass equation | $\rho_s$ | The density of solid……..……...kg/m$^3$ |
| $S_i$ | Source term for the $i$th (x or y) momentum equation | $\rho_0$ | The (constant) density of the air flow…….kg/m$^3$ |
| $t$ | Time……...day | | |
| $T$ | Temperature…….℃ | | *Subscripts* |
| $T_0$ | Operating temperature……℃ | $f$ | Fluid or frozen |
| $T_{ref}$ | Reference temperature……℃ | $s$ | Solid |
| $\vec{v}_s$ | Superficial velocity…….....m/s | $t$ | Thawed |
| $\vec{v}_p$ | Physical velocity…….m/s | u | Unfrozen |
| $\vec{v}$ | Velocity vectors…...……...m/s | e | Effective value |
| $v_i$ | Velocity in *i*-direction (*i*=*x* or *y*)…….m/s | m | Mass |
| $\|v\|$ | Magnitude of the velocity$\sqrt{v_x^2 + v_y^2}$…...m/s | $x$ | x-direction |
| $Y$ | The mass fraction | $y$ | y-direction |

## 4.1 Mathematical Representation

In this study, ACEs are constructed by utilizing crushed rocks or cellular concrete blocks, resulting in very high air permeability. For this reason, the embankments can be considered as porous media. In winter, the ambient temperature is lower than the underlying permafrost temperature. An unstable air density gradient that formed within the embankment during cold winters results in pore air convection. The air convection accelerated heat removal from the embankment during cold periods, and the heat transfer pattern is dominated by both conduction and convection. In summer, natural convection does not occur due to the stable air density gradient. Thus, the summer-time heat transfer mode is mainly heat conduction, which transfers heat less effectively (Goering and Kumar, 1996; Goering, 1998, 2003).

Besides, a convectional sand/gravel embankment was also simulated in this study for comparison purposes. Different from ACE, the heat transfer in the sand/gravel embankment was mainly through heat conduction. Therefore, the sand/gravel embankment model and the ACE models are discussed separately in this study. Under these conditions, governing equations of porous media zone and heat transfer equations of solid zone can be written as shown in the next section (Nield and Bejan, 2011; Fluent, 2019a, 2019b).

### *4.1.1 Governing Equations of Porous Media Zone*

In the ACE models, the governing differential equations for the heat transfer through the porous media (embankment) were derived based upon thermal equilibrium between the solid medium (cellular concrete blocks or crushed rocks) and the fluid flow (air).

The superficial velocity was calculated based on the volumetric flow rate. The superficial velocity in the governing equations can be represented as:

$$\vec{v}_s = \gamma \vec{v}_p \tag{4.1}$$

Where $\gamma$ is the porosity of the porous media defined as the ratio of the volume occupied by the fluid to the total volume. Where $\vec{v}_p$ is the true or physical velocity throughout the flow field, and $\vec{v}_s$ is the superficial velocity of the flow field (Nield and Bejan, 2011; Fluent, 2019b).

The physical velocity formulation was used in the following equations. To simplify the representation, $\vec{v}_p$ was abbreviated as $\vec{v}$. Assuming the porous media is of isotropic porosity and the fluid medium is single-phase flow, the governing equations are as follows (Fluent, 2019a, 2019b; Zhang et al., 2006):

**Mass conservation equations:**

$$\frac{\partial(\gamma\rho_f)}{\partial t} + \nabla \cdot (\gamma\rho_f \vec{v}) = S_m \tag{4.2}$$

Equation 4.2 is the general form of the mass conservation equation and is valid for incompressible as well as compressible flows (Fluent, 2019a). The source term $S_m$ is the mass added to the continuous phase from the dispersed second phase. In this study, the numerical models are two-dimensional and the source term $S_m$ can be ignored, thus the volume-averaged mass equation can be simplified as follows (Zhang et al., 2006; Fluent, 2019a):

$$\frac{\partial(\gamma\rho_f)}{\partial t} + \left[ \frac{\partial(\gamma v_x)}{\partial x} + \frac{\partial(\gamma v_y)}{\partial y} \right] = 0 \tag{4.3}$$

Where *x, y* are the axial coordinates, $v_x, v_y$ are the axial velocities of air in the *x* direction and the *y* direction.

**Momentum equations:**

$$\frac{\partial\left(\gamma\rho_f v_i\right)}{\partial t}+\nabla\cdot\left(\gamma\rho_f v_i\vec{v}\right)=-\gamma\nabla p+\nabla\cdot\left(\gamma\bar{\bar{\tau}}\right)+\gamma\vec{B}_f+S_i \tag{4.4}$$

The first two terms on the right-hand side of Equation 4.4 represent two surface force terms, the pressure term and the stress tensor term. The third term means body force term; in this problem, it is generated from gravitational body force (Fluent, 2019a). Moreover, the last term on the right-hand side represents the source terms $S_i$ in porous media, which will be described in detail in Equation 4.5.

Porous media are modeled by the addition of a momentum source term to the standard fluid flow equations. The source term is composed of two parts: a viscous loss term (Darcy term, the first term on the right-hand side of Equation 4.5), and an inertial loss term (the second term on the right-hand side of Equation 4.5). For a simple homogeneous porous medium, the source term is (Fluent, 2019a, 2019b):

$$S_i=-\left(\frac{\gamma^2\mu}{\alpha}v_i+\frac{\gamma^3 C_2}{2}\rho_f|v|v_i\right) \tag{4.5}$$

Where $S_i$ is the source term for the $i$th (*x* or *y*) momentum equation, $|v|$ is the magnitude of the velocity, $\alpha$ is the permeability of porous media, which is a measure of the ability of a material (such as crushed rocks) to transmit fluids (air), and $C_2$ is the inertial resistance factor in porous media.

The momentum conservation equation can be decomposed into *x*-direction and *y*-direction as follows (Fluent, 2019a, 2019b):

*x*-direction:

$$\frac{\partial\left(\gamma\rho_f v_x\right)}{\partial t}+\nabla\cdot\left(\gamma\rho_f v_x \vec{v}\right)=-\gamma\frac{\partial p}{\partial x}+\nabla\cdot\left(\gamma\bar{\bar{\tau}}\right)-\left(\frac{\gamma^2\mu}{\alpha}v_x+\frac{\gamma^3 C_2}{2}\rho_f\left|\vec{v}\right|v_x\right) \tag{4.6a}$$

*y*-direction:

$$\frac{\partial\left(\gamma\rho_f v_y\right)}{\partial t}+\nabla\cdot\left(\gamma\rho_f v_y \vec{v}\right)=-\gamma\frac{\partial p}{\partial y}+\nabla\cdot\left(\gamma\bar{\bar{\tau}}\right)-\gamma\rho_f g-\left(\frac{\gamma^2\mu}{\alpha}v_y+\frac{\gamma^3 C_2}{2}\rho_f\left|\vec{v}\right|v_y\right) \tag{4.6b}$$

To get faster convergence of the model, the Boussinesq approximation is employed in the numerical simulation. The Boussinesq model is set up with density as a function of temperature. This model treats density as a constant value in all solved equations, except for the buoyancy term (gravitational body force term) in the momentum equation (Zhang et al., 2006; Nield and Bejan, 2011; Fluent, 2019b):

$$\left(\rho-\rho_0\right)g\approx-\rho_0\beta\left(T-T_0\right)g \tag{4.7}$$

Where $\rho_0$ is the (constant) density of the air flow, $T_0$ is the operating temperature, and $\beta$ is the thermal expansion coefficient. Equation 4.7 is obtained by using the Boussinesq approximation $\rho=\rho_0(1-\beta\Delta T)$ to eliminate $\rho$ from the buoyancy term. This approximation is accurate as long as changes in actual density are small; specifically the Boussinesq approximation is valid when $\beta(T-T_0)\ll 1$.

**Energy equations:**

The thermal equilibrium energy equation for the numerical solution was

$$\frac{\partial}{\partial t}\left(\gamma\rho_f E_f + (1-\gamma)\rho_s E_s\right) + \nabla\cdot\left(\vec{v}\left(\rho_f E_f + p\right)\right) = \nabla\cdot\left[\lambda_e \nabla T - \left(\sum_i h_i J_i\right) + \left(\bar{\bar{\tau}}\cdot\vec{v}\right)\right] + S_f^h \qquad (4.8)$$

The first three terms on the right-hand side of Equation 4.8 represent energy transfer due to conduction, species diffusion, and viscous dissipation, respectively (Fluent 2019a).

The conduction flux in the porous medium uses an effective conductivity, and the transient term includes the thermal inertia of the solid region in the medium. The effective thermal conductivity in the porous medium (embankment), $\lambda_e$, is defined as the volume average of the fluid conductivity, $\lambda_f$, and solid conductivity, $\lambda_s$ (Nield and Bejan, 2011; Fluent 2019a):

$$\lambda_e = \gamma\lambda_f + (1-\gamma)\lambda_s \qquad (4.9)$$

In Equation 4.8,

$$E = h - \frac{p}{\rho} + \frac{v^2}{2} \qquad (4.10)$$

Where, in this problem, the sensible enthalpy $h$ is defined for incompressible flows as (Fluent 2019a):

$$h = \sum_j Y_j h_j + \frac{p}{\rho} \qquad (4.11a)$$

In Equation 4.11a, $Y_j$ is the mass fraction of species $j$ and

$$h_j = \int_{T_{ref}}^{T} c_{p,j}\, dT \qquad (4.11b)$$

The value used for $T_{ref}$ in the calculation of sensible enthalpy depends on the solver and models in use. For the pressure-based solver $T_{ref}$ is 298.15 K (25°C). $c_{p,j}$ is the thermal conductivity of species $j$ (Fluent, 2019a).

### *4.1.2 Heat Transfer Equations of Solid Zone*

In solid regions (the sand/gravel embankment and the permafrost), the energy transport equation has the following form (Fluent 2019a):

$$\frac{\partial}{\partial t}(\rho h) = \nabla \cdot (k \nabla T) + S_s^h \tag{4.12}$$

Where the first term on the right-hand side is the heat flux due to conduction and the second term on the right-hand side is the volumetric heat sources within the solid.

In this research, Equation 4.12 can be simplified as (Zhang et al., 2006; Nield and Bejan, 2011; Fluent 2019a):

$$C_e^* \frac{\partial T}{\partial t} = \frac{\partial}{\partial x}\left( \lambda_e^* \frac{\partial T}{\partial x} \right) + \frac{\partial}{\partial y}\left( \lambda_e^* \frac{\partial T}{\partial y} \right) \tag{4.13}$$

To simulate phase change considering the latent heat of the solid regions, the effective specific heat capacity, $C_e^*$, and the effective thermal conductivity, $\lambda_e^*$ in Equation 4.13 can be expressed as functions related to latent heat $L$. Using the method of sensible heat capacity, the phase change is assumed to occur in a range of temperature ($T_t \mp \Delta T$), (Zhang et al., 2006, 2009).

$$C_e^* = \begin{cases} C_f & T < (T_t - \Delta T) \\ C_f + \dfrac{C_t - C_f}{\Delta T}\left[ T - (T_t - \Delta T) \right] & (T_t - \Delta T) \le T \le T_t \\ C_t - \dfrac{C_t - C_u}{\Delta T}(T - T_t) & T_t < T \le (T_t + \Delta T) \\ C_u & T > (T_t + \Delta T) \end{cases} \tag{4.14}$$

$$\lambda_e^* = \begin{cases} \lambda_f & T < (T_t - \Delta T) \\ \lambda_f + \dfrac{\lambda_u - \lambda_f}{2\Delta T}\left[T - (T_t - \Delta T)\right] & (T_t - \Delta T) \le T \le (T_t + \Delta T) \\ \lambda_u & T > (T_t + \Delta T) \end{cases} \tag{4.15}$$

Where subscripts *f*, *t* and *u* represent the frozen, thawed and unfrozen states, respectively. $C_f$, $C_t$, and $C_u$ are volumetric heat capacity of solid regions in the frozen, thawed, and unfrozen states, respectively. The value used for $T_t$ is 0℃, and for $\Delta T$ is 0.2℃.

In Equations 4.14 and 4.15, $C_t$ can be expressed as (Zhang et al., 2006):

$$C_t = \frac{L}{\Delta T} + \frac{C_f + C_u}{2} \tag{4.16}$$

From the governing equations in porous media zone (air convection embankment), and heat transfer equations in solid zone (sand/gravel embankment or permafrost layer), the temperature, pressure and velocity fields in the numerical model can be calculated.

However, the couple, profoundly nonlinear partial differential equations mentioned above have no analytical solutions. In this study, the temperature, velocity, and pressure fields were obtained using the numerical method. Three finite element models: the sand/gravel embankment, the crushed-rock ACE, and the cellular concrete ACE were simulated numerically by using the commercial finite element software ANSYS Fluent 19.1.

**4.2 Numerical Simulation**

In this study, the numerical models of the three cases have the same geometry properties. The physical domains are extended to 9.0 m from the foot of the side slope and 9.0 m of depth

from the native ground surface (Figure 4.1). The temperature and heat flux boundary conditions are required for each edge of the computational domain.

### *4.2.1 Physical Domain*

As is shown in Figure 4.1, the physical domain consists of two parts, the embankment, and the permafrost layer. The embankments of the three cases are assumed impermeable at all surfaces. The pavement is made of an asphalt-concrete layer, and the two side slopes are covered with impermeable geotextiles. A thin covering of topsoil on the geotextiles could be employed to stabilize the coating. The permafrost layer consists of uniform silt with high moisture content. Moreover, the permafrost layer contains many ice lenses and ice wedges in the foundation soil. The geometry corresponds to the numerical model of a highway embankment with the pavement surface width of 6.0 m and the height of 2.5 m, respectively, the specific dimensions information of the embankment is shown in Figure 4.1.

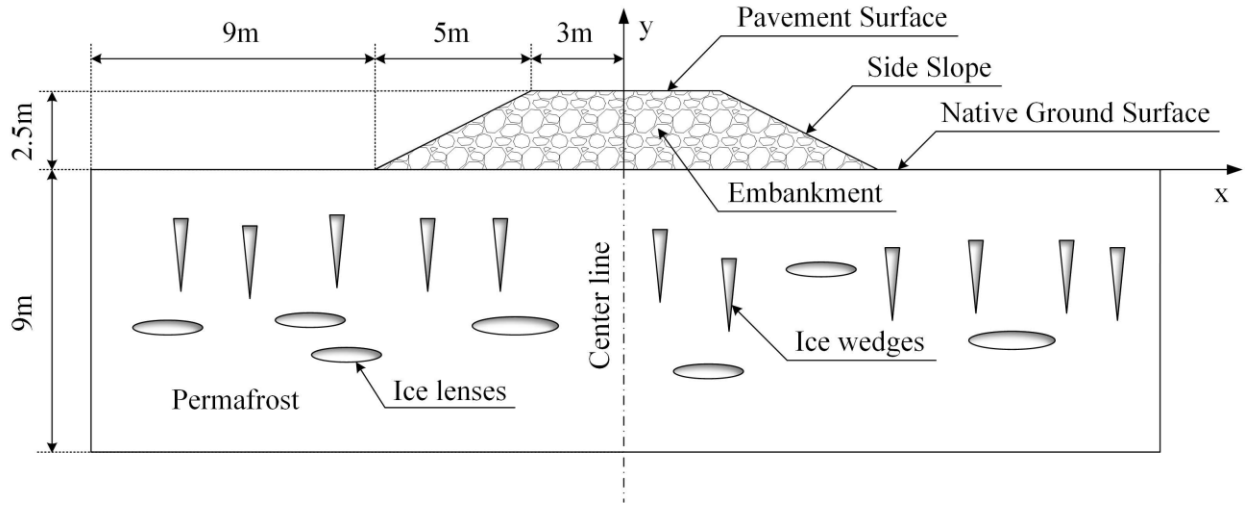


**Figure 4.1** Air convection embankment model.

### *4.2.2 Boundary Conditions*

The temperature boundary conditions of the pavement surface, the embankment side slope, and the native ground surface are shown in Table 4.1, where *t* is the time in days. The yearly average temperatures of the pavement surface, the embankment side slopes, and the native ground surface are given as 1.1℃, 2.7℃, and -1.9℃, respectively, and a phase lag of 9 days from July first has also been utilized. The temperature functions in Table 4.1 are based on the observed yearly temperature data of Fairbanks, Alaska area (Goering and Kumar, 1996). At the lower boundary of the permafrost layer, the boundary condition is considered by using the geothermal heat flux of 0.06 $W/m^2$ (Goering and Kumar, 1996; Zhang et al., 2006). The left side and right side of the permafrost layer are assumed adiabatic. The interface of the embankment and the permafrost is simulated with conjugate heat transfer condition.

In this numerical study, it is assumed that there is no air flow cross any boundary of the models. As mentioned above, each side of the embankment is covered with geotextiles, and the permafrost layer consists of uniform silt with high moisture content. Thus, both the embankment boundaries and the permafrost domain are impermeable. Therefore the default zero flow velocity boundary conditions were employed at each boundary of the physical domain. Similarly, the pressure boundary conditions were set as the default value of zero.

**Table 4.1** Temperature boundary conditions at the upper surfaces (in Fairbanks, Alaska).

| Surfaces (Figure 4.1) | Temperature function (℃) |
|---|---|
| Pavement surface | $1.1-26.1\cos\left(\frac{2\pi}{365}(t-9)\right)$ |
| Embankment side slope | $2.7-20.9\cos\left(\frac{2\pi}{365}(t-9)\right)$ |
| Native ground surface | $-1.9-10.0\cos\left(\frac{2\pi}{365}(t-9)\right)$ |

### *4.2.3 Material Properties*

In the embankment models, the sand/gravel embankment are constructed of packed sand and gravel, the permeability of the embankment is approximately $\alpha = 3 \times 10^{-11} m^2$, the value of which is too small to generate natural convection in the embankment. So the sand/gravel embankment can be considered as impermeable. For the crushed-rock ACE and the cellular concrete ACE, it is assumed that the crushed rocks and the cellular concrete blocks have the same stacked form, and the average diameter of the rocks and cellular concrete is 3-4 inches (7.6-10.2 centimeters). Thus both the crushed-rock embankment and the cellular concrete embankment have the same porosity of $\gamma = 40\%$ and the same permeability of $\alpha = 6.32 \times 10^{-7} m^2$, which means that the embankments that are of highly permeability (Goering and Kumar, 1996). The viscous resistance (inverse absolute permeability) is $1/\alpha = 1.582 \times 10^6 (1/m^2)$ and the inertial resistance is $C_2 = 3733.34 m^{-1}$ (Goering and Kumar, 1996; Zhang et al., 2006). For the air in the porous media, the dynamic viscosity and the thermal expansion coefficient are $1.725 \times 10^{-5} kg/(m \cdot s)$, and $0.00369(1/℃)$, respectively, under the reference temperature of 0 ℃.

For the three cases, the permafrost layer is ice-rich silt with a moisture content of 45% and a dry density of $1442\text{kg}/m^3$ , and a fresh density of $2090.9\text{kg}/m^3$ (Goering and Kumar, 1996). The high content of moisture would suffer a serious freeze and thaw yearly cycle in the active permafrost layer, resulting in thaw settlement under the embankment. In addition, the density, specific heat capacity, and thermal conductivity of the modeling materials are listed in Table 4.2 (Goering and Kumar, 1996; Samson et al., 2016). It should be pointed out that the main difference between Case 1, 2 and 3 are the physical properties of the embankments. Case 1 did not set up the porous media model in ANSYS Fluent due to its impermeable characteristic. The physical properties of the permafrost layer and the boundary conditions of the three models are identical.

Physical properties of the materials in the numerical models.

**Table 4.2** Physical properties of the materials in the numerical models.

| Properties | ρ kg/m$^3$ | $C_f$ J/(kg·℃) | $\lambda_f$ W/(m·℃) | $C_u$ J/(kg·℃) | $\lambda_u$ W/(m·℃) | $L$ J/kg |
|---|---|---|---|---|---|---|
| Silty Sand/gravel | 1600 | 1012.5 | 2.15 | 1243.8 | 1.99 | 16250 |
| Crushed rock | 2600 | 386.9 | 0.346 | 386.9 | 0.346 | $\approx 0$ |
| Cellular concrete | 1250 | 1000 | 0.2 | 1000 | 0.2 | $\approx 0$ |
| Air in porous media | 1.292 | 1003.8 | 0.02428 | 1003.8 | 0.02428 | $\approx 0$ |
| Permafrost layer | 2090.9 | 908.8 | 2.32 | 1426.5 | 1.49 | 82767.6 |

Note: ρ- density; $C$- specific heat capacity; $\lambda$- thermal conductivity; the subscript *f* and *u* represent unfrozen and frozen states, respectively; $L$- latent heat.

### *4.2.4 Modeling Procedures*

For the numerical simulation, the three models are created using quadrilateral mesh. There are 722 elements and 1606 nodes for the embankment zone and 7650 elements and 15732

nodes for the permafrost zone. Thus, the physical domain consists of 8372 elements and 17338 nodes. The gird was approximately 0.5 m for the whole domain.

The first step is to create a permafrost model using the boundary conditions and material properties described above. The purpose of this step is to obtain the temperature field of the permafrost layer before roadway construction. A time step of one day was employed with a total simulation time of 30 years (Figure 4.2). After 10 years calculation, the temperature field tends to be stable at every specific time of each year, and after 20 years calculation, the temperature field became stable. Finally, the temperature field of the foundation soil (permafrost layer) on July 1 of the 30$^{th}$ year was obtained through a long-term transient solution. Figure 4.2a showed the instantaneous isotherms of the permafrost layer on July 1 of the 30$^{th}$ year. Figure 4.2b illustrated the temperature at different depths below the native ground surface.

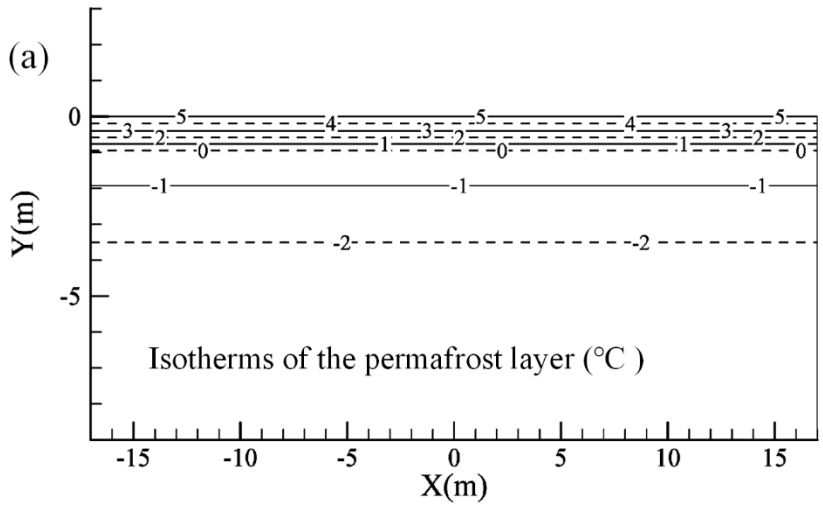

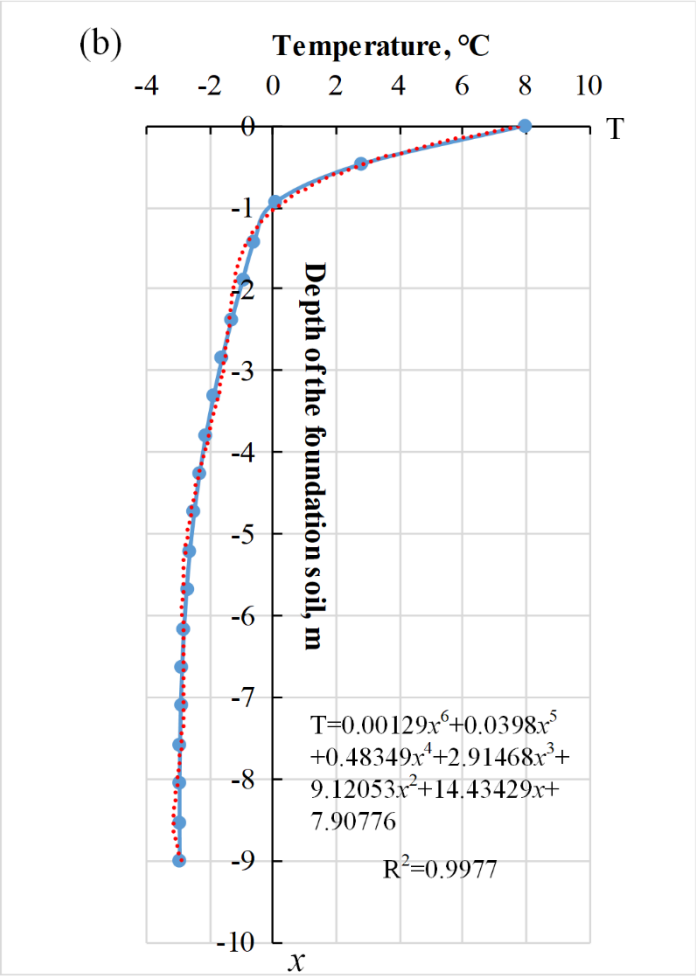


**Figure 4.2** The temperature field of the foundation soil on July 1 (in Fairbanks, Alaska). (a) Isotherms for foundation soil. (b) Soil temperatures at different depths below the native ground surface.

The second step is to create the embankment and permafrost model to simulate the temperature variation after the embankment construction practice. The initial temperature field of permafrost mentioned above was imported to the permafrost zones of the three cases. Moreover, the initial temperature field of the embankment was set as 15℃, which was the approximate average atmospheric temperature on July 1 for Fairbanks, Alaska area. A time step of one day was used with a total simulation time of 10 years. The data were stored for the first day of each

month of the 10 years. The temperature field and velocity field for the final year ($10^{th}$ year) were employed to generate the present plot in section 4.3.

## 4.3 Result and Analyses

The temperature profiles of the convectional sand/gravel embankment and the ACEs are shown in Figures 4.3-4.5. The most important for data analysis are the position and monthly motion of the 0℃ isotherm. In addition, the natural convection patterns of air in the embankment are of vital importance. The numerical models are symmetrical, so the left side and the right side have the same isotherm and velocity pattern. In the plots of Figures 4.3-4.5, the left side displays the temperature field, and the right side displays the air velocity field, which nicely illustrates the heat transfer modes and natural convection pattern in the embankments. These plots are shown for only the upper 5.0 m of permafrost layer and 17.0 m left/right side from the centerline of the embankment even though the simulations extend to a depth of 9.0 m of the permafrost layer.

### *4.3.1 Case 1, Sand/gravel Embankment*

The embankment in Case 1 was constructed using compacted sand/gravel, so the embankment is impermeable, which results in no air convection in the embankment. Consequently, the heat transfer pattern is thermal conduction only.

Figures 4.3a-c show the isotherms and the velocity vectors of the sand/gravel embankment on June 1, November 1, and January 1. The left half of Figure 4.3a displays the isotherms of the embankment on June 1. As observed, the embankment that consists of sand/gravel with 10% moisture was entirely thawed by that date. Half of the active permafrost

layer under the embankment was thawed. Most areas of the interface between the embankment and the permafrost, near the centerline, were in the thawing stage. The right half of the embankment is the velocity vectors plot; however, there is no natural convection or air motion in the embankment due to the impermeable property of the embankment.

Figure 4.3b shows that the cold ambient air began cooling the embankment and the native ground surface. However, there was a thermal center in the embankment, and the heat continued transferring from the embankment to the foundation soil. As shown in Figure 4.3b, the permafrost layer under the embankment was completely thawed, and the 0℃ isotherm moved down to approximately -2.0 m of depth. As a result, the embankment and the permafrost layer became unstable.

On January 1, the whole embankment was frozen again, and the temperature of the interface between the embankment zone and the permafrost zone was below 0℃. However, there was a large zone of thawed soil beneath the embankment, in which it is easy to trigger thaw settlement. The thaw was processing downward through the foundation soil (Figure 4.3c).

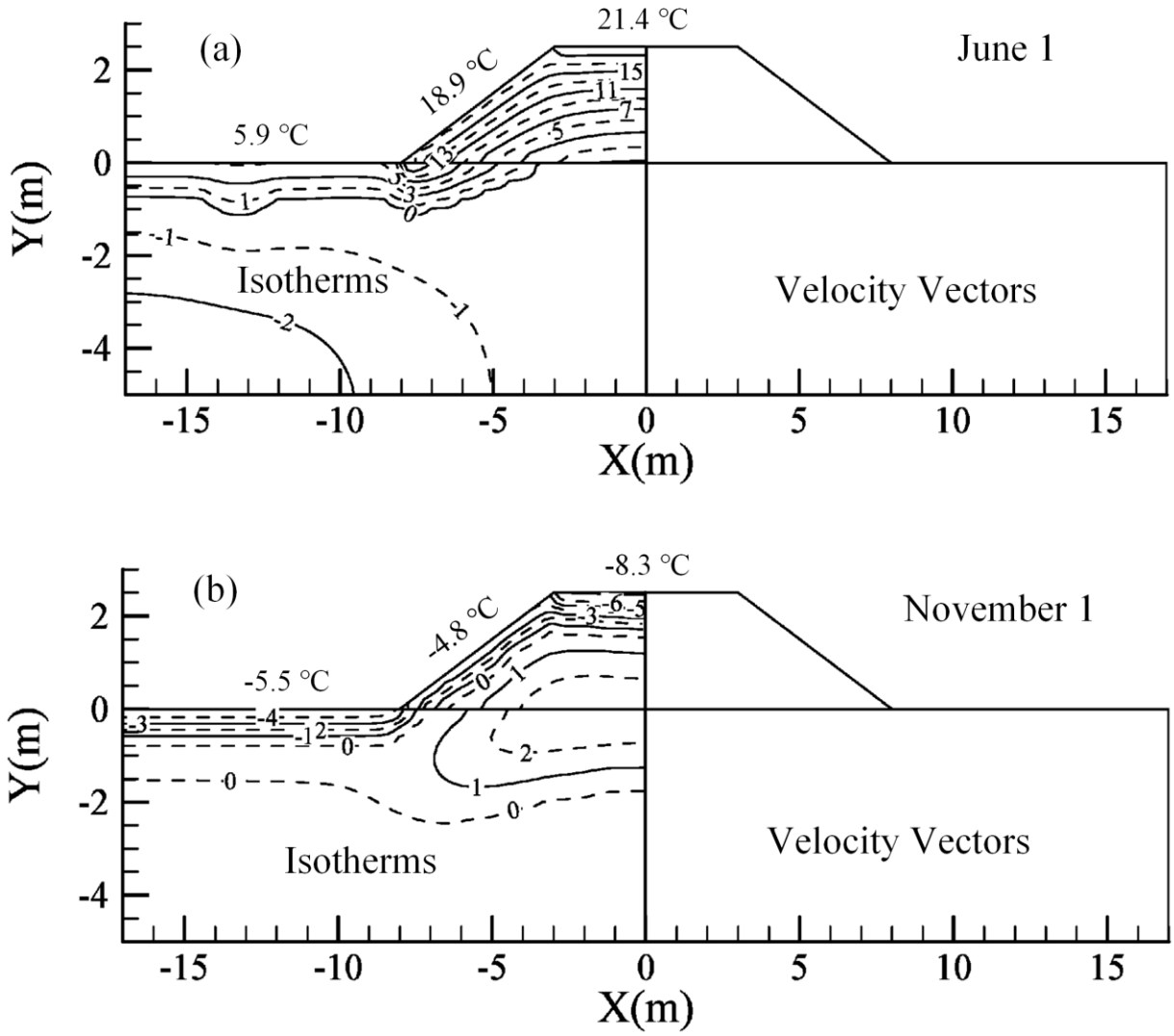
(a)
June 1
21.4 °C
18.9 °C
5.9 °C
Isotherms
Velocity Vectors
Y(m)
X(m)
(b)
November 1
-8.3 °C
-4.8 °C
-5.5 °C
Isotherms
Velocity Vectors
Y(m)
X(m)

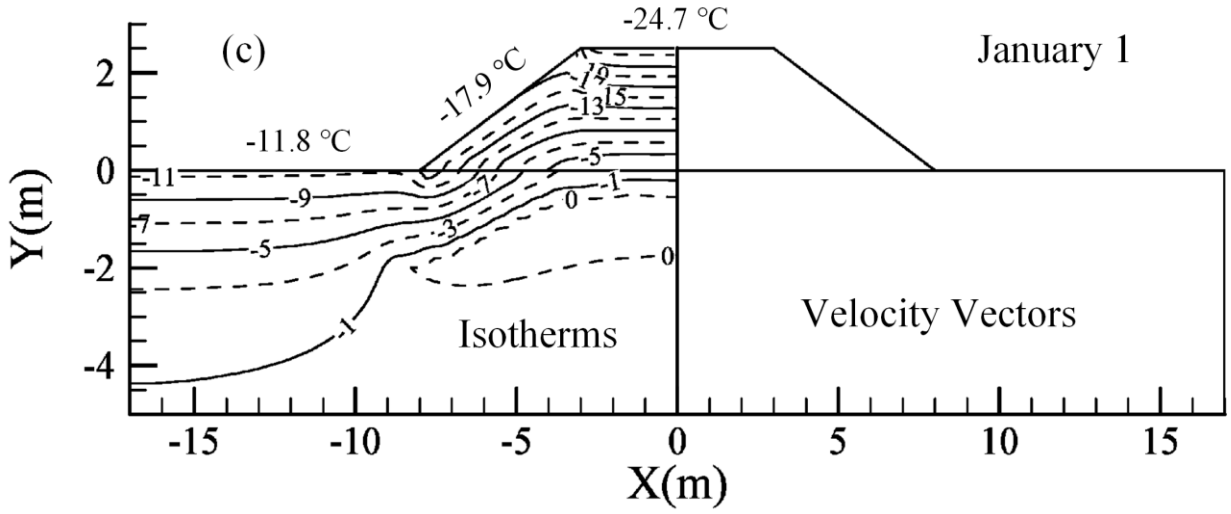


**Figure 4.3** Instantaneous isotherms (℃) and velocity vectors for Case 1, the sand/gravel embankment, conduction. (a) June 1. (b) November 1. (c) January 1.

### *4.3.2 Case 2, Crushed-rock ACE*

A typical ACE model constructed with crushed rocks was presented here. The ambient temperature and the thermal properties of the crushed rocks influence the intensity and patterns of the thermal convection and conduction of the embankment. Figures 4.4a-g illustrate the isotherms and the velocity vectors of air in the porous embankment.

Figure 4.4a shows a typical heat transfer pattern occurring in ACE during summer. Due to the stable density gradient of air in the embankment, there is no air movement in the embankment; the heat transfer pattern is conduction only. Figures 4.4b-e display the influence of ambient temperature change on the heat transfer pattern in the embankment and the permafrost layer in cold seasons. From October 1 to January 1, the air convection in the embankment became more and more violent; several air eddies formed in the embankment. The natural convection changed the heat transfer pattern from conduction to air convection and solid

conduction, which speed up the heat transfer in the embankment. The cooling effect keeps the permafrost layer beneath the embankment frozen and stable. On March 1 and April 1 (Figures 4.4f-g), the ambient temperatures around the embankment gradually increased, and the air convection in the embankment became much weaker. The air eddies in the embankment gradually disappeared.

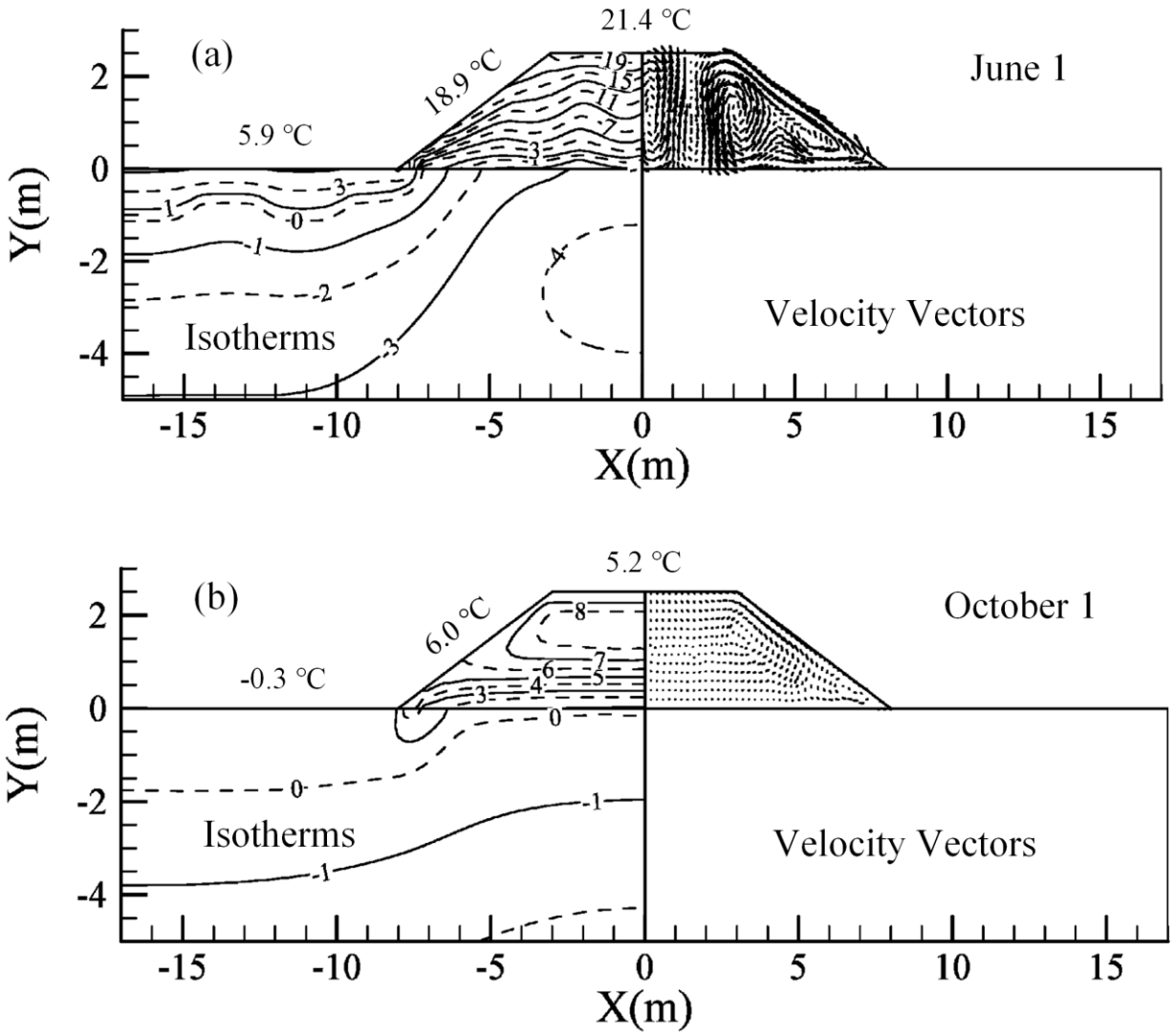

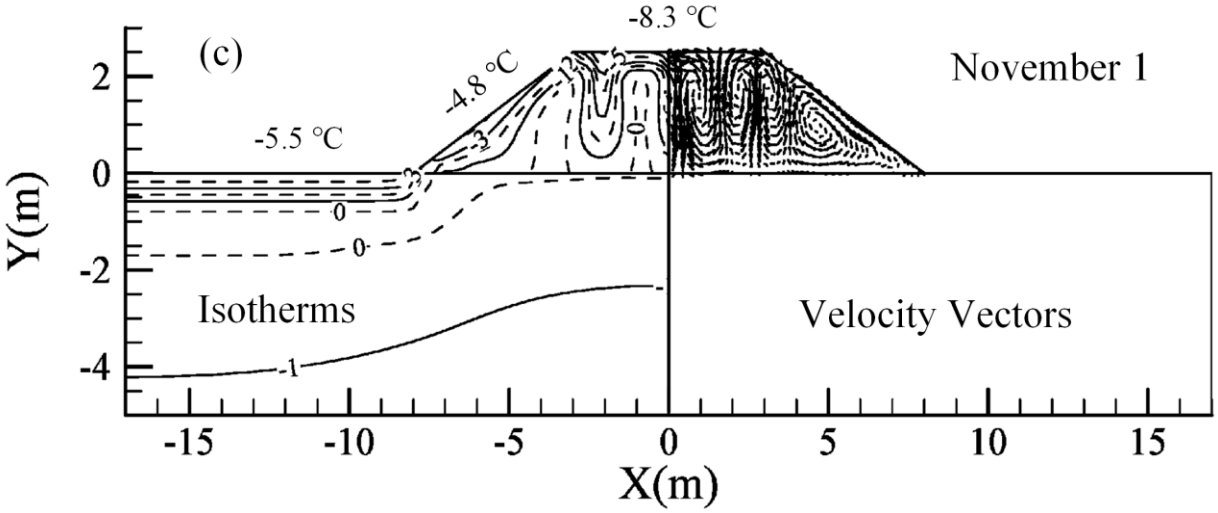
(c)
November 1
-8.3 °C
-4.8 °C
-5.5 °C
Isotherms
Velocity Vectors
Y(m)
X(m)

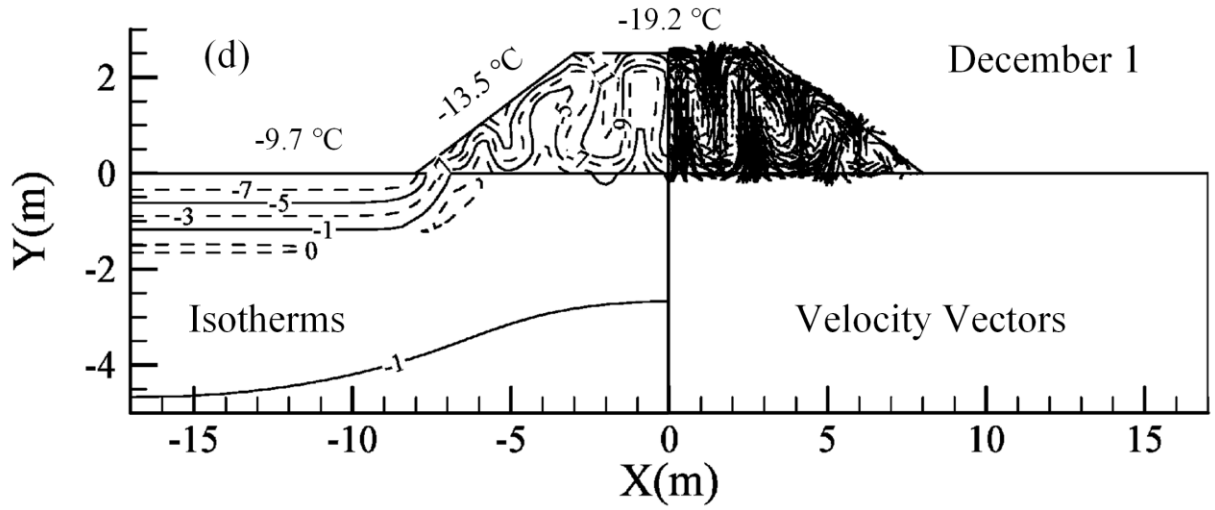
(d)
December 1
-19.2 °C
-13.5 °C
-9.7 °C
Isotherms
Velocity Vectors
Y(m)
X(m)

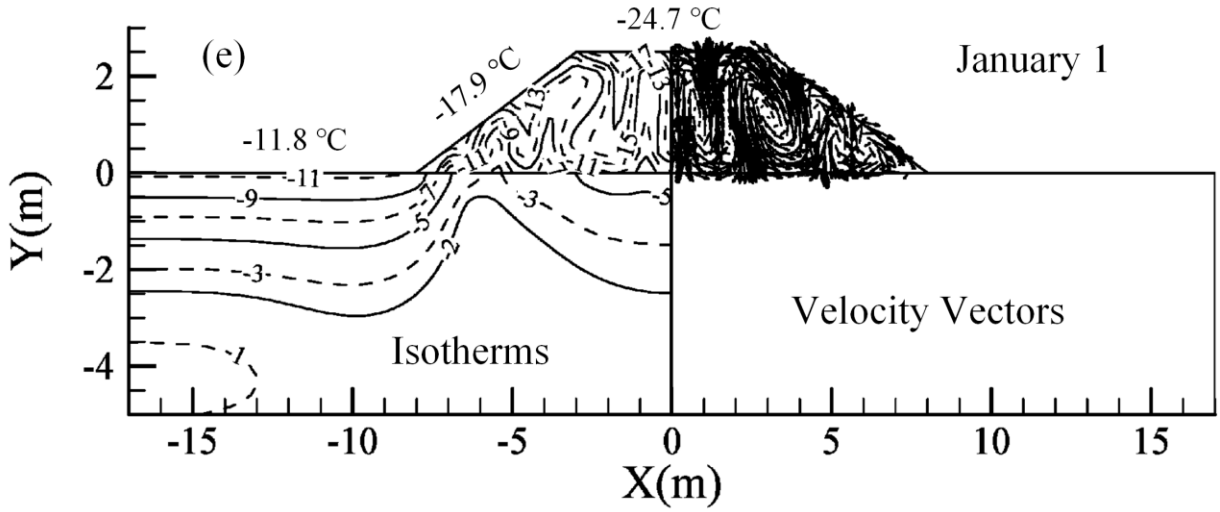
(e)
January 1
-24.7 °C
-17.9 °C
-11.8 °C
Isotherms
Velocity Vectors
Y(m)
X(m)

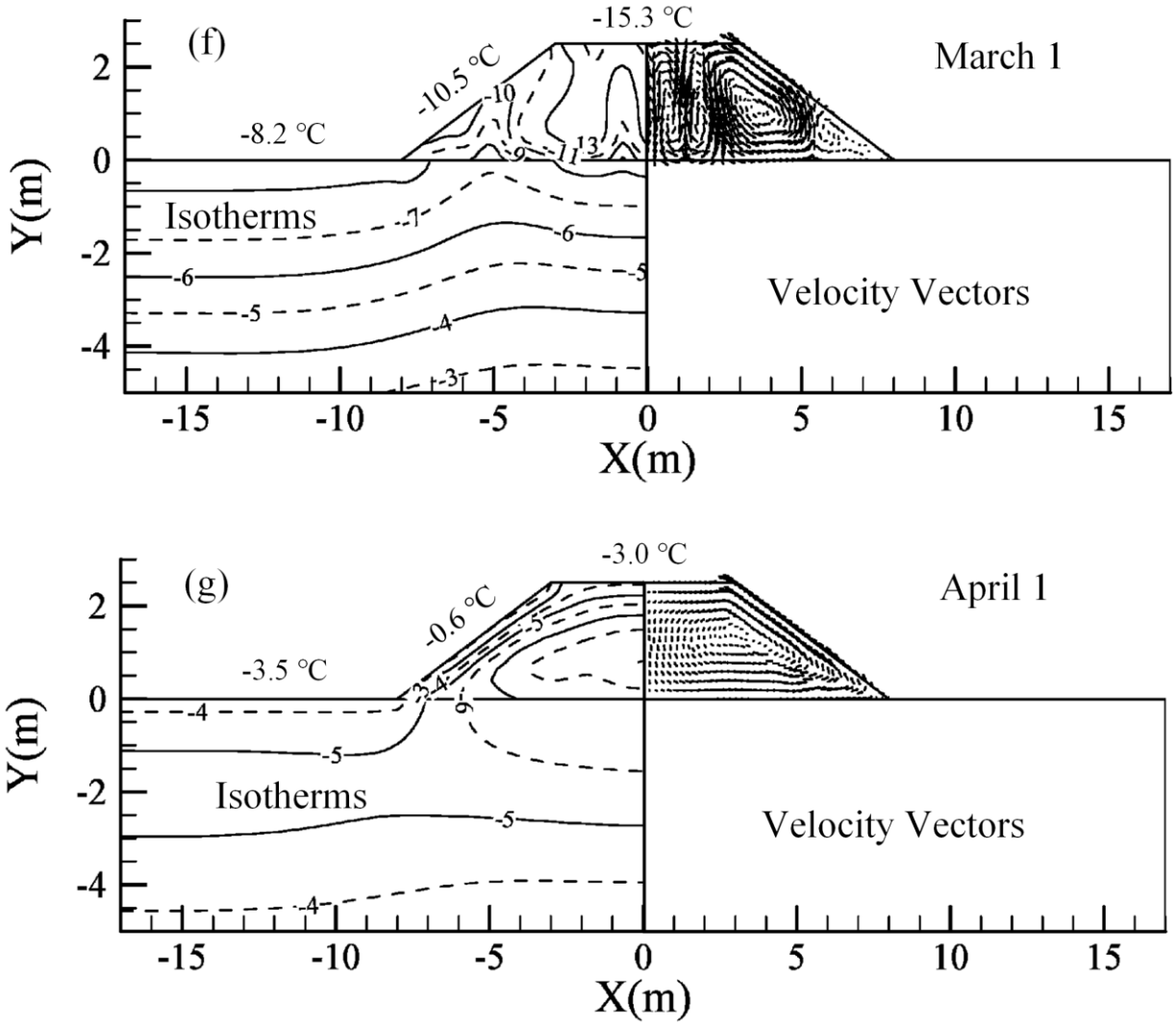


**Figure 4.4** Instantaneous isotherms (℃) and velocity vectors for Case 2, the crushed-rock embankment. (a) June 1. (b) October 1. (c) November 1. (d) December 1. (e) January 1. (f) March 1. (g) April 1.

### *4.3.3 Case 3, Cellular Concrete ACE*

In Case 3, the cellular concrete ACE was simulated by the finite element model. The heat transfer pattern of the cellular concrete ACE is similar to that of the crushed-rock ACE in Case 2.The isotherms and velocity vectors were displayed in the present plots of June 1, October 1,

November 1, December 1, January 1, March 1 and April 1, respectively, shown in Figures 4.5a-g.

Figure 4.5a shows a typical thermal pattern occurring in ACE during summer. The majority of the permafrost layer under the embankment remains frozen with a large zone that was colder than $-4℃$; the reason is that in summer there is almost no air convection in the ACE, the porous embankment turns to a thermal insulation layer to prevent the warm air and strong radiation from thawing the permafrost. Thus, even when the surface temperature of the pavement and side slope are approximately $20℃$, the temperature of the foundation soil under the embankment was much lower than the ambient temperature. Affected by the warm air and radiation, the temperature at the foot of the embankment was higher than $0℃$, which indicated that the permafrost was thawing. However, a small thawing region at the corner of the embankment will not have a big influence on the stability of the embankment. Away from the embankment, beneath the native ground, the permafrost layer thawed to a depth of approximately 1.0 m. The right side of Figure 4.5a depicts the velocity vectors of air in the embankment. The flow velocity within the embankment ranges from 0.0 m/s to $2.2 \times 10^{-3}$ m/s. Compared with Figure 4.5e in winter, the motion of air in Figure 4.5a was very gentle; there was no air eddy formed in the embankment, which results in a relatively uniformed temperature gradient, as shown in the left half of the plot.

Figures 4.5b-d shows a continuous change of the temperature field and velocity of air in porous media. Figure 4.5b shows that the thawing was extended to a depth of approximately 1.8

m under the native ground surface. The 0℃ isotherm line was moving downward. The ambient air temperature decreased, and the native ground began to freeze downward. At the same time, the cold ambient air begin to cool the embankment. The temperatures of the pavement, side slopes, and native ground decreased to $5.2℃, 6.0℃,$ and $-0.3℃$, respectively. As can be seen, there was an isotherms center in the embankment, and the temperature of the permafrost layer was still below 0℃.

On November 1, the ambient temperature lowered to below 0℃, which made the temperature gradient of the embankment become irregular (Figure 4.5c). Air motion in the embankment enhanced and distorted the isotherms from the horizontal orientation in June. It is observed that there was an unstable thermal center in the embankment. The warm air of the porous embankment moved upward and the cold air of the porous embankment moved downward. The active permafrost layer beneath the native ground froze again, and the isotherms under the embankment have no distinct difference from that of October 1.

On December 1 and January 1, Figures 4.5d-e display an obvious distortion of isotherms in the embankment. The temperature under the native ground surface continued to decrease. The heat under the embankment moved upward due to the natural convection in the embankment and the thermal conduction effect. On December 1, the temperature of the majority zone of the permafrost region under the embankment was below $-1℃$. On January 1, the temperature of the native ground surface continued to decrease, and finally reached $-11.8℃$. The temperature of the pavement and the side slopes reached $-24.7℃$ and $-17.9℃$, respectively, which

significantly enhanced the natural convection in the embankment. The temperature of the embankment-foundation interface continued to decrease to approximately $-4℃$. From December 1 to January 1, the ambient temperature is very low. As was seen in Figure 4.5d, there is a thin layer of temperature at $0℃$ in the foundation soil. When water changed from liquid to ice, a large amount of latent heat is needed. After the thin layer was frozen, less energy extraction is needed to lower the frozen soil temperature and the $-2℃$ isotherms rapidly drop on January 1 (Figure 4.5e). As shown in Figures 4.5d-e, the temperature under the native ground surface decreased faster than that under the embankment. The reason is that the thermal conductivity of air and cellular concrete are lower than that of the foundation soil; however, in wintertime, the temperature under the embankment was below $0℃$. In December, because of the density gradient, air motion developed five distinct clockwise eddies in half of the embankment, and the air motion became even stronger in January. The flow velocity within the embankment ranges from 0.0 m/s to $4.4 \times 10^{-3}$ m/s on January 1. The maximum velocity of air is twice as large as that on June 1.

With the ambient temperature increasing in March (Figure 4.5f), the air convection in the embankment became much weaker, and the five distinct strong eddies reduced to two weaker ones. However, the temperature under the embankment decreased to approximately $-6℃$. Compared with the isotherms on January 1, the isotherms became much gentle on March 1. On April 1, a new isotherms center was regenerated in the embankment, and the air eddies disappeared, so only weak air motion occurred in the embankment (Figure 4.5g).

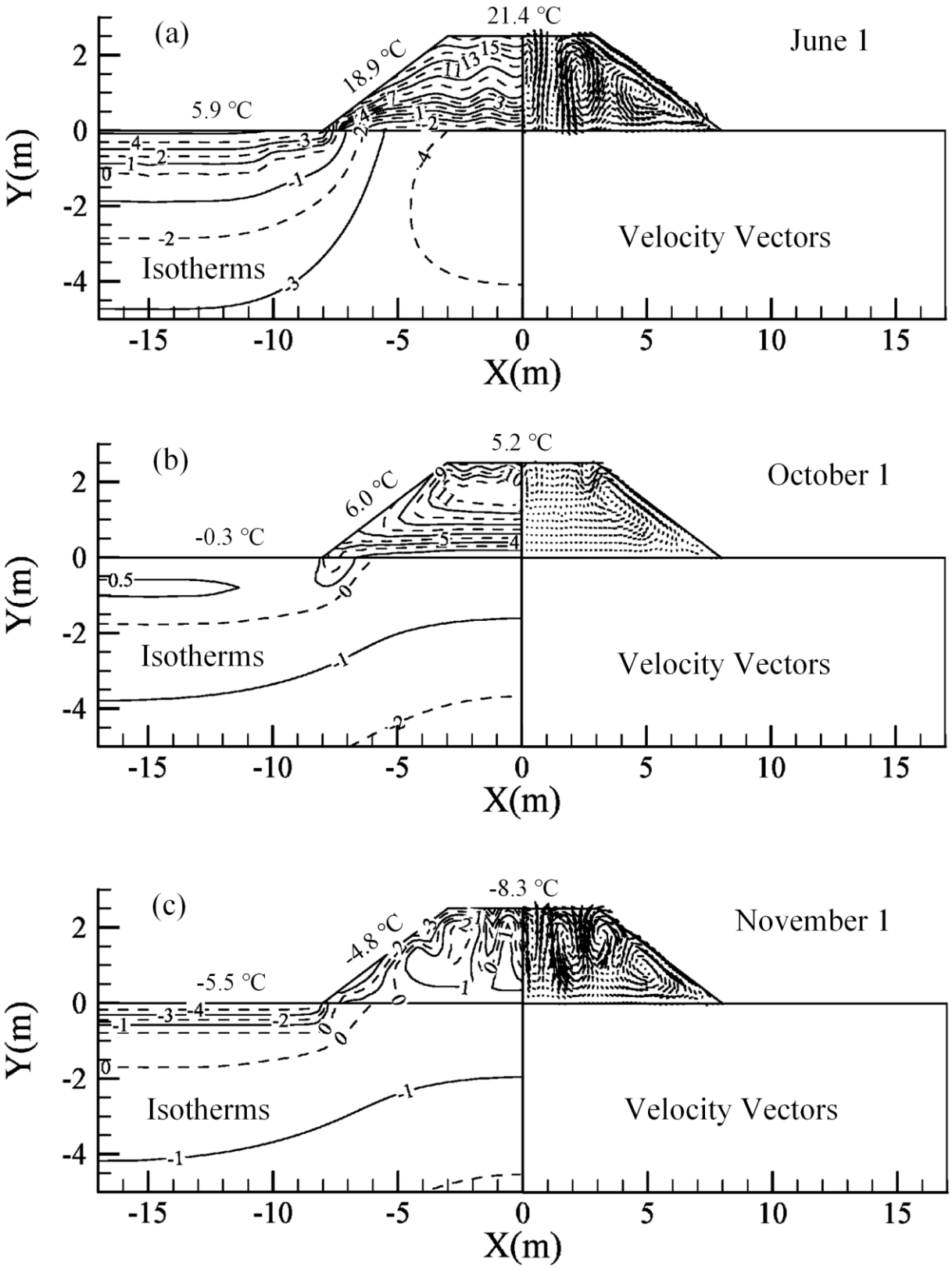
(a)
June 1
21.4 °C
18.9 °C
5.9 °C
Isotherms
Velocity Vectors
Y(m)
X(m)
(b)
October 1
5.2 °C
6.0 °C
-0.3 °C
Isotherms
Velocity Vectors
Y(m)
X(m)
(c)
November 1
-8.3 °C
-4.8 °C
-5.5 °C
Isotherms
Velocity Vectors
Y(m)
X(m)

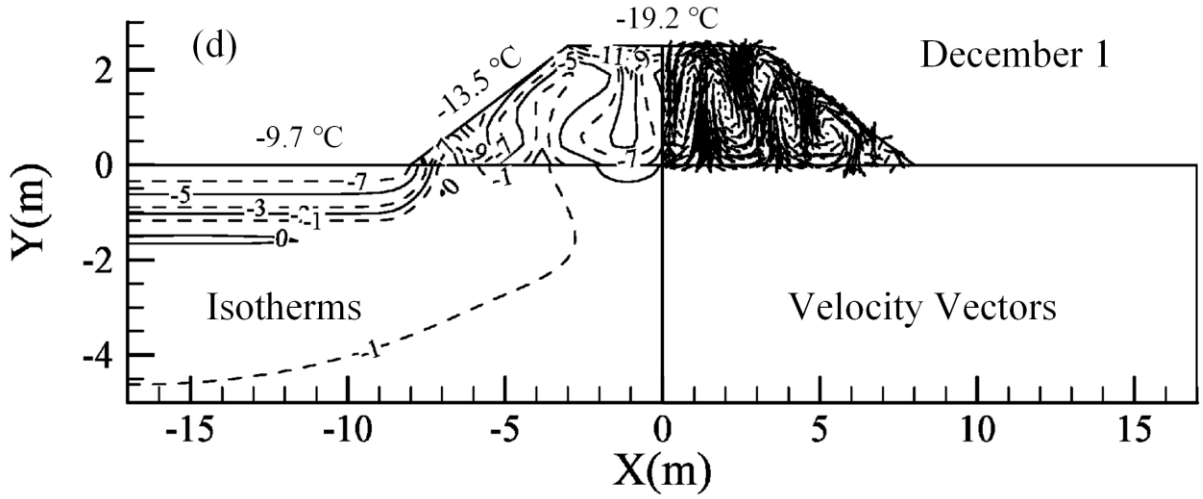
(d)
December 1
-19.2 °C
-13.5 °C
-9.7 °C
Isotherms
Velocity Vectors
Y(m)
X(m)

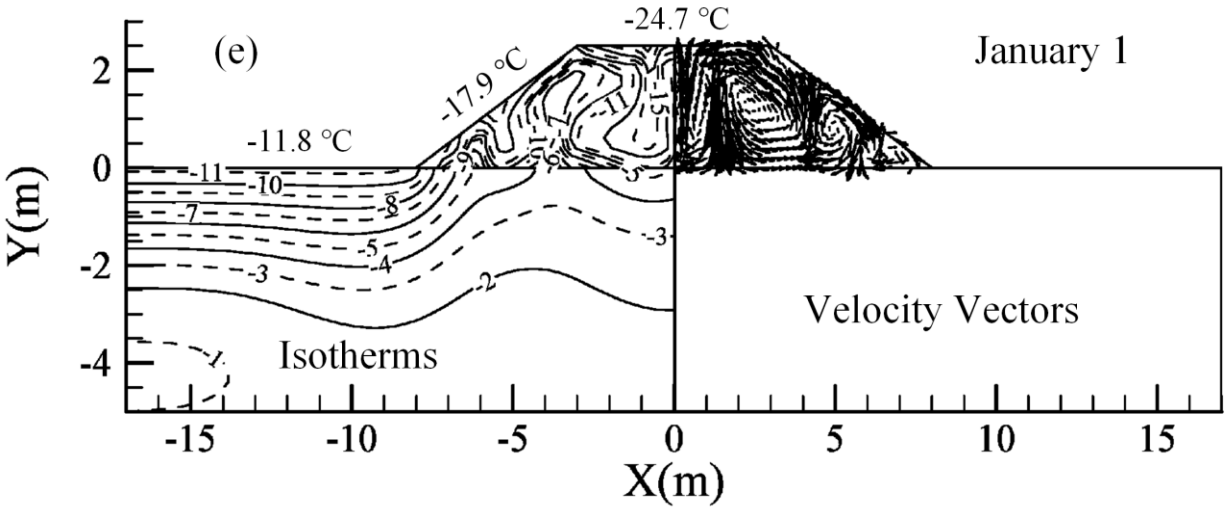
(e)
January 1
-24.7 °C
-17.9 °C
-11.8 °C
Isotherms
Velocity Vectors
Y(m)
X(m)

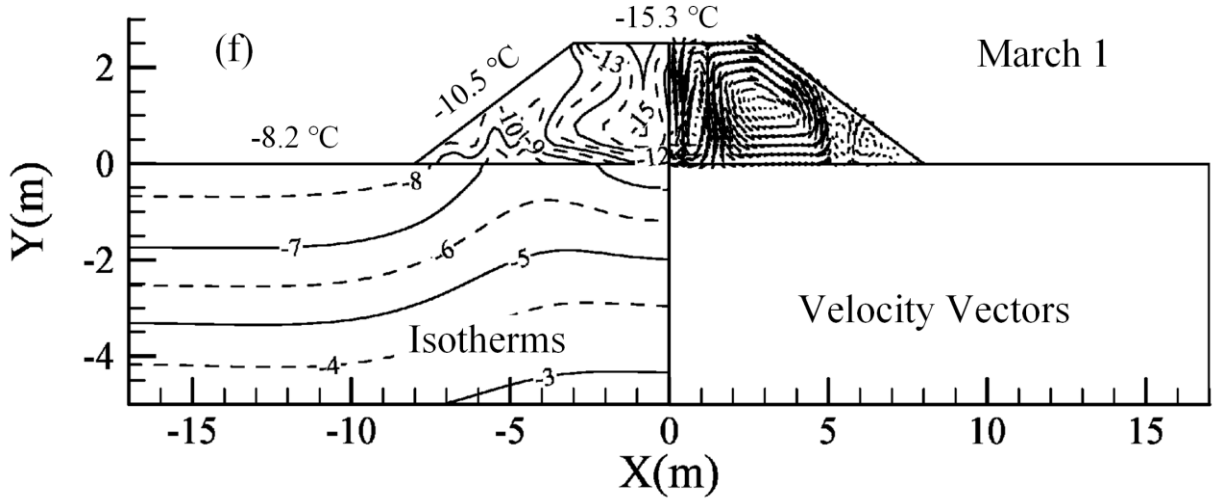
(f)
March 1
-15.3 °C
-10.5 °C
-8.2 °C
Isotherms
Velocity Vectors
Y(m)
X(m)

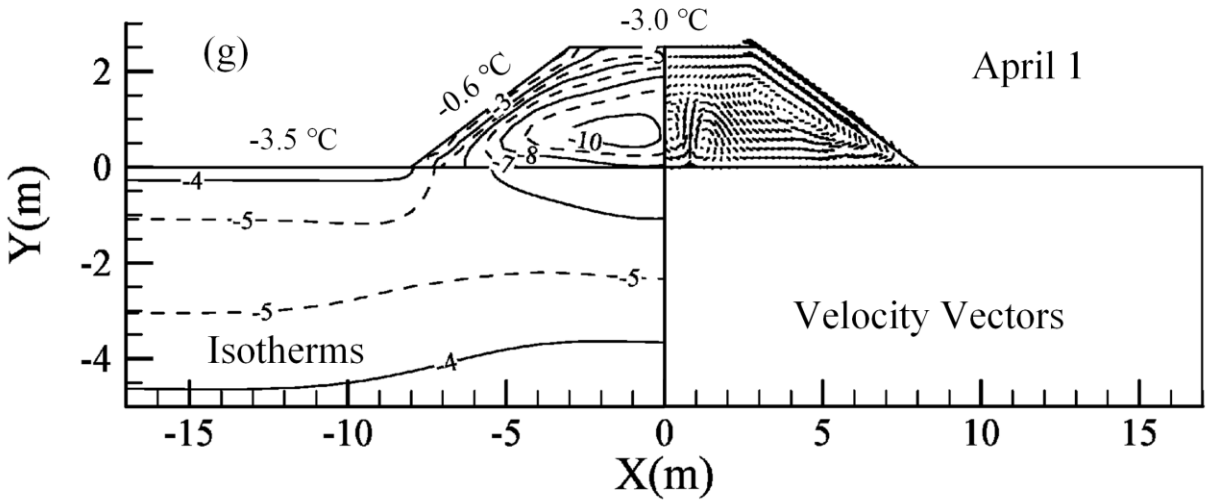


**Figure 4.5** Instantaneous isotherms (℃) and velocity vectors for Case 3, the cellular concrete embankment. (a) June 1. (b) October 1. (c) November 1. (d) December 1. (e) January 1. (f) March 1. (g) April 1.

### 4.4 Comparison and Discussion

Previous studies show that natural convection in porous embankment has a significant influence on the heat transfer pattern and thermal performance of the embankment. The comparison results of the instantaneous isotherms of Case 1, 2 and 3 on January 1, April 1, July 1, and October 1 indicated that the annual thermal effect of the proposed cellular concrete ACE was much better than that of sand/gravel embankment and crushed-rock ACE.

Figures 4.6a-d show the instantaneous isotherms of cellular concrete ACE and sand/gravel embankment. The left half and right half of the plot represent the isotherms of the cellular concrete ACE and sand/gravel embankment, respectively. The sand/gravel embankment is impermeable. Thus, the thermal pattern is the conduction only. Compared the instantaneous isotherms of Case 1 with Case 3 on January 1, April 1, July 1, and October 1, the temperature

beneath the embankment of cellular concrete is much lower than that of sand/gravel embankment in all the four months. The cooling performance of cellular concrete ACE is overwhelmingly better than that of conventional sand/gravel embankment.

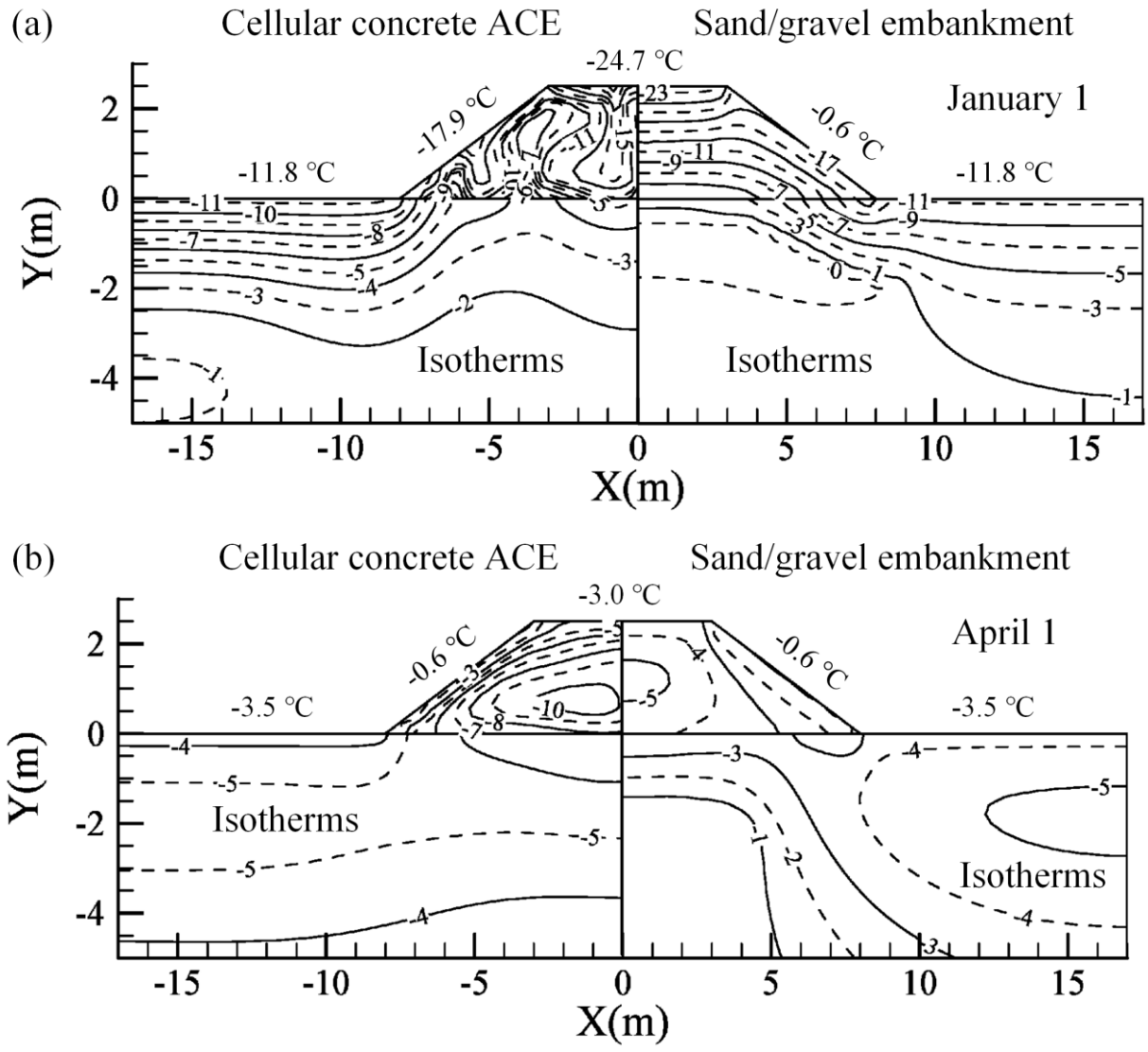

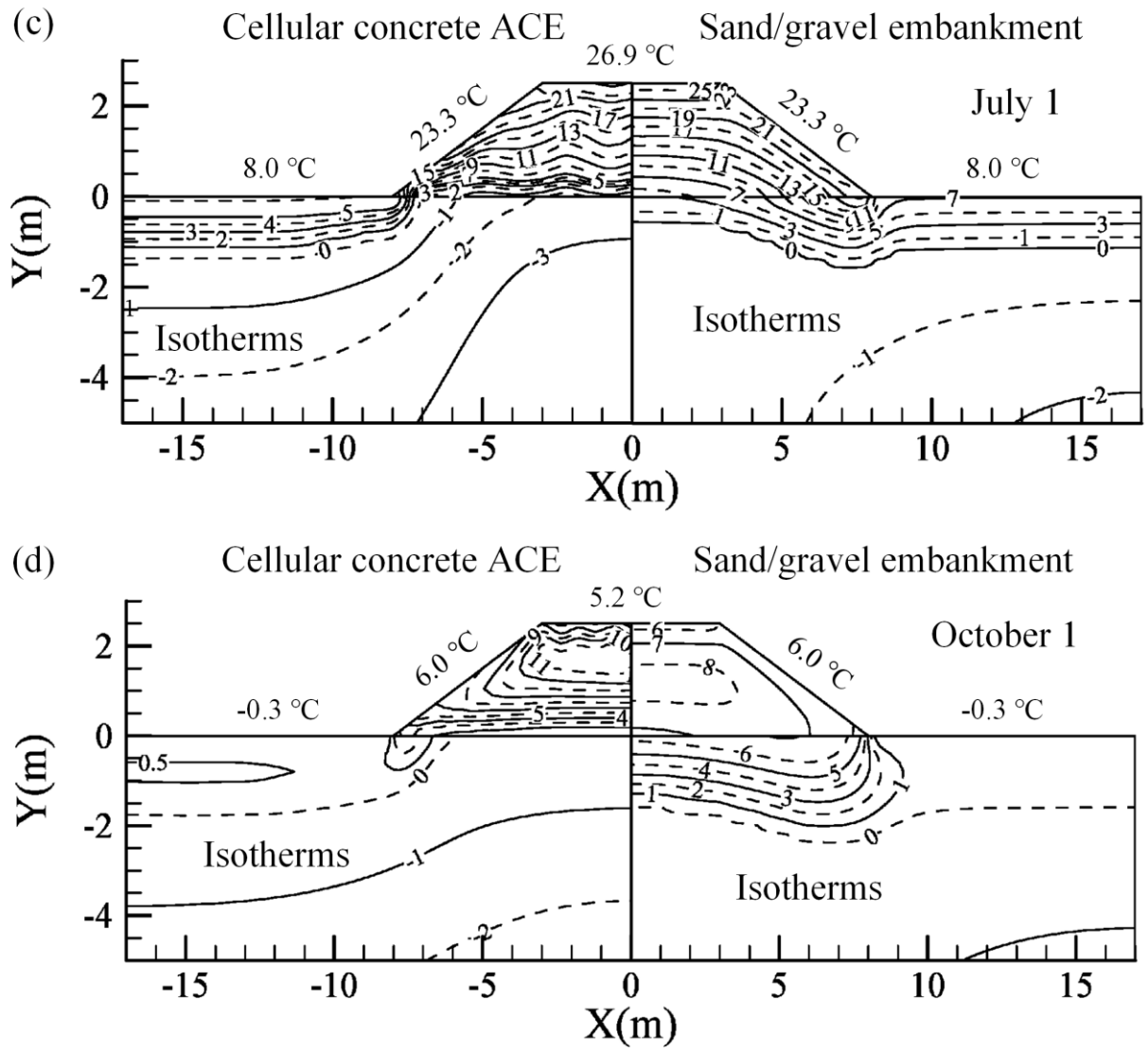


**Figure 4.6** Comparison of the instantaneous isotherms (℃) of Cases 1 and 3. (a) January 1. (b) April 1. (c) July 1. (d) October 1.

Figures 4.7a-d display the instantaneous isotherms of cellular concrete ACE and crushed-rock ACE. The left half and right half of the plot represent the isotherms of the cellular concrete ACE and crushed-rock ACE, respectively. Figure 4.7a shows that the temperature beneath the crushed-rock ACE was lower than that at the same depth of cellular concrete ACE. The reason is that the heat transfer contributed by the natural convection is almost the same. However, crushed

rock has a higher value of thermal conductivity, which means the thermal conductive effect of crushed rocks is much stronger than that of cellular concrete. Thus, the overall cooling effect of the crushed-rock embankment is better than that of cellular concrete in winter. The entire permafrost layer beneath the two embankments remained frozen, and the temperature was lower than $-3℃$.

On April 1, the temperatures on outside boundaries of the embankment and the native ground surface began to increase (Figure 4.7b). A thermal center generated in the embankments of the two cases. At this time of the year, the cellular concrete shows a better thermal insulation effect than that of crushed-rock, the difference of the temperature at the same depth beneath the cellular concrete ACE and the crushed-rock ACE became less obvious.

On July 1, Figure 4.7c shows a typical thermal pattern occurring in ACE during summer. The upper half of the embankment was thawed, but the lower half of the embankment stayed frozen. The majority of the permafrost layer under the embankment remains frozen, except for the toe of the embankment. The temperature beneath the embankment of Case 3 is much lower than that of Case 2. At the embankment-foundation interface, the temperature of Case 3 is $1℃$ lower than that of Case 2. The cellular concrete showed a much better thermal performance than that of crushed-rock due to its better insulation property.

Figure 4.7d displays that, on October 1, the surface temperatures of the two embankments and native ground decreased again. A thermal center regenerated in the embankments of the two cases. The density gradient in the embankment-triggered air motion in the embankment and sped

up the heat transfer in the embankment. The foundation soil beneath the crushed-rock embankment started thawing, and the 0℃ isotherm moved a little bit below the interface. However, the foundation soil beneath the cellular concrete embankment was still frozen.

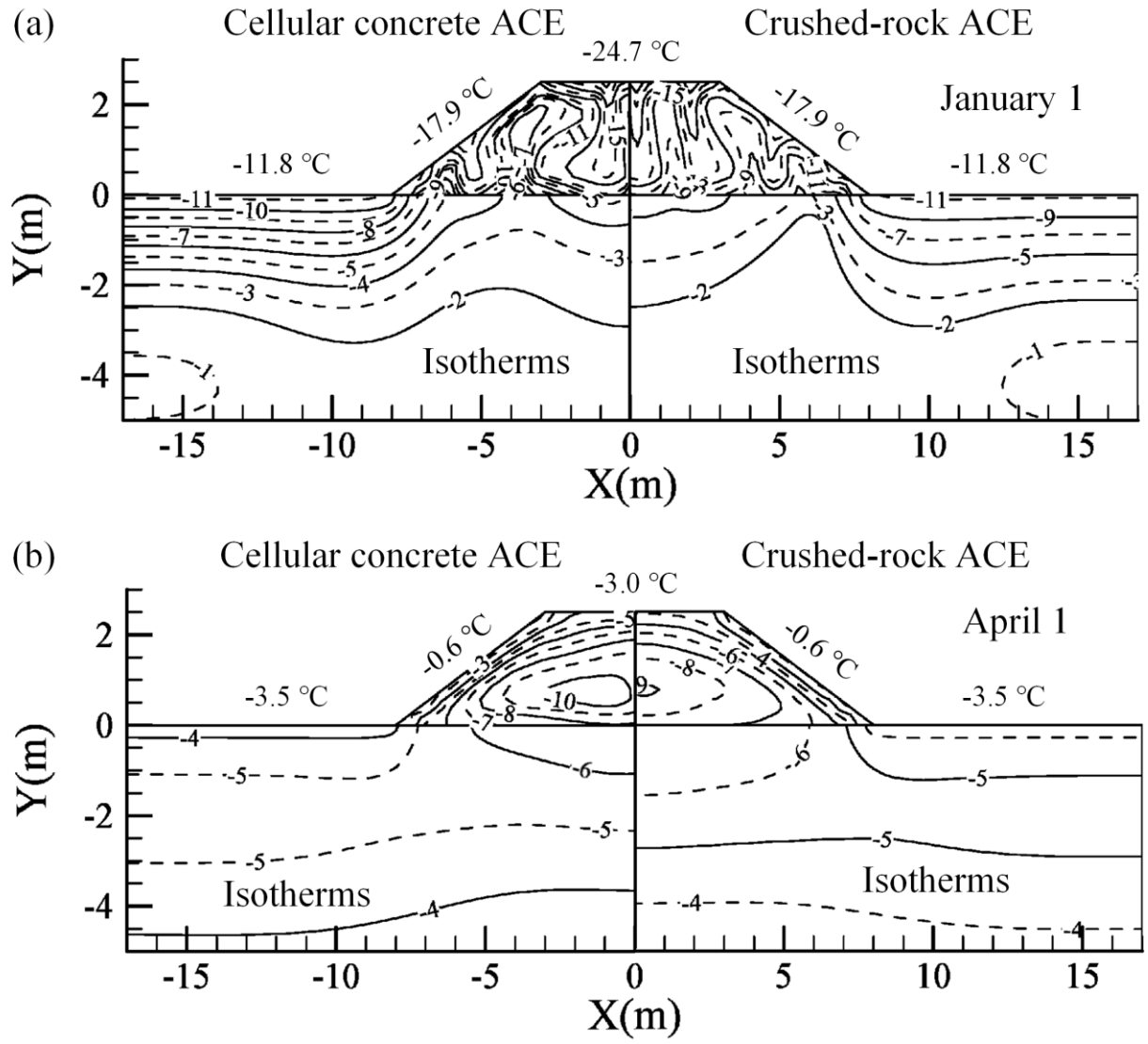

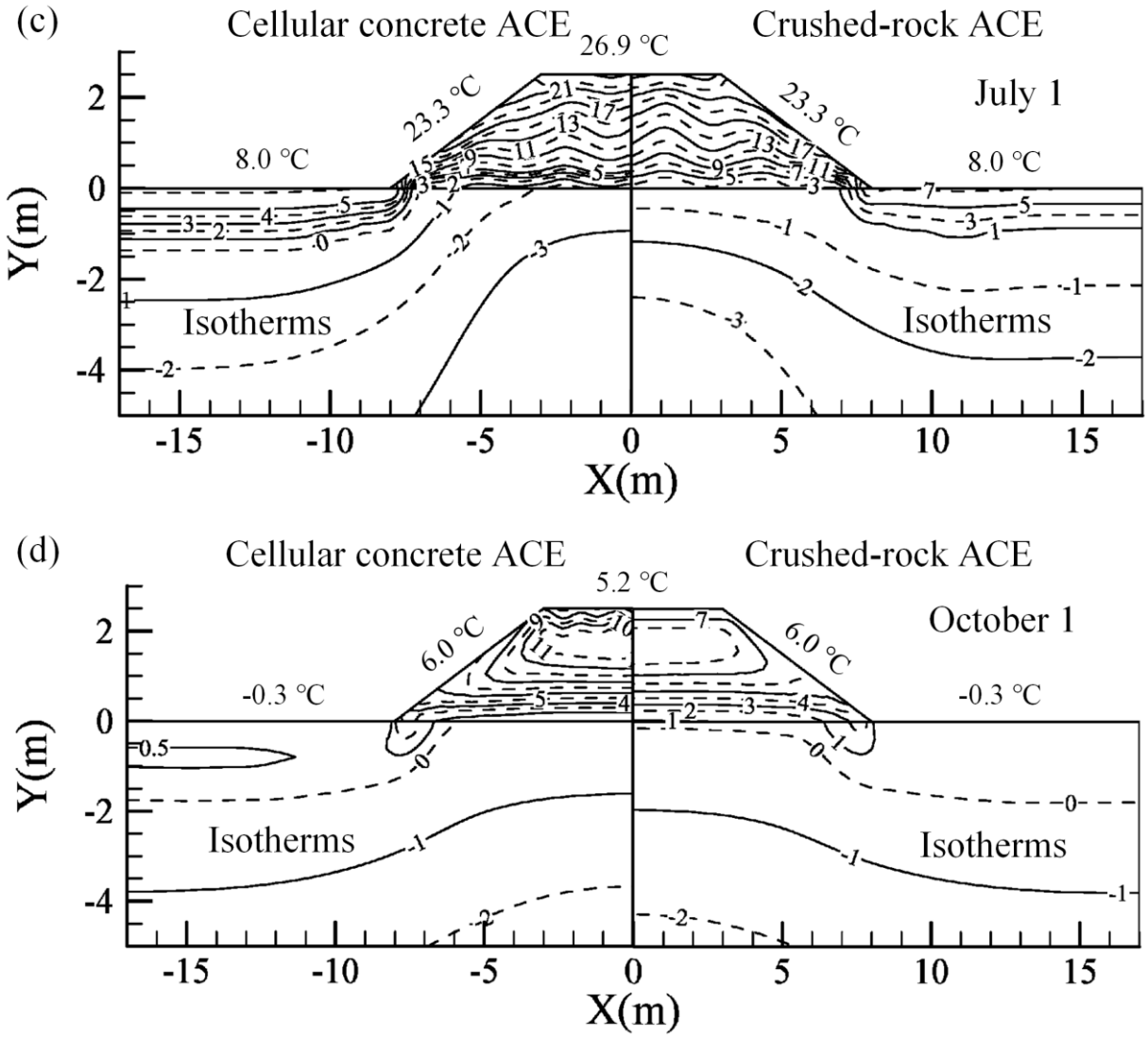


**Figure 4.7** Comparison of the instantaneous isotherms (℃) of Cases 2 and 3. (a) January 1. (b) April 1. (c) July 1. (d) October 1.

Table 4.3 evaluated the thermal performance of the embankments for Cases 1, 2 and 3. The thermal performance is qualitatively divided into three levels: Lowest, Moderate, and Highest. The temperatures at the embankment-foundation interface were considered as indicators; the lower the temperature, the better will be the cooling performance of the embankment. By analyzing the data of the 12 months in the 10th year, the cooling performance

level of the embankments was summarized in Table 4.3. As observed, the thermal performance of Cases 2 and 3 are overwhelmingly better than that of Case 1. From February 1 to April 1, the performance of crushed-rock ACE is much better than that of cellular concrete ACE, however, from May 1 to December 1, and January 1, the performance of the cellular concrete ACE is better than that of crushed-rock ACE. Considering the annually thermal performance, the proposed cellular concrete ACE outperformed crushed-rock embankment.

**Table 4.3** Thermal performance of the embankments for Cases 1, 2 and 3.

| Month | Interface temperature | | |
|---|---|---|---|
| | Case 1 | Case 2 | Case 3 |
| Jan. | Highest | Moderate | Lowest |
| Feb. | Highest | Lowest | Moderate |
| Mar. | Highest | Lowest | Moderate |
| Apr. | Highest | Lowest | Moderate |
| May. | Highest | Moderate | Lowest |
| Jun. | Highest | Moderate | Lowest |
| Jul. | Highest | Moderate | Lowest |
| Aug. | Highest | Moderate | Lowest |
| Sep. | Highest | Moderate | Lowest |
| Oct. | Highest | Moderate | Lowest |
| Nov. | Highest | Moderate | Lowest |
| Dec. | Highest | Moderate | Lowest |

Note: Take temperatures at the embankment-foundation interface as indicators, the lower the temperature, the better for the cooling performance of the embankment.

An evaluation of the thermal influence that an embankment will have on the permafrost layer beneath it can be obtained by analyzing the temperatures at the interface of the embankment and the foundation soil. Figure 4.8 shows the yearly average, yearly minimum and yearly maximum temperature at the embankment-foundation interface for Cases 1, 2 and 3,

respectively. The critical temperatures are plotted as a function of distance from the centerline of the numerical model.

As was shown in Figure 4.8a, the annual average temperature near the centerline of the embankment increased by approximately 4℃, compared to the results of Case 2 and Case 3 (Figures 4.8b-c). The value of the annual average temperature at the centerline is 0.85℃, which is close to the boundary temperatures of 1.1℃, 2.7℃, and −1.9℃. The results indicates that the summer ambient temperature and the ambient winter temperature would have an equal effect on the embankment and the permafrost layer. For Case 1, the range of temperature at the centerline is about −6.5℃ to 8.5℃. Compared to Cases 2 and 3, the range of the temperature of Case 1 at the centerline is much more extensive, which indicated that the ambient temperature has a greater influence on the embankment of Case 1 than that of the other two cases. The same phenomenon can be observed from temperatures at the toe of the embankment.

Figures 4.8b-c show that the annual average temperature at the interface between the embankment and the permafrost layer is approximately −5℃ to −3℃, except the toe of the embankment. The critical temperatures mentioned above are much lower than that of Case 1 in Figure 4.8a. For Case 1, the annual maximum temperature at the centerline of the embankment is 8.4℃, and the minimum temperature is −6.4℃. For Case 2, the maximum yearly temperature at the centerline of the embankment is 0.3℃, and the minimum temperature is −9.1℃. For Case 3, the annual maximum temperature at the centerline of the embankment is −0.1℃, and the minimum temperature is −7.8℃ (Figure 4.8). The natural convection in ACE during winter will

enhance the cooling effect of the ambient temperature to the permafrost layer. Thus, the thermal patterns of ACE are convection and conduction, which result in the annual average temperatures of Cases 2 and 3 being much lower than that of Case 3.

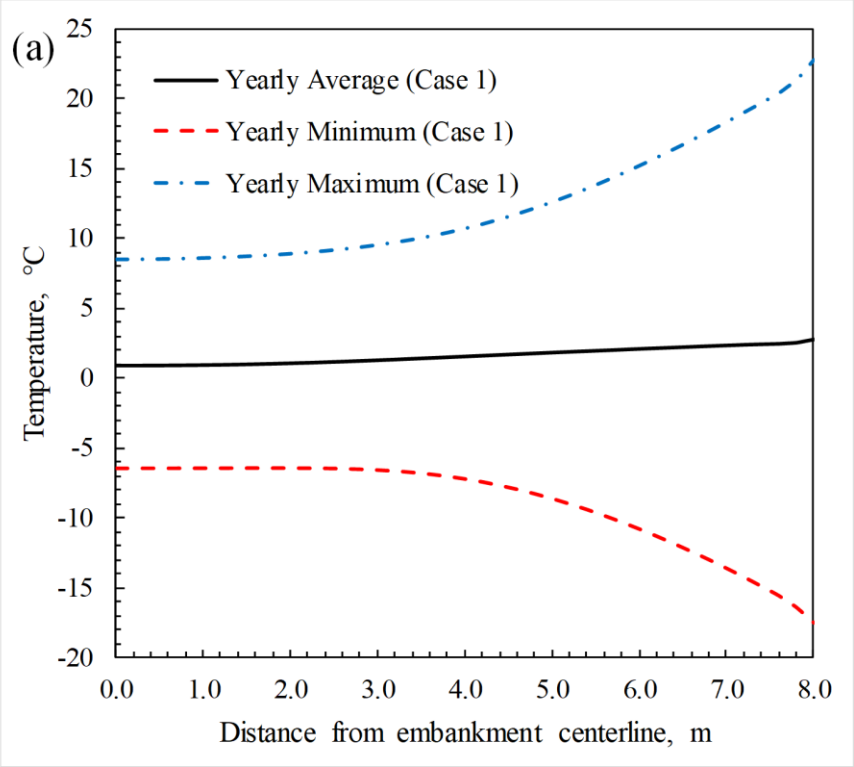

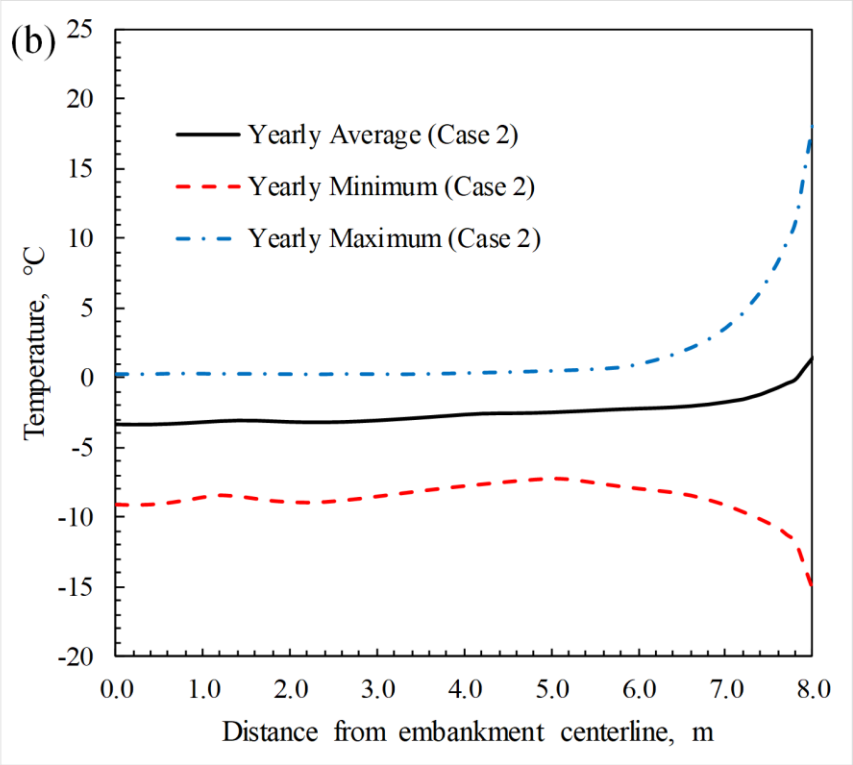
(b)
Yearly Average (Case 2)
Yearly Minimum (Case 2)
Yearly Maximum (Case 2)
Temperature, °C
25
20
15
10
5
0
-5
-10
-15
-20
0.0
1.0
2.0
3.0
4.0
5.0
6.0
7.0
8.0
Distance from embankment centerline, m

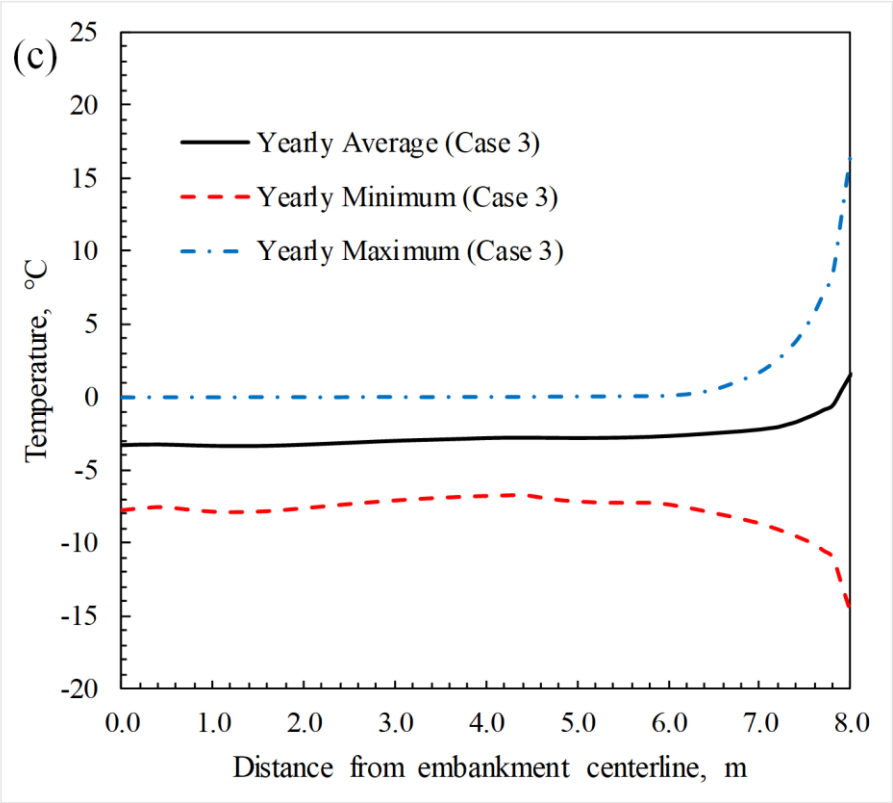


**Figure 4.8** Temperatures at the embankment-foundation interface (℃). (a) Case 1, the sand/gravel embankment. (b) Case 2, the crushed rock embankment. (c) Case 3, the cellular concrete embankment.

Figure 4.9 displays the yearly maximum temperature of the embankment-foundation interface for Cases 1, 2 and 3. As observed, the yearly maximum temperature of cellular concrete ACE and crushed rock ACE are much lower than that of the sand/gravel embankment, which indicated that the cooling performance of ACE is overwhelmingly better than that of conventional sand/gravel embankment. The interface temperature for the crushed-rock embankment, except for the toes of the embankment, is 0℃ or higher, which means that the interface was in thawing stage. The thawing of the permafrost layer had a negative influence on the stability of the roadway structure. The interface temperature for the cellular concrete

embankment, except for the toes of the embankment, is 0℃ or lower, which means that the interface was in the frozen state all the year round. Therefore, even the yearly maximum temperature of cellular concrete ACE is a little bit lower than that of crushed rock ACE, the cooling performance of cellular concrete ACE is much better than that of crushed-rock ACE.

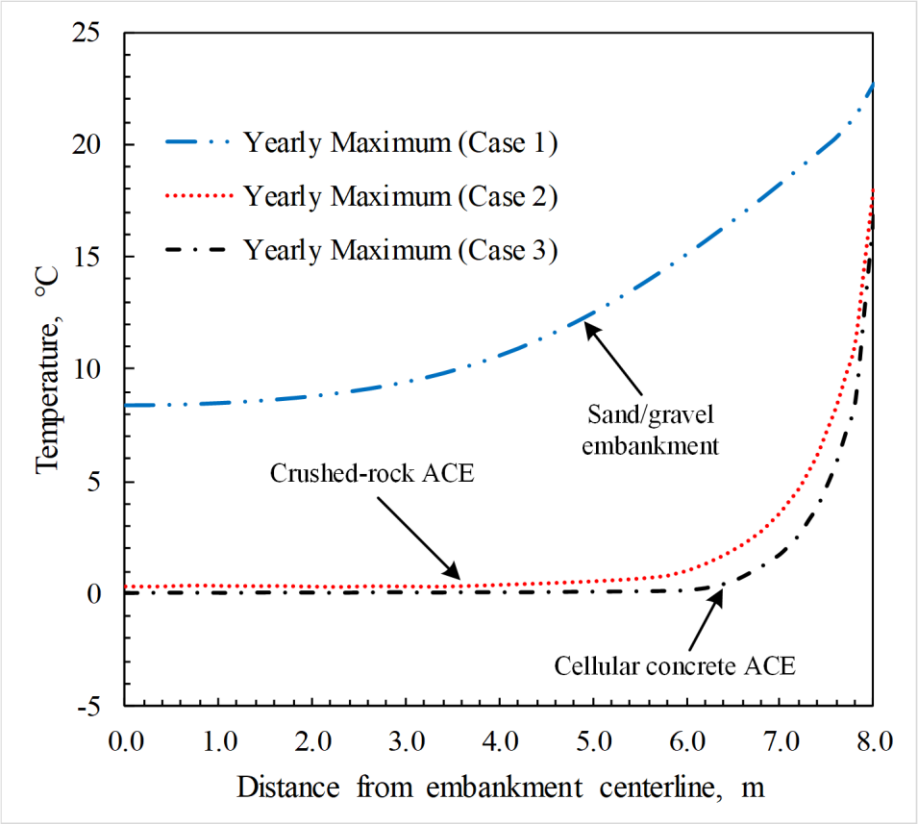


**Figure 4.9** Comparison of the yearly maximum temperatures at the embankment-foundation interfaces (℃) for Cases 1, 2 and 3.

# CHAPTER 5.0 COSTS ANALYSES

Saboundjian (2008) and Ferrell (2009) investigated the costs associated with techniques to stabilize the roadway embankment independently. Sabounjian (2008) focused on lightweight fill materials considering roadbed construction practice on permafrost foundations in Alaska. The author provided an estimation of the costs per unit volume which are assumed to be in 2008 U.S. dollars (Regehr et al., 2013). Ferrell (2009) investigated the railway embankment construction on permafrost regions. The cost estimation is provided based on discussions with industry representatives, product information, and necessary assumptions. The costs estimations are provided for North American and are assumed to be in 2009 U.S. dollars.

The cost estimations of the three cases are provided in the study to investigate further the feasibility of using cellular concrete as an alternative material for ACE practices. Table 5.1 provides details on the cost estimations for the proposed cellular concrete ACE, crushed-rock ACE, and silty sand/gravel embankment in this study, respectively, referring to the cost estimations from Saboundjian (2008) and Ferrell (2009).

As observed in Table 5.1, the per kilometer cost of the cellular concrete ACE is the same as or approximately 30% higher than that of conventional sand/gravel embankment with using the locally available materials. However, as discussed above, the cooling effect of cellular concrete ACE is overwhelmingly better than that of the conventional sand/gravel embankment.

The per kilometer cost of the crushed-rock embankment is about $3,575,000 without considering the shipping cost (Table 5.1), which is approximately 37% to 136% higher than that of cellular concrete ACE. Moreover, in many areas of interior Alaska, the coarse gravel or crushed rocks needed for ACE construction are not readily available. Replacement fill shipped from a remote location to a construction project in western Alaska can cost 10 to 12 times more (Saboundjian, 2008). Burdened by the need to ship suitable rock to remote locations, costs for constructing a crushed-rock ACE is often prohibitively high, which prevents its wide use in Alaska. However, cellular concrete's primary advantages are minimal construction labor and reasonable shipping costs for materials which provides an excellent solution to this issue (Saboundjian, 2008).

**Table 5.1** Estimated costs for the sand/gravel embankment and the ACEs.

| Technique | Unit Cost Estimate (USD) | Cost per km (USD) |
|---|---|---|
| Silty sand/gravel embankment | Unit price: 60-75$/$m^3$ (locally available in the Yukon-Kuskokwim Delta)[a] | Total: Approximately $1,650,000 to $2,062,500 |
| Crushed-rock ACE | Unit price: $50/ton=130$/$m^3$ (placement included, with the density of 2600kg/$m^3$)[b]<br>Shipping fee: 10 to 12 times more than if suitable local material were available[a]. | Materials & placement: $3,575,000<br>Shipping fee: $35,750,000<br>Total: Approximately $39,325,000 |
| Cellular concrete ACE | Unit price: $55-$95/$m^3$ (without sand or aggregate, locally available)[a] | Total: Approximately $1,512,500 to $2,612,500 |

[a]Source: Saboundjian (2008)

[b]Source: Ferrell (2009)

Even the shipping cost, extra labor, and equipment expenses vary for different regions, and climate conditions, and these factors are not fully considered in this study. The rough estimation is still strongly proof that cellular concrete as an environmentally friendly and cost-effective material shows excellent potential to provide a better roadway embankment solution on permafrost foundations in Alaska.

# CHAPTER 6.0 CONCLUSIONS AND RECOMMENDATIONS

A series of lab tests on cellular concrete combinations of cement, fly ash, slag and foaming agent with different volumetric foaming percentages were conducted to investigate the properties of cellular concrete. The effects of those design factors on the setting time, flowability, and compressive strength of pastes were investigated to determine the optimum paste design. The workability, thermal conductivity, and concrete density and compressive strength were evaluated to finalize the optimum mix design of cellular concrete. The results show that the cellular concrete has great thermal insulation properties and sufficient compressive strength for the embankment, therefore cellular concrete has great potential as an alternative material for ACE construction in cold regions.

The thermal characteristics of the conventional sand/gravel embankment, crushed-rock embankment, and the proposed cellular concrete embankment were analyzed using a numerical simulation method. The analysis focused on the heat transfer pattern and thermal performance of the embankments for Case 1, Case 2, and Case 3. The critical temperatures, the isotherms, and the velocity vectors of the embankment and permafrost layer have been investigated in detail.

The results of the study show that heat from the bottom of cellular concrete mass can be efficiently removed in winter, but little is removed during the warm season. That is to say, cellular concrete ACE performed as an excellent cooling agent in cold seasons, and in warm-season, it provides an excellent thermal insulation resistance to prevent heat transfer from the

ambient environment to the permafrost layer. Consider the annual net cooling effectiveness; thawing is prevented by effective cooling of ACE, the temperature of the underground layer decreased and associated with stabilizing the foundation soil in permafrost regions.

The cooling effect of cellular concrete ACE and crushed-rock ACE is overwhelmingly better than that of conventional sand/gravel embankment. In cold seasons, the natural convection in the embankment made a considerable contribution to the heat transfer efficiency of ACE. In short winter times, the passive cooling performance of crushed-rock ACE is a little bit better than the proposed cellular concrete ACE due to the higher thermal conductivity of crushed rocks. However, for the majority of the months, the temperature beneath the cellular concrete ACE is much lower than that of crushed-rock ACE. For the annual thermal performance, there is no doubt that the proposed cellular concrete ACE is much better than that of the crushed-rock embankment.

The only difference between cellular concrete ACE and crushed-rock ACE is the thermal properties. The better performance of cellular concrete ACE indicated that the thermal conductivity and specific heat capacity of the construction materials has a significant impact on the thermal performance of ACE.

In this study, the authors roughly estimated the per kilometer costs of the cellular concrete ACE, the crushed-rock ACE, and the sand/gravel embankment in Alaska. The economic benefits of cellular concrete ACE are significantly higher than that of ordinary crushed-rock ACE and the sand/gravel embankment. Cellular concrete as an alternative material

for ACE in permafrost regions showed great potential for higher performance and reduction of the high cost of embankment construction in the permafrost region.

## REFERENCES


Akulov, K. A., Petryakov, V. A., Mostovaya, N. and A. (2017). “The Use of Foamed Concrete for Oil Spill Treatment and Carbon Capture.” IOP Conference Series: Earth and Environmental Science, 50, 012042.

Amran, Y. H. M., Farzadnia, N., Amran, M., and Ali, A. A. A. (2015). “Properties and applications of foamed concrete; a review.” Construction and Building Materials, 101. 990-1005.

ASTM C109. (2013). Standard Test Method for Compressive Strength of Hydraulic Cement Mortars (Using 2-in. or [50-mm] Cube Specimens).

ASTM, C1107. (2019). Standard Specification for Packaged Dry. Hydraulic-Cement Grout (Nonshrink).

ASTM, C1437. (2007). Standard test method for flow of hydraulic cement mortar.

ASTM C191. (2019). Standard test methods for time of setting of hydraulic cement by vicat needle.

ASTM C192/C192M. (2012). Standard practice for making and curing concrete test specimens in the laboratory.

ASTM C39. (2010). Standard test method for compressive strength of cylindrical concrete specimens.

ASTM C495. (2012). Standard Test Method for Compressive Strength of Lightweight Insulating Concrete.

Barbhuiya, S. A., Gbagbo, J. K., Russell, M. I., and Basheer, P. A. M. (2009). “Properties of fly ash concrete modified with hydrated lime and silica fume.” Construction and Building Materials, 23(10), 3233-3239.

Bihina, G., Zhao, B., and Bouchaïr, A. (2013). “Behaviour of composite steel–concrete cellular beams in fire.” Engineering Structures, 56(6), 2217-2228.

Biondini, F., and Nero, A. (2011). “A cellular finite beam element for nonlinear analysis of concrete structures under fire.” Journal of Structural Engineering, 137(5), 543-558.

Cai, J., Lu, Z., Hou, G., Bai, R., and Liu, M. (2011). “Application of Magnetite Mill Tailings and Solvay Distiller Waste in Foamed Concrete in Situ.” International Conference on Materials and Products Manufacturing, 335, 1312-1315.

Chen, B., Wu, Z., and Liu, N. (2012). “Experimental research on properties of high-strength foamed concrete.” Journal of Materials in Civil Engineering, 24(1), 113-118.

Choi, J. Y., Lee, H. S., and Lee, B. K. (2007). “An experimental study on the development of structural lightweight concrete using micro foam agents.” Key Engineering Materials, 348-349(a1), 469-472.

Decký, M., Drusa, M., Zgútová, K., Blaško, M., Hájek, M., and Scherfel, W. (2016). “Foam concrete as new material in road constructions.” Procedia Engineering, 161, 428-433.

Dong, Y., Pei, W., Liu, G., Jin, L., and Chen, D. (2014). “In-situ experimental and numerical investigation on the cooling effect of a multi-lane embankment with combined crushed-rock interlayer and ventilated ducts in permafrost regions.” Cold Regions Science and Technology, 104, 97-105.

Ferrell, S. M. (2009). Maintaining stability beneath cold region transportation infrastructure with special emphasis on railroads (M.Sc. thesis, Michigan Technological University), Houghton, MI.

Ferrians, O. J. (1994). Permafrost in Alaska. The Geology of North America, 1, 845-854.

Fluent ANSYS. (2019a). ANSYS fluent theory guide 19.1. ANSYS, Canonsburg, PA.

Fluent ANSYS. (2019b). ANSYS fluent user's guide 19.1. ANSYS, Canonsburg, PA.

Gerasimovich, B. M., Stsnislavovna, G. L., and Victorovna, K. D. (2014). "Variable density cellular concrete." Advanced Materials Research, 860-863, 1323-1326.

Goering, D. J., and Kumar, P. (1996). "Winter-time convection in open-graded embankments." Cold Regions Science and Technology, 24(1), 57-74.

Goering, D. J. (1997). Air Convection Embankment Experimental Feature Design–Phase I (No. AK-RD-97-02, INE/TRC 97.06, SPR-95-08, Interim Rept). Alaska. Dept. of Transportation and Public Facilities.

Goering, D. J. (1998). "Experimental investigation of air convection embankments for permafrost-resistant roadway design." Seventh International Conference on Permafrost. 319-326.

Goering, D. J. (2001). Parks/Chena ridge air convection embankment experimental feature-phase II final report (No. FHWA-AK-RD-01-02). Alaska. Dept. of Transportation and Public Facilities.

Goering, D. J. (2003). "Thermal response of air convection embankments to ambient temperature fluctuations." Proceedings of the Eighth International Conference on Permafrost, Zurich, Switzerland, 1, 291-296.

Hu, H. (2013). “On the application of anti-seismic & waste-recyclable foamed concrete cast-in-place wall in architecture.” Advanced Materials Research, 671-674, 1524-1527.

Jones, M. R., and Mccarthy, A. (2005). “Preliminary views on the potential of foamed concrete as a structural material.” Magazine of Concrete Research, 57(1), 21-31.

Jones, M. R., and Mccarthy, A. (2006). “Heat of hydration in foamed concrete: effect of mix constituents and plastic density.” Cement and Concrete Research, 36(6), 1032-1041.

Jones, M. R., Ozlutas, K., and Zheng, L. (2017). “High-volume, ultra-low-density fly ash foamed concrete.” Magazine of Concrete Research, 69(22), 1146-1156.

Kadela, M., Kozłowski, M., and Kukiełka, A. (2017). “Application of foamed concrete in road pavement – weak soil system.” Procedia Engineering, 193, 439-446.

Kashani, A., Ngo, T. D., Mendis, P., Black, J. R., and Hajimohammadi, A. (2017). “A sustainable application of recycled tyre crumbs as insulator in lightweight cellular concrete.” Journal of Cleaner Production, 149, 925-935.

Kearsley, E. P., and Wainwright, P. J. (2001). “Porosity and permeability of foamed concrete.” Cement and Concrete Research, 31(5), 805-812.

Krämer, C., Schauerte, M., Kowald, T. L., and Trettin, R. H. F. (2015). “Three-phase-foams for foam concrete application.” Materials Characterization, 102, 173-179.

Krämer, C., Schauerte, M., Müller, T., Gebhard, S., and Trettin, R. (2017). “Application of reinforced three-phase-foams in UHPC foam concrete.” Construction and Building Materials, 131, 746-757.

Krivenko, P., and Kovalchuk, G. (2014). “Achieving a heat resistance of cellular concrete based on alkali activated fly ash cements.” Materials and Structures, 48(3), 1-8.

Kuzielová, E., Pach, L., and Palou, M. (2016). “Effect of activated foaming agent on the foam concrete properties.” Construction and Building Materials, 125, 998-1004.

Lamond, J., and Pielert, J. (2006). Significance of Tests and Properties of Concrete and Concrete-making Materials, Chapter 47, Cellular Concrete, ASTM Special Technical Publication, ASTM, West Conshohocken, PA.

Lai, Y., Ma, W., Zhang, M., Yu, W., and Gao, Z. (2006). “Experimental investigation on influence of boundary conditions on cooling effect and mechanism of crushed-rock layers.” Cold Regions Science and Technology, 45(2), 114-121.

Li, G. Y., Mu, Y. H., and Zhang, X. (2009). “Thermal characteristics of the embankment with crushed rock side slope to mitigate thaw settlement hazards of the Qinghai-Tibet railway.” Acta Geologica Sinica-English Edition, 83(5), 1000-1007.

Lin, D., Zhao, Q., Hou, G., Zhao, J., and Han, J. (2013). “Preparation of novel foaming agent and its application in foam concrete.” Advanced Materials Research, 785-786, 305-307.

Liu, C., Zhang, Y., Yang, H., Ren, X., and Yang, J. (2011). “Dodecanamide concrete foaming agent: preparation and application.” Applied Mechanics and Materials, 71-78, 799-802.

Liu, M. Y. J., Alengaram, U. J., Jumaat, M. Z., and Mo, K. H. (2014). “Evaluation of thermal conductivity, mechanical and transport properties of lightweight aggregate foamed geopolymer concrete.” Energy and Buildings, 72, 238-245.

Liu, M. Y. J., Alengaram, U. J., Santhanam, M., Jumaat, M. Z., and Mo, K. H. (2016). “Microstructural investigations of palm oil fuel ash and fly ash based binders in lightweight aggregate foamed geopolymer concrete.” Construction and Building Materials, 120, 112-122.

Liu, M. H., Li, G. Y., Niu, F. J., Lin, Z. J., and Shang, Y. H. (2017). “Porosity of crushed rock layer and its impact on thermal regime of Qinghai−Tibet railway embankment.” Journal of Central South University, 24(4), 977-987.

Liu, Z., Zhao, K., Hu, C., and Tang, Y. (2016a). “Effect of water-cement ratio on pore structure and strength of foam concrete.” Advances in Materials Science and Engineering, 2016(11), 1-9.

Long, W. W., and Wang, J. S. (2015). “Study on Compressive Strength and Moisture Content of Different Grades Density of Foam Concrete.” International Conference on Material Science and Applications, 3, 167-172.

Ma, W., Shi, C. H., Wu, Q. B., Zhang, L. X., and Wu, Z. J. (2006). “Monitoring study on technology of the cooling roadbed in permafrost region of Qinghai–Tibet Plateau.” Cold Regions Science and Technology, 44(1), 1-11.

Ma, Q., Lai, Y., Zhang, M., and You, Z. (2017). “Model test study on the anti-saline effect of the crushed-rock embankment with impermeable geotextile in frozen saline soil regions.” Cold Regions Science and Technology, 141, 86-96.

Miled, K., and Limam, O. (2016). “Effective thermal conductivity of foam concretes: homogenization schemes vs experimental data and fem simulations.” Mechanics Research Communications, 76, 96-100.

McHattie, R. L., and Goering, D. J. (2009). Air convection embankment (ACE) design guide. (No. FHWA-AK-RD-09-06). Alaska Department of Transportation and Public Facilities.

Mu, Y., Wei, M., Liu, Y., and Sun, Z. (2010). “Monitoring investigation on thermal stability of air-convection crushed-rock embankment.” Cold Regions Science and Technology, 62(2), 160-172.

Mu, Y. H., Ma, W., Sun, Z. Z., and Liu, Y. Z. (2011). “The Application of Crushed Rock Materials upon Railway Embankments in Permafrost Regions.” In Advanced Materials Research, 255, 4027-4033.

Mu, Y., Ma, W., Wu, Q., Sun, Z., and Liu, Y. (2012). “Cooling processes and effects of crushed rock embankment along the Qinghai-Tibet Railway in permafrost regions.” Cold Regions Science and Technology, 78, 107-114.

Nambiar, E. K. K., and Ramamurthy, K. (2007). “Sorption characteristics of foam concrete.” Cement and Concrete Research, 37(9), 1341-1347.

Narayanan, N., and Ramamurthy, K. (2000). “Structure and properties of aerated concrete: a review.” Cement and Concrete Composites, 22(5), 321-329.

Nield D. A., Bejan A. (2013). Convection in Porous Media, 4th edition. Springer New York Heidelberg Dordrecht London 2013.

Niu, F., Cheng, G., Xia, H., and Ma, L. (2006). “Field experiment study on effects of duct-ventilated railway embankment on protecting the underlying permafrost.” Cold Regions Science and Technology, 45(3), 178-192.

Pei, W., Zhang, M., Lai, Y., Jin, L., and Harbor, J. (2014). “Thermal stability analysis of crushed-rock embankments on a slope in permafrost regions.” Cold Regions Science and Technology, 106, 175-182.

Qian, J., Yu, Q. H., You, Y. H., Hu, J., and Guo, L. (2012). “Analysis on the convection cooling process of crushed-rock embankment of high-grade highway in permafrost regions.” Cold Regions Science and Technology, 78, 115-121.

Qian, J., Yu, Q. H., Jiang, Z. Q., Gu, W., and You, Y. H. (2012). "Comparative analysis of the natural convection process between hollow concrete brick layer and crushed rock layer." Cold Regions Science and Technology, 70, 117-122.

Ramamurthy, K., Nambiar, E.K.K., and Ranjani, G.I.S. (2009). "A classification of studies on properties of foam concrete." Cement and Concrete Composites, 31(6), 388-396.

Rasheed, M. A., and Prakash, S. S. (2015). "Mechanical behavior of sustainable hybrid-synthetic fiber reinforced cellular light weight concrete for structural applications of masonry." Construction and Building Materials, 98, 631-640.

Regehr, J. D., Milligan, C. A., Montufar, J., and Alfaro, M. (2013). "Review of Effectiveness and Costs of Techniques to Improve Roadbed Stability in Permafrost Regions." Journal of Cold Regions Engineering, 27(3), 109-131.

Risdanareni, P., Hilmi, A., and Susanto, P. B. (2017). "The effect of foaming agent doses on lightweight geopolymer concrete metakaolin based." Ism International Statistical Conference, 1835, 263-278.

Rooney, J. W. (1997). "Rock fill embankment applications for convective foundation cooling on the BAM railway system." Proceeding of 5th International Symposium on Cold Region Development, Anchorage, AK, 399-402.

Saboundjian, S., and Goering, D. J. (2003). "Air convection embankment for roadways: Field experimental study in Alaska." Transportation research record, 1821(1), 20-28.

Saboundjian S (2008). Evaluation of alternative embankment construction methods (No. FHWA-AK-RD-08-02). Alaska Department of Transportation and Public Facilities.

Samson, G., Phelipot-Mardelé, A., and Lanos, C. (2016). "A review of thermomechanical properties of lightweight concrete." Magazine of Concrete Research, 69(4), 201-216.

Sayadi, A. A., Tapia, J. V., Neitzert, T. R., and Clifton, G. C. (2016a). “Effects of expanded polystyrene (EPS) particles on fire resistance, thermal conductivity and compressive strength of foamed concrete.” Construction and Building Materials, 112, 716-724.

Sayadi, A. A., Vilches, T. J., Neitzert, T. R., and Clifton, G. C. (2016b) “Effectiveness of foamed concrete density and locking patterns on bond strength of galvanized strip.” Construction and Building Materials, 115, 221-229.

Sun, Z., Ma, W., and Li, D. (2005). “In Situ Test on Cooling Effectiveness of Air Convection Embankment with Crushed Rock Slope Protection in Permafrost Regions.” ASCE, Journal of Cold Regions Engineering, 19(2), 38-51.

Tian, W., Li, L., Zhao, X., Zhou, M., and Wang, N. (2009). “Application of Foamed Concrete in Road Engineering.” International Conference on Transportation Engineering, 2114-2120.

Tikalsky, P. J., Pospisil, J., and Macdonald, W. (2004). “A method for assessment of the freeze–thaw resistance of preformed foam cellular concrete.” Cement and Concrete Research, 34(5), 889-893.

Wang, H., Chen, W., Tan, X., Tian, H., and Cao, J. (2012). “Development of a new type of foam concrete and its application on stability analysis of large-span soft rock tunnel.” Journal of Central South University, 19(11), 3305-3310.

Wang, H. (2013). “Development and application of the light ceramsite foam concrete insulation block.” Advanced Materials Research, 608-609, 1690-1697.

Wu, Q., Ge, L., Liu, Y., and Zhang, T. (2010). “Thermal performance of embankment within crushed rock layer along Qinghai-Tibet railway.” International Journal of Offshore and Polar Engineering, 20(3), 210-217.

Xia, Y. (2014). “The development and application of foam concrete.” Advanced Materials Research, 919-921(43), 1962-1966.

Xu, J., and Goering, D. J. (2008). “Experimental validation of passive permafrost cooling systems.” Cold Regions Science and Technology, 53(3), 283-297.

Ye, Y., Wang, Z., Cheng, A., and Luo, M. (2007). “Frost Heave Classification of Railway Subgrade Filling Material and the Design of Anti-freezing Layer.” China Railway Science, 1, 1-7.

Yu, Q., Pan, X., Cheng, G., and He, N. (2008). “An experimental study on the cooling mechanism of a shading board in permafrost engineering.” Cold Regions Science and Technology, 53(3), 298-304.

Yue, J. W., Yue, T. T., Wang, Y. F., and Gu, L. H. (2013). “Experimental research on properties of low-density foaming concrete.” Advanced Materials Research, 683, 258-261.

Zhang, M., Lai, Y., Gao, Z., and Yu, W. (2006). “Influence of boundary conditions on the cooling effect of crushed-rock embankment in permafrost regions of Qinghai–Tibetan Plateau.” Cold Regions Science and Technology, 44(3), 225-239.

Zhang, M., Lai, Y., and Dong, Y. (2009). “Numerical study on temperature characteristics of expressway embankment with crushed-rock revetment and ventilated ducts in warm permafrost regions.” Cold Regions Science and Technology, 59(1), 19-24.

Zhang, Z., and Wang, H. (2016). “The pore characteristics of geopolymer foam concrete and their impact on the compressive strength and modulus.” Frontiers in Materials, 3, 10.

Zhi, W., Yu, S., Wei, M., and Qi, J. (2008). “In situ experimental study on thermal protection effects of the insulation method on warm permafrost.” Cold Regions Science and Technology, 53(3), 369-381.